

# Thermal transport in metal halide perovskites and other third-generation photovoltaic materials

Cite as: Appl. Phys. Rev. 11, 041311 (2024); doi: 10.1063/5.0226632

Submitted: 2 July 2024 · Accepted: 19 September 2024 ·

Published Online: 25 October 2024



View Online



Export Citation



CrossMark

Du Chen,<sup>1,2</sup>  Shunran Li,<sup>1,2</sup>  Bowen Li,<sup>1,2</sup>  and Peijun Guo<sup>1,2,a)</sup> 

## AFFILIATIONS

<sup>1</sup>Department of Chemical and Environmental Engineering, Yale University, New Haven, Connecticut 06520, USA

<sup>2</sup>Energy Sciences Institute, Yale University, West Haven, Connecticut 06516, USA

**Note:** This paper is part of the APR Special Topic on Frontiers in energy materials research: novel measurement, modelling and processing approaches.

<sup>a)</sup>Author to whom correspondence should be addressed: [peijun.guo@yale.edu](mailto:peijun.guo@yale.edu)

## ABSTRACT

Third-generation photovoltaic materials, including metal halide perovskites (MHPs), colloidal quantum dots (QDs), copper zinc tin sulfide (CZTS), and organic semiconductors, among others, have become attractive in the past two decades. Unlike their first- and second-generation counterparts, these advanced materials boast properties beyond mere photovoltaic performance, such as mechanical flexibility, light weight, and cost-effectiveness. Meanwhile, these materials possess more intricate crystalline structures that aid in understanding and predicting their transport properties. In particular, the distinctive phonon dispersions in MHPs, the layered architecture in quasi-two-dimensional (2D) perovskites, the strong quantum confinement in QDs, and the complex crystal structures interspersed with abundant disorders in quaternary CZTS result in unique and sometimes anomalous thermal transport behaviors. Concurrently, the criticality of thermal management in applications such as photovoltaics, thermoelectrics, light emitting diodes, and photodetection devices has received increased recognition, considering that many of these third-generation photovoltaic materials are not good thermal conductors. Effective thermal management necessitates precise measurement, advanced modeling, and a profound understanding and interpretation of thermal transport properties in these novel materials. In this review, we provide a comprehensive summary of various techniques for measuring thermal transport properties of these materials and discuss the ultralow thermal conductivities of three-dimensional (3D) MHPs, superlattice-like thermal transport in 2D perovskites, and novel thermal transport characteristics inherent in QDs and CZTS. By collecting and comparing the literature-reported results, we offer a thorough discussion on the thermal transport phenomenon in these materials. The collective understanding from the literature in this area, as reviewed in this article, can provide guidance for improving thermal management across a wide spectrum of applications extending beyond photovoltaics.

Published under an exclusive license by AIP Publishing. <https://doi.org/10.1063/5.0226632>

## TABLE OF CONTENTS

I. INTRODUCTION.....	2	2. Scanning thermal microscopy (SThM) .....	8
II. MEASUREMENT TECHNIQUES .....	3	3. Suspended-pad method .....	9
A. Laser flash analysis .....	3	G. Differential scanning calorimetry (DSC).....	9
B. Photoacoustic .....	5	III. 3D METAL HALIDE PEROVSKITES (MHPs) .....	9
C. Time/frequency-domain thermoreflectance (TDTR/FDTR).....	5	A. Introduction to 3D MHP photovoltaics .....	9
D. Transient thermal grating .....	7	B. Thermal conductivity measurements of MAPbI <sub>3</sub> ..	10
E. Other photothermal methods .....	8	1. Four-point probe.....	10
1. Optothermal Raman spectroscopy (OTRS) ...	8	2. SThM .....	11
2. Photothermal deflection spectroscopy (PDS) and thermal lens spectroscopy (TLS) .....	8	3. TDTR and FDTR .....	11
F. Electrothermal methods .....	8	4. Vibrational-pump visible-probe (VPVP) .....	12
1. 3ω method.....	8	5. Other experimental methods.....	12
		6. Numerical simulations .....	12
		C. Constituent-dependent thermal conductivity of MAPbI <sub>3</sub> .....	13

D. Temperature-dependent thermal conductivity of MAPbI <sub>3</sub> .....	14
IV. QUASI-2D METAL HALIDE PEROVSKITES .....	15
A. Introduction to 2D MHPs.....	15
B. Ultralow thermal conductivities exceeding bulk limits .....	16
C. Partially coherent cross-plane thermal transport..	17
D. Measuring anisotropic thermal transport .....	20
E. Temperature-dependent thermal transport.....	20
F. Lower dimensionality .....	24
V. COMPOSITIONAL ORIGINS OF THE ULTRALOW THERMAL CONDUCTIVITIES OF MHPs .....	25
A. Role of A-site cation and [BX <sub>6</sub> ] <sup>4-</sup> octahedra.....	25
B. Role of A'-site organic spacers in 2D MHPs .....	26
VI. OTHER THIRD-GENERATION PHOTOVOLTAIC MATERIALS .....	28
A. Quantum Dots (QDs).....	28
1. Metal chalcogenide QDs .....	29
2. Graphene QDs.....	29
B. Copper zinc tin sulfide/selenide (CZTS/Se).....	30
VII. SUMMARY AND OUTLOOK.....	32

## I. INTRODUCTION

The escalating global energy demand along with the need for sustainable and environmentally friendly energy sources has propelled the development of advanced photovoltaic (PV) materials. Photovoltaics, which directly converts sunlight into electricity, will play a pivotal role in the future energy landscape. First-generation PV materials, primarily crystalline silicon-based, have dominated the market for decades, achieving improved efficiency and cost reduction. Second-generation thin-film solar cells, including amorphous silicon, cadmium telluride (CdTe), and copper indium gallium selenide (CIGS), are much more lightweight, flexible, and have lower production costs. However, these PV materials face inherent limitations in efficiency due to high non-radiative recombination and low material availability.<sup>1</sup> This has driven significant interests in third-generation PV materials, which promise higher efficiencies, novel functionalities, and potentially lower manufacturing costs.<sup>2</sup> In particular, metal halide perovskites (MHPs), colloidal quantum dots (QDs), and copper zinc tin sulfide (CZTS) stand out as promising candidates due to their unique optoelectronic properties.

MHPs have garnered substantial attention due to their remarkable power conversion efficiency, which has rapidly increased from below 4% to over 26% within a decade.<sup>3–11</sup> Their facile solution-based processing,<sup>3,12</sup> tunable bandgaps,<sup>13,14</sup> and defect tolerance<sup>15,16</sup> make them highly attractive for various optoelectronic applications. In the case of lead halide perovskites, the 6s orbital lone pair electrons in Pb enable highly symmetrical structures and thus direct bandgaps, leading to strong absorption of light in the visible and near-infrared spectrum suitable for PV applications.<sup>17</sup> In addition, the coupling between the s and p orbitals of Pb and I allows the formation of defect states near or within the valence band and conduction band, making MHPs defect-tolerant with long carrier diffusion lengths.<sup>18</sup> The structure of perovskites can also be substantially modified by changing the organic cation, allowing them to be tailored into two-dimensional (2D) layered MHPs. In three-dimensional (3D) MHPs with a general formula of ABX<sub>3</sub>, the A-site cation is contained within cages formed between the

octahedral structures. In contrast, in 2D MHPs, the octahedra are confined in 2D layers, separated by bulk organic spacers that exert strong quantum and dielectric confinement on charge carriers.<sup>19</sup> The wide range of available spacers and choice of the layer number enable a larger structural tunability and chemical diversity of 2D MHPs.

Colloidal QDs, sometimes referred as nanocrystals, are nanoscale semiconducting particles, which could be utilized for third-generation photovoltaics. QDs exhibit strong quantum confinement effects, leading to discrete energy levels and size-tunable optical properties.<sup>20,21</sup> QDs have large multi-exciton generation efficiency due to enhanced impact ionization, making it possible to bypass the efficiency bottleneck of single-junction solar cells.<sup>22,23</sup> Another third-generation PV material is CZTS, which has a direct bandgap and a high optical absorption coefficient, making it suitable for thin-film solar cells.<sup>24</sup> Unlike some traditional PV materials, CZTS is made of earth-abundant and nonpoisonous elements, addressing some of the critical material availability and environmental concerns.<sup>25</sup>

While the remarkable electronic and optical properties of third-generation PV materials have been extensively explored, fewer efforts have been spent on understanding the thermal transport behaviors of such systems, which significantly influence device performance, stability, and robustness under operation conditions. Effective thermal management is critical for the efficiency and longevity of PV devices due to the existence of many thermal-activated processes. Excessive heat can lead to increased carrier recombination rates, reduced carrier mobility, phase transitions, and material degradation.<sup>26–29</sup> As an example, MAPbI<sub>3</sub>, one of the prototypical MHPs, undergoes a phase transition from tetragonal to cubic above room temperature, which impedes efficiencies after thermal cycling.<sup>30</sup> Elevated temperature is also shown to accelerate material degradation significantly and chemical decomposition can happen at temperatures as low as 80 °C,<sup>31,32</sup> which is possible in practical solar cell operations.<sup>33</sup>

To effectively lower the operation temperature and optimize the design of PV devices, precise measurement and control of thermal transport properties of PV materials are necessary. As shown in Fig. 1(a), during the past 30 years, the amount of research effort on thermal transport measurements of PV materials surged. This trend is synchronous with the development of third-generation PV materials, which generally possess much smaller thermal conductivities than crystalline silicon [Fig. 1(b)], further attracting attention to thermal management. MHPs are known for their ultralow thermal conductivities. Specifically, low thermal conductivities in MHPs can be attributed to the flattening of low-frequency phonon bands and thus low phonon group velocities, as well as strong anharmonicity arising from the soft inorganic octahedral lattice, which are present regardless of organic cation composition.<sup>34–36</sup> However, the presence of organic cations may still modify the thermal properties of the perovskite, by either introducing new vibrational modes or altering material structures. In 3D organic-inorganic hybrid MHPs, the phonon mode associated with slow rotation of the organic cation might also contribute to low thermal conduction at low temperatures.<sup>37</sup> In 2D hybrid MHPs, weak van der Waals forces binding neighboring perovskite layers further impede cross-plane thermal transport.<sup>38</sup> The anisotropy of 2D perovskites poses a challenge in measuring both in-plane and cross-plane thermal conductivities accurately. Additionally, the intrinsic instability of hybrid MHPs requires careful consideration of measurement conditions. Vacuum conditions and non-contact methods are

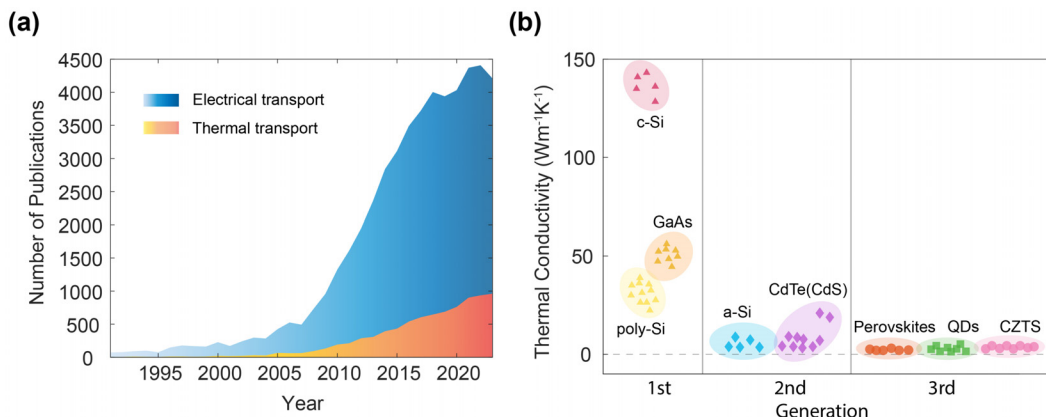


**FIG. 1.** (a) Number of publications on the electrical (blue) and thermal transport (orange) measurements and properties of photovoltaic materials as a function of years. (b) Thermal conductivity ranges of the first-, second-, and third-generation photovoltaic materials. c-Si: single-crystalline silicon. poly-Si: polycrystalline silicon. a-Si: amorphous silicon. QDs: quantum dots. CZTS: copper zinc tin sulfide.

preferred to avoid degradation during testing. Therefore, versatile and flexible measurement techniques are essential to accurately characterize the thermal transport properties of these materials under varying conditions.

This review aims to provide a comprehensive coverage of the thermal transport properties of MHPs, while touching on QDs and CZTS, highlighting the experimental techniques used for their measurements. Note that our discussion does not cover organic semiconductors, which has been reviewed elsewhere recently.<sup>39</sup> The first section of the review will introduce a range of commonly used photo-thermal and electrothermal-based measurement techniques, focusing on their operation principles and capabilities. The second part discusses the thermal properties of 3D MHPs, and the effects of chemical composition, temperature, and phonons on thermal transport and summarizes experimental and simulation efforts on evaluating thermal properties. The third section considers the scenario of 2D or lower-dimensional MHPs, and in addition to topics discussed for the 3D case, emphasizes mechanisms and measurements of in-plane and cross-plane anisotropic transport. Finally, the application of QDs and CZTS in photovoltaics and efforts to maximize thermal conduction in these systems are discussed. By combining and comparing the reported results, this review seeks to clarify the range of applicability and limitations of methods used for thermal property measurement of PV materials and shed light on the underlying physical mechanisms governing their thermal transport. Accurate determination and understanding of their thermal transport properties will inform the development of strategies for effective thermal management, thereby enhancing the performance and durability of PV devices and broadening their applicability in various optoelectronic applications.

## II. MEASUREMENT TECHNIQUES

Broadly, thermal transport measurement techniques can be categorized into transient heat-flow methods and periodic heat-flow methods. The latter method was first pioneered by Angström as early as 1863, wherein one end of a metal rod is subjected to periodic heating and the temperature oscillation at another point on the rod was

measured.<sup>40</sup> The phase lag between the temperature oscillations at two points offers an accurate evaluation of thermal diffusivity, and consequently, thermal conductivity ( $\kappa$ ). Various heat sources, such as light illumination or electrical Joule heating, can induce heat flow in the sample during the measurement. Here, we primarily focus on the photo-thermal methods, where temperature variations are induced by light absorption and the resulting effects are detected through various signal modalities. A transient decay in the time domain or a modulation dependence in the frequency domain of the detected signals, in either transient heating or periodic heating scenarios, respectively, provides a direct measurement of the thermal transport properties of materials. Below, we give a brief account of the techniques utilized for characterizing third-generation PV materials. Readers interested in a specific technique are encouraged to read the references in each section.

### A. Laser flash analysis

The laser flash method (LFM), also known as the laser flash analysis (LFA), was invented by Parker *et al.* in 1961.<sup>41</sup> Since its inception, LFA has been extensively adopted for measuring the thermal diffusivity of materials, including PV semiconductors,<sup>42–44</sup> owing to its simplicity and ease of implementation. A typical LFA setup is depicted in Fig. 2(a), where a disk or square-shaped specimen is secured in an adiabatic chamber, and its front surface is irradiated by a short laser pulse. The temporal rise in temperature of the rear surface, which manifests as infrared (IR) radiation, is then detected by an IR sensor. This scenario can be accurately described by a one-dimensional heat transfer equation that is analytically solvable. For an optically opaque and geometrically uniform specimen with a thickness of  $d$ , the thermal diffusivity can be determined from the time of temperature rise as

$$\alpha = 0.1388 \frac{d^2}{t_{1/2}}, \quad (1)$$

where  $\alpha$  is the thermal diffusivity in  $\text{cm}^2 \cdot \text{s}^{-1}$  and  $t_{1/2}$  is the time for the rear-surface temperature rise to reach half of the maximum value. Since LFA measures thermal diffusivity, separate measurements of

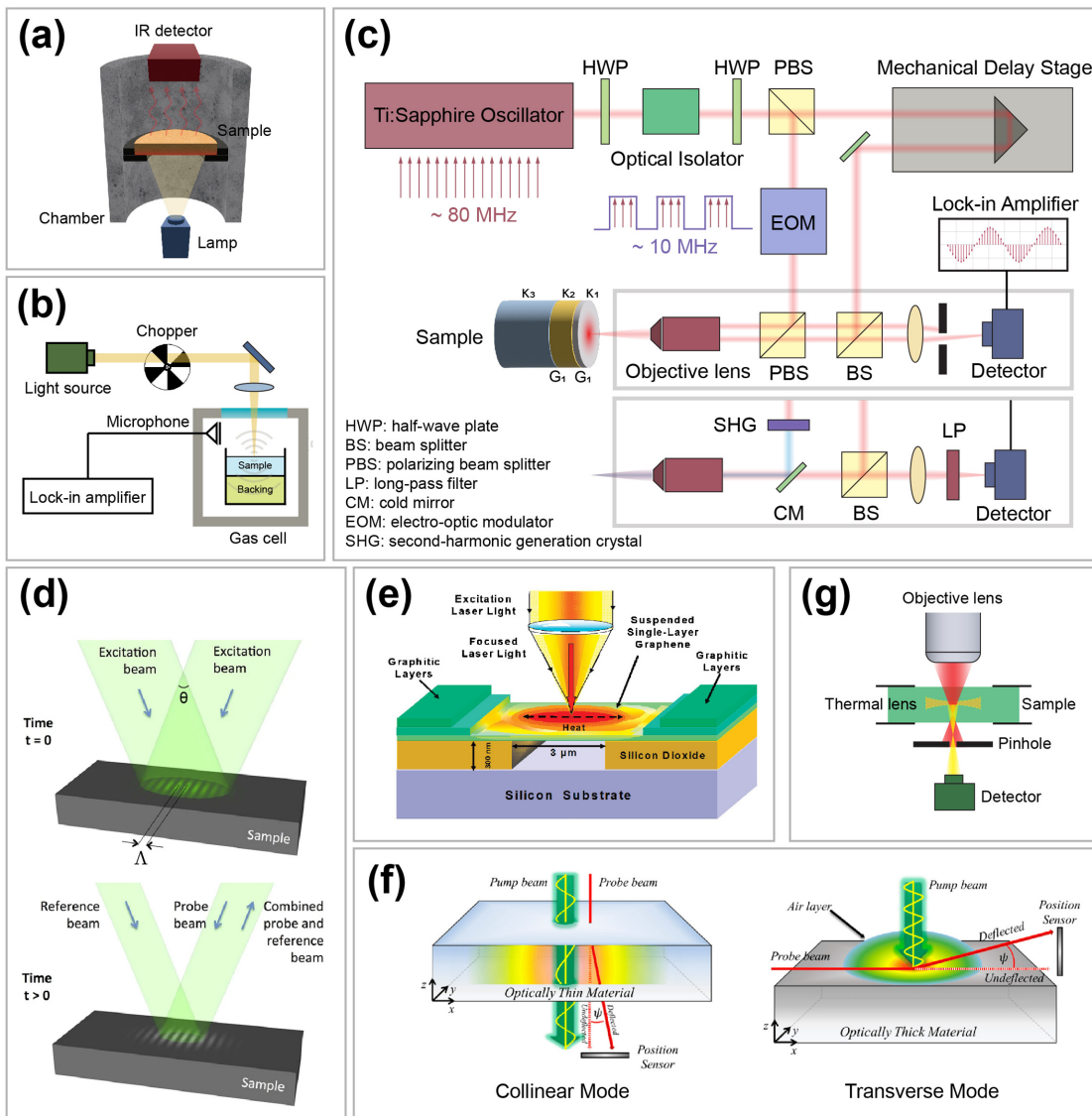


**FIG. 2.** Schematics of photothermal-based thermal transport measurement techniques. (a) Laser flash analysis (LFA). (b) Photoacoustic spectroscopy (PAS) using front-surface illumination and a microphone as the sensor. (c) Time-domain thermoreflectance (TDTR) with spatially separated (upper boxed panel) or spectrally separated (lower boxed panel) pump and probe beams. (d) Transient thermal grating (TTG). Upper panel: absorption grating with a periodicity of  $\Lambda$  excited by two overlapped pump beams at an angle of  $\theta$ . Lower panel: transient detection of the resulting thermal grating by a reflected probe beam. Reproduced with permission from Hofmann *et al.*, *Sci. Rep.* **5**, 16042 (2015). Copyright 2015 Springer Nature.<sup>445</sup> (e) Optothermal Raman spectroscopy (OTRS) on a graphene monolayer suspended across a trench. Reproduced with permission from Balandin *et al.*, *Nano Lett.* **8**(3), 902–907 (2008). Copyright 2008 American Chemical Society.<sup>135</sup> (f) Photothermal deflection spectroscopy (PDS) in the collinear mode (left panel) for transparent materials and the transverse mode (right panel) for opaque materials. Reproduced with permission from Kim *et al.*, *Appl. Sci.* **9**(8), 1522 (2019). Copyright 2019 Authors, licensed under a Creative Commons Attribution (CC-BY) license.<sup>446</sup> (g) Thermal lens spectroscopy (TLS). A diverging thermal lens formed inside the sample deflects (defocuses) the light, allowing it to pass through the pinhole and be detected.

mass density ( $\rho$ ) and specific heat ( $C_p$ ) are required to calculate the effective thermal conductivity  $\kappa_{\text{eff}}$  using the following relationship:

$$\kappa_{\text{eff}} = \alpha \cdot C_p \cdot \rho. \quad (2)$$

While uncertainty of the thermal conductivity determination by classical LFA was estimated to be from  $\pm 3\%$  to  $\pm 5\%$ ,<sup>45</sup> more nuanced

analysis that takes into account thermal radiation loss and other uncertainties in LFA to improve the accuracy has also been reported.<sup>46,47</sup> Instead of the conventional half-rise time method, the entire time-dependent temperature curve can be fitted with calculations, providing a more accurate determination of thermal diffusivity<sup>48</sup> or enabling the simultaneous evaluation of both thermal diffusivity and heat capacity.<sup>49</sup> A crucial requirement for LFA is that the flash duration is much

shorter compared to the characteristic time of heat diffusion, defined as  $\tau_c = d^2/\alpha$ , where  $d$  is the sample thickness.<sup>41</sup> This imposes stringent constraints on the sample thickness, typically required to be of millimeter-scale. Furthermore, commercial equipment often necessitates a minimal lateral sample size of several millimeters (e.g.,  $8 \times 8 \text{ mm}^2$  in Netzsch LFA 457).<sup>50</sup> Consequently, commercial LFA instrument is generally employed for measuring the “effective” and isotropic thermal diffusivity of large single crystals or powder-compressed specimens. That being said, some careful treatment of the specimen dimension could potentially enable the measurement of anisotropic thermal transport properties.<sup>51</sup>

A method analogous to LFA is pulsed photothermal radiometry (PPTR), which adopts a nearly identical measurement configuration. The primary distinction is that PPTR collects IR emission from the front surface, i.e., the same side as for illumination. Unlike LFA where the temperature rise is contributed by the entire volume of the sample, PPTR measures the temperature decay of a skin layer of the surface, making it more sensitive to the surface and sub-surface properties.<sup>52</sup> With more complex modeling and data analysis, PPTR could provide depth-resolved information of complex structures and layered materials.<sup>53,54</sup>

## B. Photoacoustic

Photoacoustic (PA) effect involves the generation of acoustic waves by the absorption of light or other forms of radiation incident on the sample. Such effect was first discovered by Alexander Graham Bell in as early as 1880,<sup>55</sup> but it faded into obscurity until the late 20th century with the advent of sensitive detectors and intense light sources. PA subsequently emerged as a viable tool for spectral absorption and thermal transport characterization.<sup>56–60</sup> An important advantage of photoacoustic spectroscopy (PAS) over reflection-based method, which will be discussed later, is that ultrasmooth and highly reflective surfaces are not necessary.<sup>61</sup>

In a typical PAS measurement on solids, a chopped beam of continuous-wave (CW) light or pulsed laser light is incident onto either the front or rear surface of an absorbing sample. The absorbed radiation energy is dissipated into the lattice, primarily as heat. The subsequent periodic temperature excursion leads to intermittent thermal expansion via thermo-elastic effects, generating acoustic waves that propagate through the interior of samples, subsequently detected by a sensor. This detection scheme is sometimes referred to as the transmission mode.<sup>62</sup> Alternatively, the PA signals can be collected from a fluid (usually gas) in contact with the surface of the sample enclosed in a gas cell. A periodic modulation of surface temperature of the sample gives rise to pressure oscillations in the gas, the amplitude of which is proportional to the surface temperature.<sup>63</sup> The collected signal is then amplified and analyzed with a lock-in amplifier.<sup>61</sup>

Despite some literatures distinguishing between PA effect (direct generation of acoustic waves inside the sample) and opto-acoustic effects (acoustic waves induced in an adjacent fluid),<sup>64,65</sup> in this review, we will use “PA” as a common reference. Generally, PA signals indirectly measured from the adjacent gas under front-surface illumination are more sensitive to the surface temperature changes, while the direct acoustic waves are more influenced by the overall thermal and elastic properties of the sample. In the case of highly absorbing materials where only a skin layer of the sample surface is heated, PA signals from the gas can provide a higher sensitivity.

Conventionally, either a microphone or a piezoceramic transducer can be used as the detector for PA signals. Despite the fact that microphone is an inexpensive and most commonly used type of detector in PAS, piezoelectric sensors have the advantage of eliminating acoustic mismatch between the gas, the solid sample surface, and the microphone membrane. Additionally, piezoelectric transducers enable the use of much higher modulation frequency,<sup>66</sup> which is beneficial for avoiding PA saturation<sup>57,67</sup> and achieving high-resolution photoacoustic imaging.<sup>68</sup> A typical PAS setup is illustrated in Fig. 2(b) adopting a microphone detector.

While both front- and rear-surface illumination configurations are available, it has been verified that accurate thermal transport measurement by PAS requires rear-surface illumination and a modulation frequency appropriately higher than the characteristic frequency,  $f_c = \frac{\pi}{d}$  to eliminate the influence of backing substrate on the results.<sup>57</sup> In this configuration, the sample is usually directly backed by water and then a solid substrate to minimize the parasitic coherent effects accompanying rear illumination.<sup>57</sup> Otherwise, careful system calibration is needed to determine the ratio of effusivities between the backing substrate and sample,  $g = \frac{e_b}{e_s}$ , where  $e_b$  and  $e_s$  are the effusivities of the substrate and sample, respectively.<sup>56</sup> Note that front-surface illumination requires knowledge of  $g$  and a modulation frequency lower than  $f_c$ .

To determine the thermal diffusivity of the sample, PA measurements can be performed with either a varying or a single modulation frequency. Both the modulation-frequency dependence of signal magnitude<sup>57</sup> and phase<sup>64</sup> provides information to extract the thermal diffusivity. Using a single modulation frequency, thermal diffusivity can also be evaluated with a similar scheme to the Angström method,<sup>40</sup> where the phase and magnitude of PA signals are measured at varying distances away from the heat source.<sup>69</sup> Alternatively, magnitude ratio and phase difference of the signals between front- and rear-surface illuminations under single modulation can be used to precisely determine the thermal diffusivity.<sup>58</sup>

Instead of using uniform illumination, photoacoustic microscope focuses the excitation light down to a small spot on the sample with a lens or an objective to achieve photoacoustic imaging on a microscopic lengthscale.<sup>62,68</sup> Combined with the capability of PA signals to provide depth-profile information,<sup>70</sup> subsurface features that are hard to observe with an optical microscope can be visualized.<sup>54,68</sup> It is also worth noting that one of the unique characteristics of PAS over other spectroscopic methods is that signals can originate from diverse excited-state decay pathways generating acoustic waves, such as thermal expansion,<sup>57,71</sup> electrostriction,<sup>72,73</sup> breakdown and plasma formation,<sup>74</sup> molecule decompositions,<sup>75</sup> and charge carrier recombination.<sup>76</sup>

## C. Time/frequency-domain thermoreflectance (TDTR/FDTR)

Thermoreflectance (TR) is a modulation technique predicated on a periodic perturbation of temperature, which alters the optical properties of the samples that lead to a reflectivity change. For metals, the change in the complex refractive index with temperature ( $\frac{dn}{dT}$ ) arises from several temperature effects including changes in energy bands, shifts and broadening of the Fermi level, and variations in electron-phonon scattering rates.<sup>77</sup> Additional effects such as shifts of energy bandgaps in semiconductors also play a role.<sup>78</sup> The resulting rate of

change in reflectivity ( $\frac{dR}{dT}$ ), also termed as the thermoreflectance coefficient, is found to be constant ( $10^{-5}$ – $10^{-4}$  K $^{-1}$ )<sup>79</sup> within a small temperature perturbation (<10 K) at a given wavelength.<sup>80</sup> Thus, the AC component of reflectivity change ( $\Delta R$ ) in TR is directly proportional to the amplitude of the temperature modulation ( $\Delta T$ ), allowing the monitoring of temperature changes during the heat flow. The first thermal transport measurement applying thermoreflectance dated back to 1986,<sup>81,82</sup> where ultrafast lasers with a modulation frequency as high as 10 MHz were used to induce periodic heating and the transient temperature change was investigated in the time domain with a picosecond time resolution. This measurement scheme was later recognized as time-domain thermoreflectance (TDTR).

A key advantage of TDTR over conventional photothermal methods such as LFA is the use of ultrafast lasers with nanosecond (ns) to picosecond (ps) pulse durations,<sup>83</sup> which facilitates the measurement of thin films with nanometer-scale thickness. The heat diffusion length is defined as  $L = \sqrt{\alpha \cdot \delta t}$ , where  $\alpha$  is the thermal diffusivity and  $\delta t$  is the heating time (approximated as the pulse duration). As discussed for LFA, a valid evaluation of  $\kappa$  of thin-film materials requires sample thickness to exceed the thermal diffusion length. The latest model of LFA 457 HyperFlash provides a pulse width down to 10  $\mu$ s, with the lower limit for measuring a highly conductive sample such as a copper plate being around 200  $\mu$ m. In comparison, with an ultrashort pulse duration, TDTR allows measurement of samples ranging from bulk sizes<sup>84</sup> down to several tens of nanometers<sup>85</sup> and with  $\kappa$  ranging from ~2000 W · m $^{-1}$  · K $^{-1}$  to as low as 0.03 W · m $^{-1}$  · K $^{-1}$ .<sup>86,87</sup>

In a TDTR measurement, a metallic transducer with a high thermoreflectance coefficient is deposited onto the sample surface. The pump and probe beams are focused onto the transducer to comparable spot sizes (5–20  $\mu$ m). The pump beam induces periodic heat flow from the transducer to the sample and substrate while the probe captures the thermoreflectance response. Figure 2(c) illustrates a typical experimental configuration of TDTR. A mode-locked Ti:sapphire laser oscillator with a center wavelength at 800 nm generates a train of sub-ps optical pulses at a repetition rate of 80 MHz. A Faraday optical isolator follows immediately after the laser output to prevent back reflection into the oscillator. The laser is then split into two cross-polarized pump and probe beams by a polarizing beam splitter (PBS). The pump beam is typically modulated to a square wave at a frequency of 0.2–20 MHz by an electro-optic modulator (EOM), or an acousto-optic modulator (AOM) with a modulation frequency usually smaller than 1 MHz.<sup>88,89</sup> The probe beam is delayed with respect to the pump beam by up to several thousands of ps via a mechanical delay stage. Both the pump and probe beams are then directed and focused by an objective lens onto the sample surface, with the reflected probe beam collected by a photodiode detector converting the varying photon counts to oscillating electrical signals. A radio-frequency lock-in amplifier with a clean sine-wave modulation at the same frequency as the pump beam analyzes the signals, rejecting the DC component and higher harmonics, and isolating only the fundamental harmonic component of EOM.

Several precautions are necessary for TDTR. First is the appropriate choice of transducer according to the laser source used. For a Ti:sapphire laser, an aluminum thin film with a thickness of ~100 nm is preferred due to its strong absorption<sup>77</sup> and remarkably high thermoreflectance coefficient of  $\sim 10^{-4}$  K $^{-1}$  at 800 nm.<sup>90</sup> When using other types of ultrafast lasers such as a Nd:YAG laser centered at 1064 nm, a

Yb-doped fiber laser centered at 1030 nm, or a dye laser centered at 632 nm, different materials may be preferred as the transducers. Another concern is preventing the pump from leaking into the detector, as even a minor amount of pump light can disrupt the signals due to the small absolute value of  $\frac{dR}{dT}$  from the probe. Two approaches are commonly applied to address this issue. One is to spatially separate the parallel pump and probe beams by several millimeters before entering the objective, allowing the specular reflection of the pump to be blocked by a carefully placed aperture.<sup>88</sup> This approach is illustrated in the upper boxed panel in Fig. 2(c). While effective for smooth samples with minimal diffuse scattering of pump from the sample surface,<sup>91</sup> a “two-color” approach to spectrally separate the pump and probe is also widely adopted.<sup>92</sup> As shown in the lower boxed panel in Fig. 2(c), the pump beam coming out of the EOM is incident on a second-harmonic generation (SHG) crystal. The frequency-doubled pump beam and probe beam are then coaxially aligned and focused by the objective lens. In this case, the beam splitter can be replaced by a dichroic mirror (cold mirror) and the reflected pump beam can be further eliminated by a long-pass filter in front of the detector.

During a TDTR measurement, the lock-in amplifier outputs voltage signals comprising both in-phase and out-of-phase components as  $V(t) = V_{\text{in}}(t) + iV_{\text{out}}(t)$ , which contain the necessary thermal information. While the in-phase signal  $V_{\text{in}}$  is directly related to the transient temperature decay<sup>93</sup> and  $V_{\text{out}}$  is related to modulated continuous heating,<sup>94</sup> it is usually the phase,  $\varphi = \tan^{-1}(V_{\text{out}}/V_{\text{in}})$ , or equivalently the ratio  $R = -V_{\text{in}}/V_{\text{out}}$  of the signal that is used to determine the  $\kappa$  of the material.<sup>89,95</sup> Calibration to subtract additional instrument phases introduced by the optics and electronics is crucial. The instrument phase can be directly measured by splitting a small fraction of the modulated pump beam to a reference detector with the same optical path length as the pump incident on the sample,<sup>96</sup> or calculated using the ratio between the change in  $V_{\text{out}}$  and  $V_{\text{in}}$  across zero delay time.<sup>89</sup>

Similar to some of the thermal transport measurements we discussed in Sec. II A, TDTR determines the thermal transport properties by iteratively fitting unknown objective parameters, such as  $\kappa$  or diffusivity, and heat capacity, into a carefully constructed heat transfer model to obtain optimal agreement with the measured signals. A widely used diffusive thermal transport model based on Fourier’s law of heat transfer in cylindrical coordinates is written as follows:<sup>89,97</sup>

$$C \frac{\partial T}{\partial t} = \frac{\kappa_r}{r} \frac{\partial}{\partial r} \left( r \frac{\partial T}{\partial r} \right) + \kappa_z \frac{\partial^2 T}{\partial z^2}, \quad (3)$$

where  $\kappa_r$  and  $\kappa_z$  are the thermal conductivities of the sample in the radial (in-plane) and cross-plane directions, respectively.  $C$  is the volumetric heat capacity. The interfacial thermal conductance  $G$  between the transducer and sample, or between the interlayers of a multi-layer sample is also taken into consideration, manifesting as a temperature drop that scales linearly with the heat flux ( $q$ ) across the interfaces, i.e.,  $\Delta T = q/G$ . The uncertainty of fitting single or multi-parameters with a single measurement can differ depending on factors such as materials and substrate properties, transducer thickness, spot size, and modulation frequency. For instance, TDTR with a high modulation frequency is more sensitive to the thermal effusivity,  $\sqrt{C\kappa}$ , rather than to individual properties. As a result, the uncertainty in separately extracting  $C$  and  $\kappa$  is relatively high. At lower modulation frequencies,  $C$ ,  $\kappa$  and  $G$  can be uniquely determined with a high precision. A more

detailed discussion on uncertainty analysis in TR techniques can be found elsewhere.<sup>98</sup>

Note that deviation from the above model will occur as the thermal transport approaches the Casimir regime, where heat transfer is dominated by the ballistic transport of phonons with long mean free paths (MFPs). Practically, this could be the case when the sample is “thermally thin”, i.e., the thickness is smaller than the thermal penetration depth,  $d = \sqrt{\kappa_z/\pi fC}$ , where  $f$  is the modulation frequency of the pump.<sup>99</sup>

In the majority of TDTR measurements where  $\kappa_z$  and  $G$  are of the most interest, the above heat diffusion equation can be simplified to a 1D or quasi-1D cross-plane transport equation. In such cases, the pump spot size must be much larger than the thermal penetration depth, which corresponds to a high modulation frequency. Note that the relationship between the TR signals of TDTR and the actual temperature decay is not straightforward due to the pulse accumulation effect.<sup>89</sup> At high modulation frequencies, the system does not have sufficient time to reach thermal equilibrium between pulses, causing continuous temperature excursions. Detailed calculation processes of TDTR signals addressing the after-pulse heating by solving the heat diffusion model in either time<sup>89</sup> or frequency domain<sup>97</sup> can be found elsewhere.

Alternative to TDTR, the modulation frequency-dependent TR response under a variation of modulation frequency of the pump can be used to measure thermal transport properties, which is known as frequency-domain thermoreflectance (FDTR).<sup>96</sup> In FDTR, both the pump and probe can use CW lasers, which greatly simplifies the configuration and reduces the instrument cost. The TR signals are measured with respect to frequency rather than time, and the model is solved in the frequency domain to fit the  $\tan^{-1}\left(\frac{V_{out}}{V_{in}}\right)$  vs  $f$  curve. Any thermal property described in Eq. (3), i.e., cross-plane and in-plane  $\kappa$ , and heat capacity can be extracted from the TDTR or FDTR signals by implementing different experimental conditions, provided that the rest of the parameters are known, such as the spot size, heat capacity, and  $\kappa$  of the transducer.<sup>84</sup>

Despite the numerous advantages of TDTR and FDTR, these techniques also have certain limitations. First of all, although TR-based methods require minimal sample preparation, a smooth surface (roughness < 15 nm) is often preferred.<sup>100</sup> Additionally, TDTR/FDTR has relatively low sensitivity to radial heat transfer, presenting challenges in measuring in-plane  $\kappa$  or resolving spatial inhomogeneity of the sample. Fortunately, special configurations and approaches have been reported to overcome these limitations and achieve determination of in-plane  $\kappa$  with a low uncertainty.<sup>89,101–105</sup> Moreover, the performance of TDTR/FDTR at low temperatures is limited due to the low heat capacity of the transducer and its large temperature excursion. In spite of these constraints, TR-based methods are regarded as powerful and versatile methods for measuring the thermal transport properties of materials, particularly thin films and for investigating phonon MFPs.<sup>106–108</sup>

It is also worth noting that recent research has focused on removing or replacing the metallic transducers, which induce parasitic contact effects and compromise the sensitivity of conventional TR experiments to deeply buried interfacial thermal conductance, in-plane thermal conduction, and spatial inhomogeneity.<sup>109–111</sup> For example, one of the transducer-less TR methods, vibrational-pump-visible-probe (VPVP) spectroscopy, directly heats up thin-film MHPs with infrared light and monitors their transient TR response without any

sample preparation.<sup>112,113</sup> Alternatively, *h*-BN, which is commonly applied as an encapsulation layer in nanoscale PV devices, can be heated with pulsed mid-infrared light. The optical transparency of *h*-BN to visible probe light allows direct spectroscopic observation of the heat flow within and across each of the deeply buried layers of the device.<sup>114</sup> These two variations of TR provide novel means for achieving *in situ* thermal transport measurements on either macroscopic or nanoscale PV materials and devices.

#### D. Transient thermal grating

Transient thermal grating (TTG) is a spatially periodic temperature distribution generated by the absorption of two interfering pump beams.<sup>115</sup> The thermal grating produces a spatial modulation of the refractive index through the thermo-optic effect, along with a spatially varying surface displacement due to ununiform thermal expansion.<sup>116</sup> A time-delayed probe laser incident on the sample is diffracted by the thermal grating and used to monitor the temporal evolution (decay) of the thermal grating. The relaxation time of the grating is then used to extract the thermal diffusivity of the samples. Because the TTG method involves direct excitation of the semiconductors, a population grating or a spatially periodic distribution of excited and ground states coexists with the temperature grating and simultaneously contributes to the diffraction of the probe beam. However, the relaxation time of the population grating can differ by several orders of magnitude from that of thermal grating, allowing it to be separated from thermal transport modeling.<sup>117,118</sup> Materials with substantially long carrier lifetime (e.g.,  $\text{MAPbI}_3$ <sup>119</sup>) are not suitable for this method because it becomes difficult to distinguish between the contributions of heat and charge carriers to the TTG signals.

TTG can adopt versatile configurations,<sup>116</sup> among which a frequently used four-wave setup working in reflection mode is illustrated in Fig. 2(d). Two pump beams with a wavelength of  $\lambda$  (usually above-bandgap) overlap on the sample surface with an angle of  $\theta$ , generating a spatial intensity pattern through interference with a period of  $\Lambda$ ,

$$\Lambda = \frac{\lambda}{2\sin\left(\frac{\theta}{2}\right)}. \quad (4)$$

The non-uniform absorption on the surface produces a temperature grating, periodic thermo-elastic deformation, and surface acoustic waves, relaxation of which all have different time dependences.<sup>120–122</sup> Transient decay of the temperature grating can be monitored by the intensity change of the reflected probe, which follows an exponential decay. The thermal diffusivity can be readily determined from the decay time constant without any complex modeling as<sup>117</sup>

$$\alpha = \frac{\Lambda^2}{4\pi^2\tau}, \quad (5)$$

where  $\tau$  is the time constant of the exponential decay and  $\Lambda$  is the grating period.

One of the most appealing features of TTG method is its high sensitivity to the lateral heat transfer (parallel to the grating period), thus its capability to measure the in-plane transport of anisotropic semiconductors, such as quasi-2D perovskites<sup>123</sup> and transition metal dichalcogenides.<sup>124</sup> Meanwhile, film-morphology-induced macroscopic anisotropy can also be studied by TTG.<sup>125</sup> While the transient

relaxation of the temperature at the interference maxima follows a  $t^{1/2}$  decay, the temperature response at the grating minima is directly governed by the lateral thermal diffusivity  $\alpha_{||}$  as<sup>126</sup>

$$T \propto \frac{1}{\sqrt{t}} (1 - e^{-4\pi^2 \alpha_{||} t / A^2}). \quad (6)$$

Furthermore, as the TTG is primarily influenced by the sample from the surface up to a depth of  $A/\pi$ ,<sup>126</sup> depth-dependent thermal diffusivity can be semi-quantitatively determined by varying the grating period, either through changing the wavelength or incident angle of the pump.

### E. Other photothermal methods

Beyond the photothermal-based methods discussed above—LFA, PPTR, TDTR, FDTR, and TTG—other temperature-induced effects, such as light deflection,<sup>127,128</sup> thermal lens,<sup>129,130</sup> and Raman peak shifts,<sup>131,132</sup> can also be exploited to produce discernible signals. Although these methods are not as prevalently employed for PV materials and thus fall out of the scope of this review, we will briefly elucidate them here.

#### 1. Optothermal Raman spectroscopy (OTRS)

Optothermal Raman spectroscopy (OTRS), also known as Raman thermometry, is a steady-state measurement wherein a tightly focused laser beam heats up and probes the Raman spectrum of the sample as illustrated in Fig. 2(e). Temperature elevation induces modifications of the Raman spectrum: an increase in the Raman peaks intensity due to increased phonon populations, and a redshift of the Raman peak owing to the softening of vibrational modes at increased temperature. Under slight perturbations, the redshift of the peak frequency scales linearly with the temperature rise, which itself is linearly dependent on the absorbed laser power. Consequently, employing a micro-Raman spectrometer as a thermometer, a power-dependent Raman measurement can be performed to directly distill the  $\kappa$  of the material.<sup>132</sup> Despite the widespread and successful applications of OTRS,<sup>131,133,134</sup> particularly in 2D inorganic materials,<sup>135–138</sup> one inherent limitation of OTRS is the need to precisely determine the practically absorbed laser power, which is a challenging task typically aided by theoretical estimations.<sup>139</sup> Moreover, OTRS requires high polarizability of the bonds within the materials, thus more suitable for inorganic crystalline materials with well-defined vibrational modes. Materials with strong fluorescence are not preferred for OTRS because the fluorescence can mask the Raman signal, increasing uncertainty.

#### 2. Photothermal deflection spectroscopy (PDS) and thermal lens spectroscopy (TLS)

Photothermal deflection spectroscopy (PDS) and thermal lens spectroscopy (TLS) are two methods initially conceived for measuring absorption properties but later adapted for thermal characterizations.<sup>129,130,140–142</sup> PDS is predicated on photothermal deflection, a phenomenon where a light beam passing through or near the surface of a heated sample gets deflected. Transient or periodic heating of the sample induces varying temperature gradients within the sample and in the thin gas layer adjacent to the sample surface, the latter case often regarded as the “mirage effect.” The temperature gradient results in a refractive index gradient in the medium that deflects the light passing

through. As depicted in Fig. 2(f), the temperature changes can be detected by the deflected angle of a probe beam traveling through (i.e., collinear mode) or across the surface of (i.e., transverse mode) the sample using a position sensor. Similarly, thermal lens (TL) effect is the deflection of light due to photothermally induced refractive index gradients. Although fundamentally akin to PDS, TL specifically refers to a lens-like refractive index gradient induced by a Gaussian-shaped light beam that converges or diverges the incident light.<sup>140</sup> A diverging TLS is shown in Fig. 2(g). Such a lensing effect can also occur in the medium adjacent to the sample surface, allowing for either transmission mode which measures bulk material properties, or reflection mode which is more sensitive to surface characteristics.

### F. Electrothermal methods

Instead of the photothermal and photoacoustic methods discussed above, where light is the source of heat, electrothermal methods also see a broad application in PV materials.

#### 1. $3\omega$ method

The  $3\omega$  method leverages the relationship between Joule heating and resistivity changes, allowing for the measurement of  $\kappa$  without the need for a temperature sensor. An alternating current of frequency  $\omega$  is supplied to the sample and heats up the sample with a frequency of  $2\omega$ . The voltage across the sample is then detected using a lock-in amplifier, which varies at  $3\omega$  as a result of temperature-induced resistivity change. If the sample is an insulator, a metal film can be deposited onto the surface to serve as a thermal inducer. Information of the thermal properties of the sample is then implicitly contained between Joule heating and temperature fluctuations, and can be extracted from the lock-in signals. Compared with room temperature steady-state thermal measurements, this method is insensitive to blackbody radiation due to a much smaller effective thickness of the sample.<sup>143</sup> It is most commonly applied to bulk, solid materials, but can also extend to liquids.<sup>144,145</sup> Accurate determination of thermal properties relies on solving the heat conduction equation for the specific system. Initially, only relatively simple scenarios such as high-frequency limit or low-frequency limit were solved. Later developments presented a more general solution in the 1D case, which allows simultaneous determination of specific heat and  $\kappa$ .<sup>146</sup> Recently, the finite element method (FEM) has been introduced to achieve more precise results, accommodating more complex experimental scenarios.<sup>147</sup> The  $3\omega$  method is most commonly used in four-point-probe configuration as shown in Fig. 3(a), but it can be applied in other scenarios as well, such as scanning thermal microscopy (SThM).<sup>148,149</sup> Despite that the  $3\omega$  method is commonly used to measure the thermal conductivity of bulk materials, by integrating the lead and electrode onto a chip, the  $3\omega$  method can be used to measure the thermal conductivity of thin film materials with thickness on the order of nanometers.<sup>150</sup>

#### 2. Scanning thermal microscopy (SThM)

SThM is a technique that combines either scanning tunneling microscopy or atomic force microscopy with a thermo-sensitive probe tip, which gives nanometer spatial resolution and microsecond-to-millisecond temporal resolution of the thermal time constant

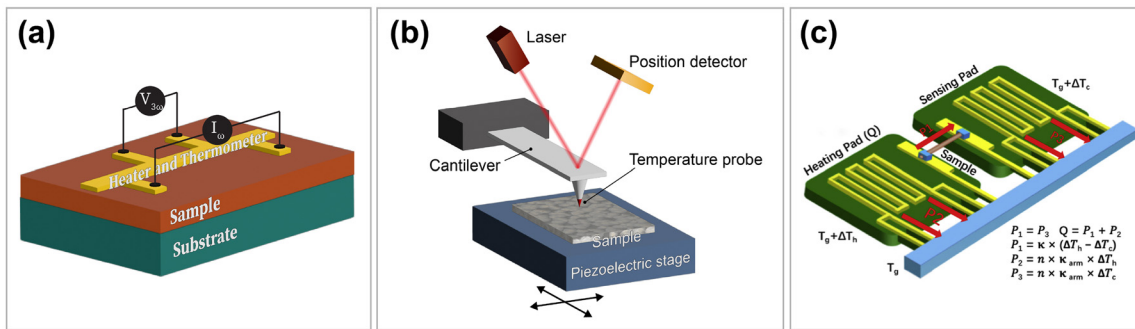


**FIG. 3.** Schematics of electrothermal-based thermal transport measurement techniques. (a)  $3\omega$  method adopting a four-point probe configuration. (b) Scanning thermal microscopy (SThM) method. (c) Suspended-pad method. Reproduced with permission from Song et al., Joule 2(2), 442–463 (2018). Copyright 2018 Elsevier.<sup>161</sup>

[Fig. 3(b)].<sup>151,152</sup> It is suitable for measurement of nanoscale structures or microelectronic devices. The most commonly used probe tips are of thermovoltage types, which generate a voltage at a small thermocouple junction, and thermoresistive types, whose resistivity varies with temperature.<sup>153–155</sup> SThM can be used to either map out the temperature profiles without an external heat supply (i.e., passive mode) or characterize  $\kappa$  by varying probe tip temperature through electrical or laser heating (i.e., active mode).<sup>156,157</sup> Local heat conduction can take several pathways including radiation, diffusive or ballistic conduction, and solid-solid conduction, which heavily depends on the probe parameters and surrounding environment.<sup>158</sup> Thus, one of the most crucial steps of SThM is calibration, which quantitatively relates the amount of heat flow or electrical signals to the local  $\kappa$  of the measured material. Calibration can be performed experimentally by measuring standard samples or by fitting parameters in established models.<sup>148,159,160</sup>

### 3. Suspended-pad method

The suspended pad is a method that specializes in measuring the thermal transport properties of low-dimensional systems, such as nanotubes, nanowires, and 2D materials.<sup>161–165</sup> As illustrated in Fig. 3(c), a nanowire is suspended between two micro-membranes embedded with metal resistance coils, which serve as both the heaters and temperature sensors by adopting the four-point-probe configuration. The heat conduction process in such a system is thus greatly simplified, and the conductivity of a single nanowire can be isolated.<sup>166,167</sup>

### G. Differential scanning calorimetry (DSC)

Apart from all the above-discussed photothermal and electrothermal methods to measure the thermal transport properties, another method that is usually used alongside, differential scanning calorimetry (DSC), is also important. More details on this technique are well covered in other literatures.<sup>168,169</sup> Although DSC typically measures the heat capacity and enthalpy changes and does not provide a direct measurement of how well heat moves through the material, some special configurations and treatments can be applied to measure the heat capacity and  $\kappa$  simultaneously.<sup>170</sup>

## III. 3D METAL HALIDE PEROVSKITES (MHPs)

### A. Introduction to 3D MHP photovoltaics

3D MHPs, characterized by a chemical formula  $ABX_3$  ( $A = Cs^+$ ,  $MA^+$ ,  $FA^+$ ;  $B = Pb^{2+}$ ,  $Sn^{2+}$ ;  $X = Cl^-$ ,  $Br^-$ ,  $I^-$ ;  $MA^+$  = methylammonium,  $FA^+$  = formamidinium), have catalyzed a revolution in photovoltaics. A typical structure of corner-sharing  $[BX_6]^{4-}$  octahedra of 3D MHPs is shown in Fig. 4(a). The power conversion efficiencies of perovskite solar cells (PSCs), with a single planar structure as illustrated in Fig. 4(b), has increased rapidly from an initial value of 3.8%<sup>3</sup> to more than 26%.<sup>171,172</sup> The rapid advancement is attributed to favorable properties including low trap densities,<sup>173</sup> high carrier mobilities,<sup>174</sup> and long carrier diffusion lengths,<sup>175–178</sup> which collectively facilitate efficient light absorption and charge collection. The structural versatility of MHPs allows for the adjustment of their electronic and optical properties by varying their ionic compositions. This tunability extends their utility across various applications beyond photovoltaics, such as light-emitting diodes (LEDs),<sup>179</sup> lasers,<sup>180</sup> and photodetectors.<sup>181</sup> Unlike silicon, which necessitates high-temperature processing, MHPs are appealing due to their potential for lower manufacturing costs<sup>182–185</sup> and their compatibility with flexible substrates [Fig. 4(c)].<sup>186,187</sup>

Despite their advantages, the path toward widespread commercialization of PSCs is still challenged by their environmental instability.<sup>188–190</sup> Specifically, these materials are prone to rapid degradation when exposed to environmental stressors such as moisture, oxygen, and temperature fluctuations [Fig. 4(d)],<sup>190,191</sup> which can lead to decreased efficiency and lifespan of PSCs. To address the stability challenge, considerable research efforts have been directed toward enhancing the robustness of MHPs through chemical modifications and improving device architectures.<sup>192–194</sup> This includes the development of more stable MHP compositions against rapid degradation and the application of advanced encapsulation techniques for protecting MHPs from environmental exposures.<sup>195,196</sup> Additionally, innovations in the interfacial engineering and the optimization of charge transport materials have shown promise in increasing the operational stability and efficiency of PSCs.<sup>197–200</sup>

Thermal stability, in particular, is a key factor that influences the operational reliability of these devices.<sup>201</sup> It was shown that an increase in temperature leads to an exponential decay in the lifetime of PSCs [Fig. 4(e)].  $\kappa$  is an important property that affects how heat generated

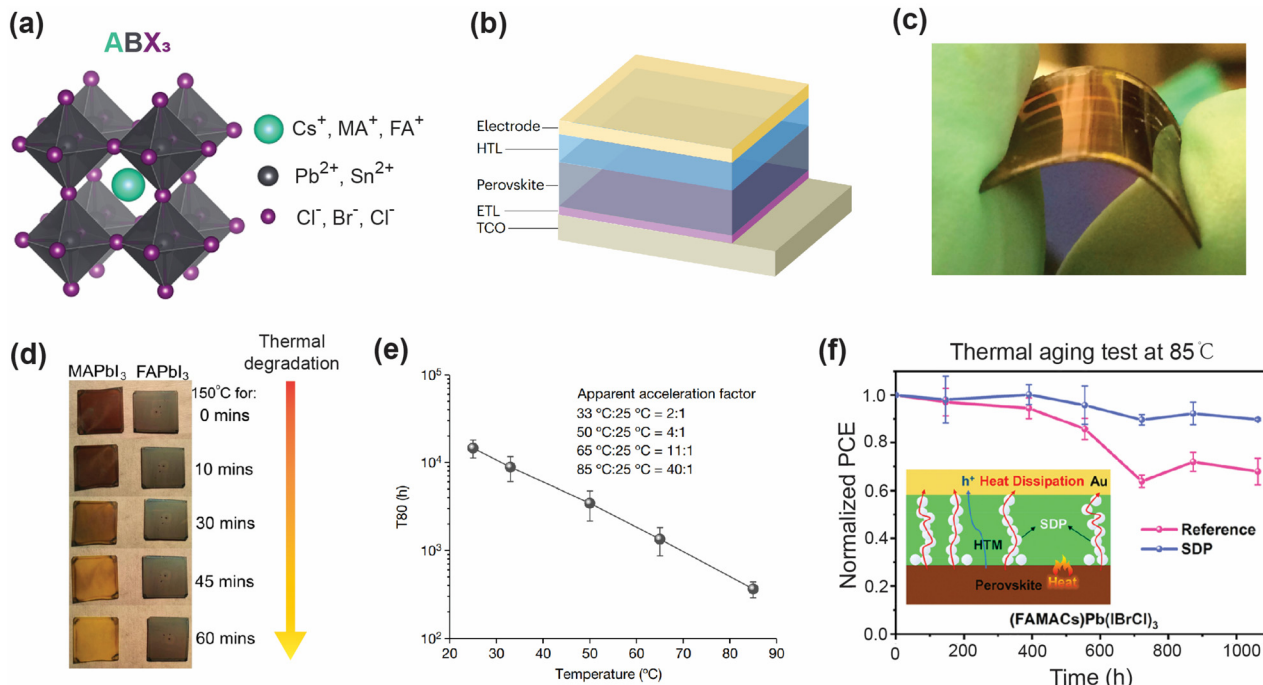


**FIG. 4.** (a) Schematic diagram of the structure of 3D MHPs. (b) Schematic drawing of a regular PSC structure (*n-i-p* type). Reproduced with permission from Jiang and Zhu Nat. Rev. Mater. 9, 399–419 (2024). Copyright 2024 Springer Nature.<sup>172</sup> (c) Photograph of a flexible PSC on PET/ITO substrate. Reproduced with permission from You *et al.*, ACS Nano 8(2), 1674–1680 (2014). Copyright 2014 American Chemical Society.<sup>187</sup> (d) Thermal degradation of MAPbI<sub>3</sub> and FAPbI<sub>3</sub>, when bare spin-coated films of each MHP are heated in air at 150 °C for durations indicated. Reproduced with permission from Eperon *et al.*, Energy Environ. Sci. 7(3), 982–988 (2014). Copyright 2014 RSC Publishing.<sup>191</sup> (e) T80 (time for a solar cell to degrade to 80% of its maximum efficiency) as a function of temperature. Reproduced with permission from Jiang *et al.*, Nature 623(7986), 313–318 (2023). Copyright 2023 Springer Nature.<sup>201</sup> (f) Long-term thermal stability of unencapsulated PSCs based on mixed MHP absorbers with/without silicon dioxide particles (SDP). Reproduced with permission from Pei *et al.*, ACS Energy Lett. 6(9), 3029–3036 (2021). Copyright 2021 American Chemical Society.<sup>204</sup>

within the solar cell is managed, particularly given that the MHP layer serves as the primary heat source in PSCs. Effective thermal management helps prevent thermal degradation of MHPs and maintain PSC efficiency over time.<sup>202–205</sup> Recent advancements in the field have shown that managing the thermal properties of MHPs can significantly improve the fabrication and operational stability of solar cells [Fig. 4(f)].<sup>204,205</sup>

## B. Thermal conductivity measurements of MAPbI<sub>3</sub>

MAPbI<sub>3</sub> holds a pivotal role among the diverse family of 3D MHPs for photovoltaics.<sup>3</sup> Since the structure of MAPbI<sub>3</sub> consists of corner-sharing [PbI<sub>6</sub>]<sup>4−</sup> octahedra extending in all three directions, in most thermal transport studies, this material is treated as isotropic, for which it is amenable to most techniques mentioned in Sec. II. However, it is important to note that each technique comes with its own degree of uncertainty and specific sample requirements. Consequently, the thermal conductivities of MAPbI<sub>3</sub> can vary significantly depending on its form—whether as a single crystal, film, powder, or nanowire—and the measurement method employed. To provide a clear understanding, the discussion on the  $\kappa$  of MAPbI<sub>3</sub> below will be organized based on the different techniques used by various research groups, specifically four-point probe [Fig. 5(a)], SThM [Fig. 5(b)], TDTR/FDTR [Fig. 5(c)], and suspended pad [Fig. 5(d)].

### 1. Four-point probe

The thermal conductivity of MAPbI<sub>3</sub> was first investigated by steady-state four-point probe method [Fig. 5(a)].<sup>37</sup> In contrast to the  $3\omega$ -based four-point probe method mentioned in Sec. II F 1, here the temperature-dependent electrical resistivity was measured to extract the thermal conductivities. Measurements on single crystals of MAPbI<sub>3</sub> revealed an intrinsic, ultralow  $\kappa$  of  $0.5 \text{ W} \cdot \text{m}^{-1} \cdot \text{K}^{-1}$ .<sup>37</sup> This value is significantly lower than the  $\kappa$  of other PV materials: single-crystalline Si has a  $\kappa$  of  $148 \text{ W} \cdot \text{m}^{-1} \cdot \text{K}^{-1}$  and bulk GaAs owns a  $\kappa$  of  $54 \text{ W} \cdot \text{m}^{-1} \cdot \text{K}^{-1}$  at room temperature.<sup>206,207</sup> This significant disparity highlights the importance of thermal management of PSCs. In addition to single-crystal measurements, it is also of great significance to determine the  $\kappa$  of polycrystalline MAPbI<sub>3</sub> thin films. Pisoni *et al.* pressed MAPbI<sub>3</sub> powder and obtained a polycrystalline sample to mimic the effects of the rich grain boundaries in thin films.<sup>37</sup>  $\kappa$  of the pressed polycrystal was determined to be  $0.3 \text{ W} \cdot \text{m}^{-1} \cdot \text{K}^{-1}$ , smaller than that of single crystals but still lies in the same realm. In contrast, the  $\kappa$  of bulk silicon, single-crystal thin-film silicon and amorphous silicon are  $148$ ,  $22$ , and  $1.4 \text{ W} \cdot \text{m}^{-1} \cdot \text{K}^{-1}$ , respectively.<sup>206,208</sup> This intrinsically low  $\kappa$  and the small disparity between single-crystalline and polycrystalline forms point to significant intrinsic phonon scattering in MAPbI<sub>3</sub>, which dominates heat transfer over effects from grain boundaries and defects.

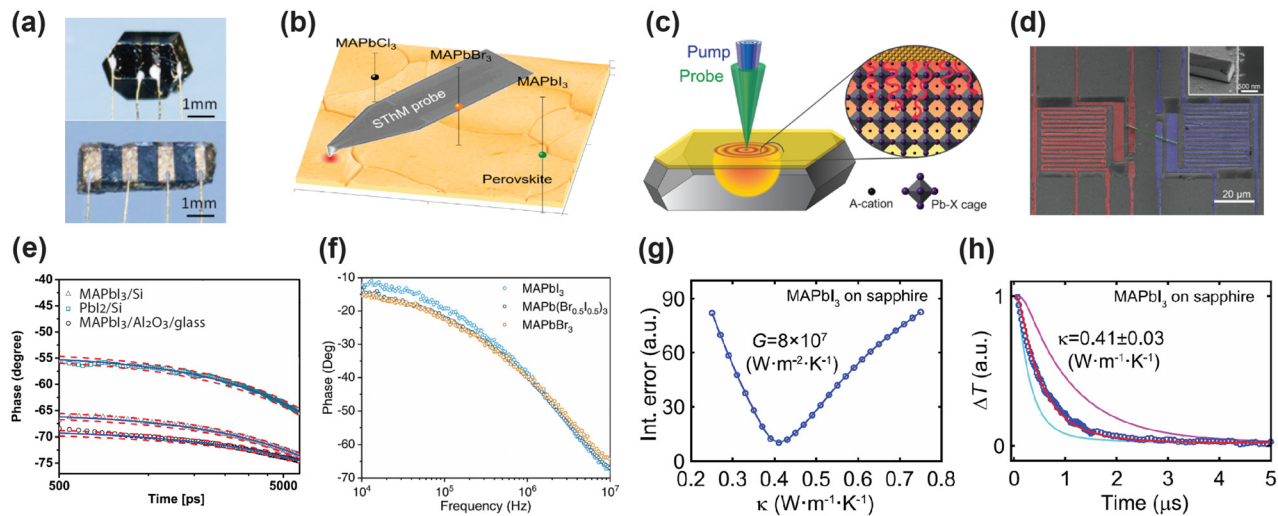


**FIG. 5.** (a) Photographs of a single MAPbI<sub>3</sub> single crystal (top) and polycrystal (bottom) used in electrical and thermal transport measurements with the four-point probe method. Reproduced with permission from Pisoni *et al.*, J. Phys. Chem. Lett. 5(12), 2488–2492 (2014). Copyright 2014 American Chemical Society.<sup>37</sup> (b)–(d) Schematics of (b) SThM. Reproduced with permission from Heiderhoff *et al.*, J. Phys. Chem. C 121, 28306–28311 (2017). Copyright 2017 American Chemical Society. (c) TDTR/FDTR. Reproduced with permission from Elbaz *et al.*, Nano Lett. 17(9), 5734–5739 (2017). Copyright 2017 American Chemical Society. (d) Suspended-pad methods for MAPbI<sub>3</sub> thermal conductivity measurement. Reproduced with permission from Wang *et al.*, Nano Lett. 18(5), 2772–2779 (2018). Copyright 2018 American Chemical Society.<sup>34,210,220</sup> (e) The phase of TDTR signals measured on different substrates at 294 K with a 3-MHz modulation. Solid lines are fitting curves using a heat conduction model considering pulse accumulation. Red-dash lines represent the 90% confidence interval of the film thermal conductivity. Reproduced with permission from Guo *et al.*, J. Phys. Chem. C 120, 6394–6401 (2016). Copyright 2016 American Chemical Society.<sup>214</sup> (f) Representative plots of phase of signals as a function of pump-beam modulation frequency for three samples from FDTR experiments. Reproduced with permission from Wang *et al.*, Adv. Sci. 11, 2401194 (2024). Copyright 2024 Authors, licensed under a Creative Commons Attribution (CC-BY) license.<sup>215</sup> (g) Integrated error as a function of  $\kappa$  under a fixed  $G$  (interfacial thermal conductance between the sample and substrate) value of  $8 \times 10^7$  W·m<sup>-2</sup>·K<sup>-1</sup>.<sup>112</sup> (h) Temperature decay profiles from FEM simulation (red curve) and experiments (blue open circles) using the optimal  $\kappa$  value of  $0.41$  W·m<sup>-1</sup>·K<sup>-1</sup> ( $G$  value is taken as  $8 \times 10^7$  W·m<sup>-2</sup>·K<sup>-1</sup>). The magenta curve shows the computation result using a smaller value for  $\kappa$  ( $0.24$  W·m<sup>-1</sup>·K<sup>-1</sup>), and the cyan curve shows the computation result using a larger value for  $\kappa$  ( $0.69$  W·m<sup>-1</sup>·K<sup>-1</sup>). Reproduced with permission from Li *et al.*, Rev. Sci. Instrum. 93(5), 053003 (2022). Copyright 2022 AIP Publishing.<sup>112</sup>

As a classical  $\kappa$  measurement method, the four-point probe is straightforward to deploy and produces reliable results, but mounting thermocouples and heat sources onto MHPs may cause sample degradation. Additionally, the configuration lacks the compactness for low-temperature measurements within a vacuum chamber and is usually conducted in ambient environment with the risk of sample degradation due to the presence of water and air, which is especially prominent for thin films. In addition, thermal radiation of the material itself may affect the results. In one work by Kovalsky *et al.*, the uncorrected  $\kappa$  was twice as high as the one corrected for thermal radiation loss at room temperature.<sup>209</sup> To this end, non-contact methods under a controlled environment have been employed for  $\kappa$  measurement of MAPbI<sub>3</sub>.

## 2. SThM

R. Heiderhoff *et al.* used the SThM method [Fig. 5(b)] and obtained a  $\kappa$  of  $0.34$  W·m<sup>-1</sup>·K<sup>-1</sup> for single crystals and  $0.33$  W·m<sup>-1</sup>·K<sup>-1</sup> for thin films fabricated by a planar hot-pressing procedure.<sup>210</sup> The small difference within the error margin is consistent with the results obtained by the four-point probe. It should be noted that the thin film consists of a large grain size up to  $10\text{ }\mu\text{m}$ , which is even larger than the phonon MFPs of Si membranes at ambient temperature ( $\sim 400$  nm).<sup>211</sup> Taking advantage of the high spatial resolution, SThM can be further used in thermal imaging. J. Zhao *et al.*

successfully imaged the local thermal strain, revealing the ferroelastic nature of MAPbI<sub>3</sub>.<sup>212</sup>

## 3. TDTR and FDTR

TDTR and FDTR have been adopted in the investigation of  $\kappa$  of MAPbI<sub>3</sub> [Figs. 5(c), 5(e), and 5(f)].<sup>34,213–215</sup> The fitting results across various samples demonstrate strong agreement with the experimental data, regardless of the delay time or the repetition rate [Fig. 5(e)]. The  $\kappa$  of thin-film MAPbI<sub>3</sub> spin-coated on Si substrate was determined to be  $0.3$  W·m<sup>-1</sup>·K<sup>-1</sup>, while the MAPbI<sub>3</sub> film intercalated into an Al<sub>2</sub>O<sub>3</sub> mesoporous scaffold produced a lower  $\kappa$  of  $0.2$  W·m<sup>-1</sup>·K<sup>-1</sup>.<sup>214</sup> In two other independent works, FDTR performed on MAPbI<sub>3</sub> single crystals produced a  $\kappa$  of  $0.34$  and  $0.35$  W·m<sup>-1</sup>·K<sup>-1</sup>, respectively.<sup>34,215</sup> Regardless of thin films or single crystals, the results given by TDTR/FDTR are highly consistent with those given by SThM and slightly lower than those given by the four-point probe. The low  $\kappa$  for the MAPbI<sub>3</sub> embedded in Al<sub>2</sub>O<sub>3</sub> scaffolds arises from the abundant grain boundaries due to grain sizes down to tens of nanometers.

A TDTR-based study attempted to use a simplified model to extract  $\kappa$  from time-dependent reflectance.<sup>213</sup> However, despite a minimal fitting error, a  $\kappa$  value of  $11.2$  W·m<sup>-1</sup>·K<sup>-1</sup> was obtained for MAPbI<sub>3</sub> thin films,<sup>213</sup> which is more than one order of magnitude higher than all currently reported room-temperature  $\kappa$  of MAPbI<sub>3</sub>.

Although the low repetition rate (1000 Hz) of the laser ensured that the material had sufficient time to fully return to its initial state, the data used in fitting only covered the first 6 ns, several orders of magnitude shorter than the time of heat dissipation.<sup>112</sup> Missing data points during the subsequent cooling process may compromise the accuracy of the fitting results to a certain extent.

#### 4. Vibrational-pump visible-probe (VPVP)

Li *et al.* developed a method dubbed VPVP spectroscopy, a variant of TDTR, where the  $\kappa$  can be obtained by directly fitting transient changes in reflectance or transmittance without the use of a lock-in amplifier for phase detection.<sup>112</sup> Utilizing an electronically triggered probe laser, the maximum delay window in VPVP is up to 1 ms. Note that the nanosecond time resolution is sufficient for resolving the slow thermal dissipation process in MAPbI<sub>3</sub> and other MHPs.

One innovation is that VPVP does not involve a metal transducer. Instead, the MHP thin film itself serves as both the heat source and temperature monitor. By pumping the vibrational modes of the MA<sup>+</sup> cations with mid-infrared laser pulses, the lattice temperature increases impulsively on a sub-ns timescale, much shorter than the timescale of thermal dissipation. Meanwhile, the transmittance of MHPs near the bandgap is used to monitor the temperature change ( $\Delta T$ ) as a function of time. A 1D thermal transport model can be established with only two independent parameters: the  $\kappa$  of MAPbI<sub>3</sub> and the interfacial conductance  $G$  of the MAPbI<sub>3</sub>/substrate interface. Furthermore, analysis reveals that when  $G$  exceeds 10<sup>6</sup> W·m<sup>-2</sup>·K<sup>-1</sup>, the transmittance over time becomes solely a function of  $\kappa$ , and the error function reaches a minimum when  $\kappa$  most closely approximates the true value [Fig. 5(g)]. Within the framework of this simplified model, the fitted  $\Delta T$ -vs-time curve exhibits substantial agreement with experimental measurements covering the whole cooling process with a high sensitivity to  $\kappa$  [Fig. 5(h)]. Depending on the type of substrate, the VPVP-inferred  $\kappa$  of MAPbI<sub>3</sub> ranges from 0.30 to 0.51 W·m<sup>-1</sup>·K<sup>-1</sup>, which agrees with values extracted from TDTR/FDTR experiments.

#### 5. Other experimental methods

Other techniques have also been utilized for measuring the  $\kappa$  of MAPbI<sub>3</sub>, when the sample morphology is adjusted to suit experimental requirements, *i.e.*, single crystal samples for the LFA, thin film samples for chip-based 3 $\omega$  method, and nanowire samples for the suspended pad method. Both LFA and chip-based 3 $\omega$  method yielded  $\kappa$  ranging from 0.30 to 0.39 W·m<sup>-1</sup>·K<sup>-1</sup><sup>12,16-219</sup> whereas the suspended pad method produced a  $\kappa$  of 0.22 W·m<sup>-1</sup>·K<sup>-1</sup> for MAPbI<sub>3</sub> nanowires, similar to the reduction from single crystals to thin films [Fig. 5(d)].<sup>220</sup> Unlike other methods, where  $\kappa$  shows a weak correlation with sample size, the measurement results from the 3 $\omega$  method indicated that the  $\kappa$  of the MHP film varies significantly with thicknesses. Specifically, when the film thicknesses are 65, 80, and 100 nm, the  $\kappa$  were 0.31, 0.44, and 0.59 W·m<sup>-1</sup>·K<sup>-1</sup>, respectively.<sup>150</sup> Such a variation in the thermal conductivity was attributed to the difference in carefully tuned crystallite size, thus the density of grain boundaries.

Different from the methods discussed above, Shen *et al.* used photoluminescence (PL) spectroscopy to obtain the  $\kappa$  of MAPbI<sub>3</sub>.<sup>221</sup> Their measurement was predicated on the fact that an increase in the bandgap of MAPbI<sub>3</sub> with rising temperature not only causes changes

in transmittance but also induces a blue shift in the PL spectra, which is linearly proportional to the amplitude of temperature rise. As a steady-state, transducer-free measurement, a presumption behind their experiments is that energy released through radiation constitutes only a small part of the energy from the incident pump light, so the primary energy dissipation is through non-radiative heat transfer process. The measurements involved specially prepared MAPbI<sub>3</sub> single-crystal flakes suspended on a SiO<sub>2</sub>/Si substrate prepatterned with an array of holes. By parking the excitation beam at the center of the floating region, heat transfer only occurs along the radial direction. It was further assumed that the temperature of the MHP outside the suspended region is always identical to that of the substrate acting as a heat sink. Under these conditions, the  $\kappa$  can be written as  $\kappa = \gamma(Q/\Delta T)$ ,<sup>222</sup> where  $\gamma$  is a structure factor,  $Q$  is the heating power, and  $\Delta T$  is the temperature difference between the excitation center and the heat sink. Since  $\Delta T$  is linear to the excitation power, the equation can be further written as  $\kappa = \gamma(Q_1 - Q_2)/(T_1 - T_2)$ , where  $T_1$  and  $T_2$  are the temperatures under the heating power  $Q_1$  and  $Q_2$ , respectively. Using these equations, Shen *et al.* obtained a  $\kappa$  of 0.14 W·m<sup>-1</sup>·K<sup>-1</sup> for MAPbI<sub>3</sub> single crystals. This value is lower than those obtained by other techniques. We note that this method is similar to OTRS, which has been primarily employed to measure the  $\kappa$  of 2D materials with good accuracy.<sup>222-225</sup> One potential source of experimental error can be the heat flow in the vertical direction compounded by the PL photon recycling in the sample, which can alter the observed spectral location of PL.

#### 6. Numerical simulations

Aside from experimental efforts, numerical techniques such as molecular dynamics (MD) simulations are widely used to predict the  $\kappa$  of materials.<sup>226-230</sup> Using the Green-Kubo relation, the  $\kappa$  can be calculated from equilibrium MD simulations as<sup>231,232</sup>

$$\kappa = \frac{1}{3Vk_B T^2} \int_0^\infty \langle \dot{\mathbf{w}}(0) \cdot \dot{\mathbf{w}}(t) \rangle dt. \quad (7)$$

Here,  $k_B$  is the Boltzmann constant,  $T$  is the temperature,  $V$  is the volume of the simulation cell,  $\dot{\mathbf{w}}$  is the heat current, and

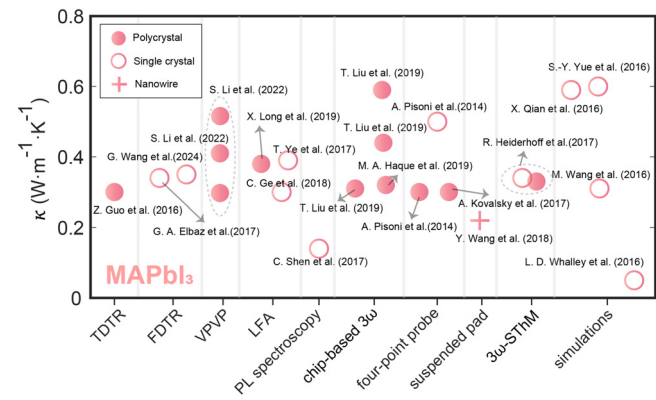


FIG. 6. Summary of reported thermal conductivities of MAPbI<sub>3</sub> measured with different methods (simulations include both MD and DFT). Detailed values and references of the data points are summarized in Table I.

$\langle \dot{\mathbf{w}}(0) \cdot \dot{\mathbf{w}}(t) \rangle$  denotes the averaged heat current autocorrelation function.  $\dot{\mathbf{w}}$  is defined as the time derivative of the first-order energy moment with respect to the atomic position  $\mathbf{r}_i$ ,

$$\dot{\mathbf{w}} = \frac{d}{dt} \sum_i E_i \mathbf{r}_i, \quad (8)$$

where  $E_i$  is the total energy of atom  $i$ .

MD simulations effectively reproduced the experimental results of MAPbI<sub>3</sub>, with  $\kappa$  determined to range from 0.3 to 0.6 W·m<sup>-1</sup>·K<sup>-1</sup>.<sup>202,231,233</sup> Another benefit of using theoretical calculations is that the anisotropic  $\kappa$  along different crystal orientations can be calculated straightforwardly,<sup>202</sup> a task often more challenging for experimentalists.

Density functional theory (DFT) is a theoretical method widely employed to predict the electronic and vibrational properties of semiconductors. Using DFT-based anharmonic lattice dynamics calculations, the average group velocity and lifetimes of phonons can be deduced from the slope and width of the phonon dispersion relations. With the calculated heat capacity and phonon–phonon scattering rates, the  $\kappa$  can be obtained from the solution of the Boltzmann transport equation (BTE) using these physical quantities. However, one report that is based on DFT calculation yielded a  $\kappa$  of

TABLE I. Summary of thermal conductivities of MAPbI<sub>3</sub>.

Material form	$\kappa$ (W·m <sup>-1</sup> ·K <sup>-1</sup> )	Method	Reference
SC	0.5	Four-point probe	37
PC	0.3	Four-point probe	37
PC	0.3	Four-point probe	209
SC	0.34 ± 0.12	SThM	210
Film	0.33 ± 0.12	SThM	210
Film (on Si)	11.2 ± 0.8	TDTR	213
Film (on Sapphire)	0.41 ± 0.03	VPVP	112
Film (on quartz)	0.3 ± 0.02	VPVP	112
Film (on CaF <sub>2</sub> )	0.51 ± 0.02	VPVP	112
Film (in mesostructured Al <sub>2</sub> O <sub>3</sub> )	0.2	TDTR	214
Film (on Si)	0.3	TDTR	214
SC	0.34 ± 0.08	FDTR	34
SC	0.35 ± 0.11	FDTR	215
SC	0.14 ± 0.02	PL spectroscopy	221
SC	0.3	LFA	217
PC	0.38	LFA	218
SC	0.39	LFA	216
Nanowire	0.22	Suspended pad	220
Film	0.32 ± 0.03	Chip-based 3ω	219
Film (65 nm)	0.31 ± 0.03	Chip-based 3ω	150
Film (80 nm)	0.44 ± 0.03	Chip-based 3ω	150
Film (100 nm)	0.59 ± 0.04	Chip-based 3ω	150
SC	0.59	MD	231
SC	0.6	MD	233
SC	0.31	MD	202
SC	0.05	DFT	234

0.05 W·m<sup>-1</sup>·K<sup>-1</sup>,<sup>234</sup> which is significantly lower than values obtained from other experimental or numerical methods. The deviation observed in DFT compared to MD simulations warrants further investigation.

In Fig. 6 and Table I, we summarize the  $\kappa$  values of MAPbI<sub>3</sub> and the associated methods reported in the literature. Most experimental methods and theoretical calculations show that the  $\kappa$  of MAPbI<sub>3</sub> is orders of magnitude lower than that of other PV materials. It is also discovered that the thermal expansion coefficient of MAPbI<sub>3</sub> is an order of magnitude higher than that of inorganic PV materials,<sup>217</sup> which may cause delamination of PSCs under variation of the operating temperatures, thus weakening their long-term stability.

### C. Constituent-dependent thermal conductivity of MAPbI<sub>3</sub>

One of the major advantages of MHPs over other semiconductor materials is their high degree of chemical composition tunability. In this context, tuning the chemical composition of MHPs can inform on the origins behind the ultralow  $\kappa$  of MAPbI<sub>3</sub>. One of the most straightforward approaches to isolate and quantify the effect of MA<sup>+</sup> on thermal transport is to compare the  $\kappa$  of MAPbI<sub>3</sub> with that of CsPbI<sub>3</sub>.<sup>209</sup> Although the  $\kappa$  of CsPbI<sub>3</sub> (0.43 W·m<sup>-1</sup>·K<sup>-1</sup>) is higher than that of MAPbI<sub>3</sub>, it remains an order of magnitude lower than that of other inorganic semiconductors. This result suggests that while vibrations of the organic MA<sup>+</sup> do partly contribute to the low  $\kappa$ , the low  $\kappa$  is common to all MHPs and is not unique to organic–inorganic hybrid ones.

When MHPs are subject to A-site cation mixing of Cs<sup>+</sup>, FA<sup>+</sup>, and MA<sup>+</sup>, the replacement of B-site Pb<sup>2+</sup> with Sn<sup>2+</sup>, and the interchange of halide anion X<sup>-</sup> (Cl<sup>-</sup>, Br<sup>-</sup>, and I<sup>-</sup>), their  $\kappa$  are consistently lower than 1 W·m<sup>-1</sup>·K<sup>-1</sup>. Figure 7 and Table II summarize the  $\kappa$  values for MHPs published in the literature found by the authors.<sup>34,210,215,235–242</sup> Their similarity implies that the inorganic octahedral framework and the phonons corresponding to the motions of B and X atoms should be responsible for the low  $\kappa$  of MAPbI<sub>3</sub> and other MHPs in general. From the data points in Fig. 7, three key trends emerge: (1) the  $\kappa$  of all-inorganic MHPs are generally higher than

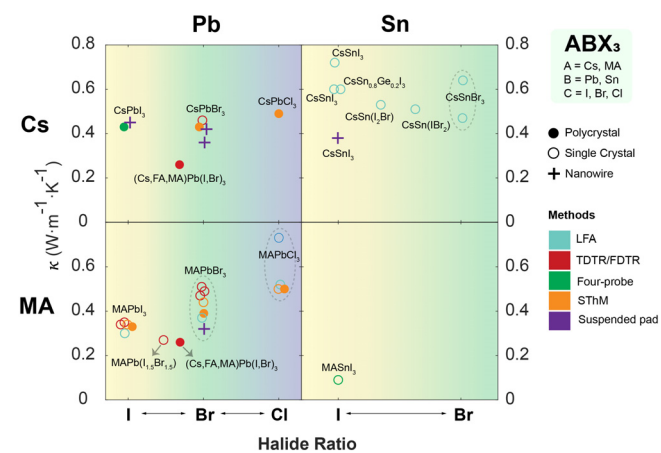


FIG. 7. Summary of thermal conductivities of 3D MHPs (ABX<sub>3</sub>) with varying cations, halides and mixing ratios. Values and references of the data points are summarized in Table II.

TABLE II. Summary of thermal conductivities of 3D perovskites other than MAPbI<sub>3</sub>.

Materials	Form	$\kappa$ (W·m <sup>-1</sup> ·K <sup>-1</sup> )	Method	Reference
MASnI <sub>3</sub>	SC	0.09 ± 0.01	Four-point probe	448
MAPbBr <sub>3</sub>	SC	0.44 ± 0.08	SThM	210
MAPbBr <sub>3</sub>	Film	0.39 ± 0.05	SThM	210
MAPbCl <sub>3</sub>	SC	0.5 ± 0.05	SThM	210
MAPbCl <sub>3</sub>	Film	0.5 ± 0.12	SThM	210
CsPbI <sub>3</sub>	PC	0.43	Four-point probe	209
CsPbI <sub>3</sub>	Nanowire	0.45 ± 0.05	Suspended pad	235
CsPbBr <sub>3</sub>	Nanowire	0.42 ± 0.04	Suspended pad	235
CsSnI <sub>3</sub>	Nanowire	0.38 ± 0.04	Suspended pad	235
MAPbBr <sub>3</sub>	SC	0.37	LFA	217
MAPbCl <sub>3</sub>	SC	0.52	LFA	217
MAPbBr <sub>3</sub>	Nanowire	0.32	Suspended pad	220
CsPbBr <sub>3</sub>	Nanowire	0.36	Suspended pad	220
CsPbBr <sub>3</sub>	Film	0.43 ± 0.03	SThM	236
CsPbCl <sub>3</sub>	Film	0.49 ± 0.04	SThM	237
(Cs,FA,MA)Pb(I,Br) <sub>3</sub>	Film	0.26 ± 0.03	TDTR	238
CsSnI <sub>3</sub>	SC	0.72	LFA	239
CsSnBr <sub>3</sub>	SC	0.47	LFA	240
CsSnBr <sub>3</sub>	SC	0.64	LFA	241
CsSnBr <sub>2</sub> I	SC	0.51	LFA	241
CsSnBrI <sub>2</sub>	SC	0.53	LFA	241
CsSnI <sub>3</sub>	SC	0.6	LFA	241
MAPbBr <sub>3</sub>	SC	0.51 ± 0.12	FDTR	34
MAPbCl <sub>3</sub>	SC	0.73 ± 0.18	FDTR	34
CsPbBr <sub>3</sub>	SC	0.46 ± 0.12	FDTR	34
FAPbBr <sub>3</sub>	SC	0.49 ± 0.12	FDTR	34
MAPbBr <sub>3</sub>	SC	0.47 ± 0.09	FDTR	215
MAPbI <sub>3</sub>	SC	0.35 ± 0.11	FDTR	215
MAPbBr <sub>1.5</sub> I <sub>1.5</sub>	SC	0.27 ± 0.07	FDTR	215

those of organic-inorganic hybrid MHPs; (2) for MHPs containing different inorganic cages ( $[BX_6]^{4-}$ ), the trend in  $\kappa$  is as follows:  $\kappa_{\text{Cl}} > \kappa_{\text{Br}} > \kappa_{\text{I}}, \kappa_{\text{Sn}} > \kappa_{\text{Pb}}$ ; (3) the  $\kappa$  of MHPs with mixed A<sup>+</sup> cations or mixed halides are lower than those of their unmixed counterparts. The first trend has been attributed to resonant scattering by the organic cations,<sup>37,209,220</sup> a phenomenon also reported in other organic-inorganic hybrid materials, and thermoelectric materials with similar cage networks,<sup>243</sup> where thermal conductance is greatly suppressed due to the presence of organic constituents.<sup>227,244,245</sup> As for the second trend, one potential origin is the different bond strengths resulting from the differences in oxidation potential and atomic radii. At room temperature, the bond dissociation energies of the B-X bonds are as follows: 350 kJ·mol<sup>-1</sup> for Sn-Cl, 337 kJ·mol<sup>-1</sup> for Sn-Br, 235 kJ·mol<sup>-1</sup> for Sn-I, 301 kJ·mol<sup>-1</sup> for Pb-Cl, 248 kJ·mol<sup>-1</sup> for Pb-Br, and 194 kJ·mol<sup>-1</sup> for Pb-I.<sup>246</sup> The strength of these chemical bonds influences the mechanical properties of the MHPs, such as the elastic modulus, consequently affecting the  $\kappa$ .<sup>247</sup> Regarding the third trend, the diversity of chemical components in a system increases its entropy, and one characteristic of high-entropy compounds is their low  $\kappa$ . This property is widely exploited in the field of thermoelectrics.<sup>248-250</sup>

#### D. Temperature-dependent thermal conductivity of MAPbI<sub>3</sub>

The Debye model is widely used to bridge the macroscopic  $\kappa$  and microscopic phonon behaviors, where  $\kappa$  can be approximated as<sup>37</sup>

$$\kappa = CT^3 \int_0^{\theta_D} \tau(x) \left[ \frac{x^4 e^x}{(e^x - 1)^2} \right] dx. \quad (9)$$

Here,  $\theta_D$  is the Debye temperature,  $C = (k_B/2\pi^2 v_s)(k_B/\hbar)^3$ , and  $x = \hbar\omega/k_B T$ , where  $k_B$  is the Boltzmann constant,  $\hbar$  is the reduced Planck's constant,  $\tau$  is the average phonon lifetime, and  $v_s$  is the average speed of sound.  $\tau$  can be approximated using the Callaway's approach, with different phonon scattering mechanisms summed up as<sup>251</sup>

$$\tau^{-1} = \sum_i \tau_i^{-1}. \quad (10)$$

There are several common scattering mechanisms: grain boundaries, point defects, and Umklapp scattering.<sup>252</sup> The corresponding phonon lifetimes can be written as  $\tau_B^{-1} = \frac{v_s}{d}$ ,  $\tau_{PD}^{-1} = \frac{V}{4\pi v_s^3} B_{PD}^2 \omega^4$ , and

$\tau_U^{-1} = \frac{\hbar^2}{Mv^2 B_{PD}} \omega^2 T \exp\left(-\frac{\theta_D}{3T}\right)$ , where  $d$  is the average crystallite size,  $V$  is the unit-cell volume,  $B_{PD}$  is a fitting parameter,  $M$  is the average atomic mass, and  $\gamma$  is the Grüneisen parameter. For MAPbI<sub>3</sub>, since MA<sup>+</sup> has vibrational modes such as rotation, another resonant scattering term in the form of  $\tau_R^{-1} = \frac{\omega^2 \omega_0^2}{(\omega^2 - \omega_0^2)^2}$  was added in some studies, where  $\omega_0$  is the vibrational frequency of the organic cation responsible for the resonant scattering.<sup>37,209,253</sup>

For solids, especially single crystals,  $\kappa$  initially increases and then decreases with rising temperature. This occurs because in the low-temperature region, as temperature rises, more phonons are activated to conduct thermal energy. As phonon density continues to increase, phonon–phonon interactions intensify rapidly, leading to predominant Umklapp scattering, which ultimately causes  $\kappa$  to decrease with increased temperature. In most studies, the temperature-dependent  $\kappa$  of MHPs, including both single crystals and thin films, follows this trend [see Fig. 8(a) for an example]. However, the scattering mechanisms contributing to the low  $\kappa$  can differ. Given the large grain size and low impurity densities in single crystals, Pisoni *et al.* utilized only the resonant term and the Umklapp scattering term to fit the temperature-dependent  $\kappa$ , obtaining a curve that closely aligns with the experimental data.<sup>37</sup> In contrast, Guo *et al.* chose three terms to incorporate effects from grain boundaries, point defects, and Umklapp scattering, the results of which matched their experimental data.<sup>214</sup> Kovalsky *et al.* found that unless the temperature falls below 10 K, the inclusion of grain boundaries, point defect, and resonant scattering terms does not significantly alter the temperature-dependent  $\kappa$  curve [Fig. 8(b)].<sup>209</sup> It implies that Umklapp scattering starts to dominate heat transfer even at very low temperatures, suggesting strong phonon–phonon coupling in MAPbI<sub>3</sub> across a broad range of temperatures.

While there is consensus on the general tendency for the  $\kappa$  of MAPbI<sub>3</sub> to decrease with increasing temperature (above 100 K), variation in  $\kappa$  near the phase transition temperature differs across studies.

There is a sudden increase in  $\kappa$  after the tetragonal-to-cubic phase transition around 330 K measured by SThM,<sup>210</sup> which was also predicted by MD simulations.<sup>231</sup> In all studies involving the LFA, no change near the tetragonal-to-cubic phase transition has been observed.<sup>216–218</sup> As for the orthorhombic-to-tetragonal phase transition around 160 K, a decrease in  $\kappa$  was found by TDTR while it was not captured by the four-point probe method.<sup>37,209,214</sup> It is not clear why different methods give different trends and further research is warranted. It should be noted that in some specific cases, such as MHPs in Al<sub>2</sub>O<sub>3</sub> mesostructured films, the  $\kappa$  shows a monotonic increase with temperature in low-temperature regions (up to room temperature).<sup>214</sup> This glass-like thermal transport behavior mainly results from the nanostructure and is not an intrinsic property of MHPs.<sup>254</sup>

#### IV. QUASI-2D METAL HALIDE PEROVSKITES

##### A. Introduction to 2D MHPs

In this section, we will discuss the thermal transport properties of low-dimensional MHPs, primarily focusing on 2D MHPs due to their technological importance. Systematic investigations on the dependence of temperature,<sup>43,255</sup> organic spacer,<sup>256–259</sup> and inorganic layer thickness<sup>258,260–262</sup> revealed that thermal transport in layered 2D MHPs share some characteristics with superlattices<sup>263–265</sup> and self-assembled monolayers,<sup>266–268</sup> although 2D MHPs exhibit behaviors unique to themselves as a result of their chemical and structural diversities.

MHPs with reduced dimensionalities (i.e., 2D, 1D, and 0D) play an important role in the MHP family due to their favorable optoelectronic properties and diverse applications, including photovoltaics.<sup>269–271</sup> Although the record conversion efficiency of 2D MHP-based PSCs (20%)<sup>272</sup> is lower than the state-of-art 3D MHP-based PSCs (~26%),<sup>8,273</sup> the advantages of the 2D form have been extensively reported,<sup>270,274,275</sup> especially their improved moisture stability owing to the inclusion of hydrophobic organic cations.<sup>271,274,276</sup> Moreover, instead of serving as the light-absorbing layer in PSCs, 2D

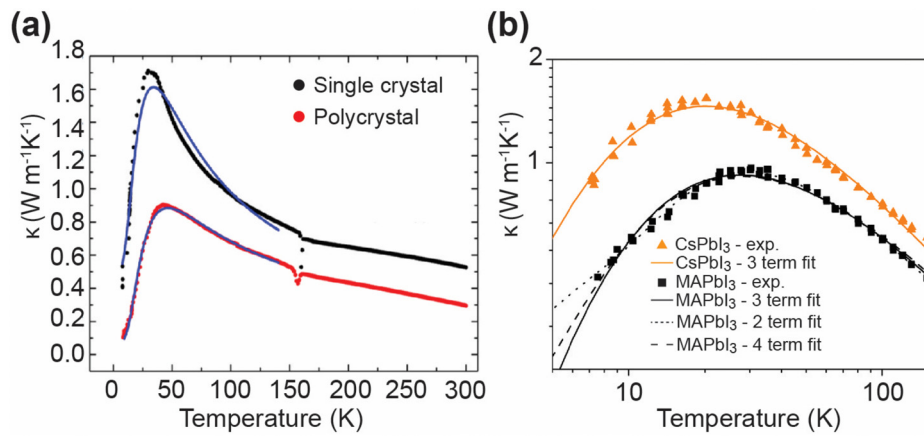


**FIG. 8.** (a) Temperature dependence of thermal conductivities of single-crystalline (black) and polycrystalline (red) MAPbI<sub>3</sub> samples. Blue lines are obtained from the theoretical model. Reproduced with permission from Pisoni *et al.*, J. Phys. Chem. Lett. **5**(14), 2488–2492 (2014). Copyright 2014 American Chemical Society.<sup>37</sup> (b) Thermal conductivities of MAPbI<sub>3</sub> and CsPbI<sub>3</sub> plotted on a logarithmic scale. Solid lines represent model fitting considering three phonon scattering mechanisms (grain boundaries, point defects, and Umklapp scattering). Dotted lines represent modified model containing two scattering terms (both Umklapp and resonant scattering). Dashed lines represent the model taking into account all four relevant phonon scattering mechanisms. Reproduced with permission from Kovalsky *et al.*, J. Phys. Chem. C **121**, 3228–3233 (2017). Copyright 2017 American Chemical Society.<sup>209</sup>

MHPs have also been exploited as interfacial layers to improve the charge collection characteristics and stability of 3D MHP-based PSCs.<sup>277–279</sup> In recent years, there has been a surge in publications on 2D MHPs<sup>13,280–283</sup> not only focusing on their potential for photovoltaics but also exploring other applications such as photodetection,<sup>284</sup> LEDs,<sup>13,285–287</sup> and thermoelectrics.<sup>288</sup> Concurrently, thermal management of 2D MHPs becomes increasingly important. For instance, efficient heat dissipation prompts longer-lifetime LEDs, and effective suppression of heat flow can maintain sizeable temperature gradients for improving thermoelectric performances [Fig. 9(a)]. The plethora of available choices of organic spacers provides a playground for tuning the material properties and device performance by adjusting the crystal structures, interlayer distances, and octahedral connectivity modalities.<sup>289</sup>

The general formulas of (100)-oriented and (110)-oriented 2D MHPs are  $A'_2A_{n-1}B_nX_{3n+1}$  and  $A'A_{n-1}B_nX_{3n+1}$ , respectively, where  $A'$  is a 1+ or 2+ cation, A is a 1+ cation, B is a divalent metallic cation (e.g.,  $Pb^{2+}$ ,  $Sn^{2+}$ ,  $Ge^{2+}$ ,  $Cu^{2+}$ , or  $Cd^{2+}$ ), and X is a halide anion ( $Cl^-$ ,  $Br^-$ , or  $I^-$ ). The less common (111)-oriented 2D MHPs have a general formula of  $A'_{n+1}B_nX_{3n+3}$ .<sup>290</sup> The structures of (100)-, (110)-, and (111)-oriented 2D MHPs are displayed in Fig. 9(b). The (100)-oriented type, with inorganic layers comprising corner-sharing  $[BX_6]^{4-}$  octahedra separated by interdigitating organic cations, are mostly investigated due to their easier processability and higher charge mobility. Based on the selected organic spacers, (100)-oriented 2D MHPs may adopt two different phases: the Ruddlesden-Popper (RP) phase, featuring monovalent interlayer organic spacers, and the Dion-Jacobson (DJ) phase, characterized by divalent organic spacers. The variation in organic spacers leads to distinct stacking configurations of each layer as shown

in Fig. 9(b). Some commonly adopted spacers are presented in Fig. 9(b), although a substantially larger variety of cations has been utilized for making 2D MHPs, which has been summarized in an excellent review article.<sup>289</sup>

In addition to the facile fabrication,<sup>270,274</sup> tunable bandgaps,<sup>13,291–293</sup> and efficient light absorption properties<sup>13</sup> of 2D MHPs, their ultralow  $\kappa$  (even lower than the already-low  $\kappa$  of their 3D counterparts) are garnering increasing attention.<sup>38,258,260</sup> Although PSCs may benefit from the low  $\kappa$  of MHPs through longer-lived hot carriers arising from the hot-phonon bottleneck effect,<sup>294</sup> slow heat dissipation raises concerns on thermal degradation under high operating temperature (up to 85 °C) of PSCs.<sup>33</sup> This delicate trade-off necessitates better thermal management and hence a deeper understanding of thermal transport in 2D MHPs. Additionally, due to the strong excitonic effect in 2D MHPs, they are also extensively incorporated into LEDs, where heat generation can be more prominent. As we discuss below, while there have been systematic studies delving into certain aspects of the thermal transport properties in low-dimensional MHPs, a comprehensive understanding of all influencing factors and a thorough comparative discussion of existing research are still lacking.<sup>38,255–258,260,261,295</sup>

## B. Ultralow thermal conductivities exceeding bulk limits

Ultralow  $\kappa$  of a series of 2D MHP films, ranging from 0.1 to 0.2 W·m<sup>-1</sup>·K<sup>-1</sup>, were measured by Giri *et al.* using TDTR.<sup>38</sup> Notably, unlike in highly doped semiconductors and metals where charge carriers carry a significant amount of heat,<sup>296–298</sup> phonons are the dominant heat carriers in 2D MHPs. The exclusive contribution of

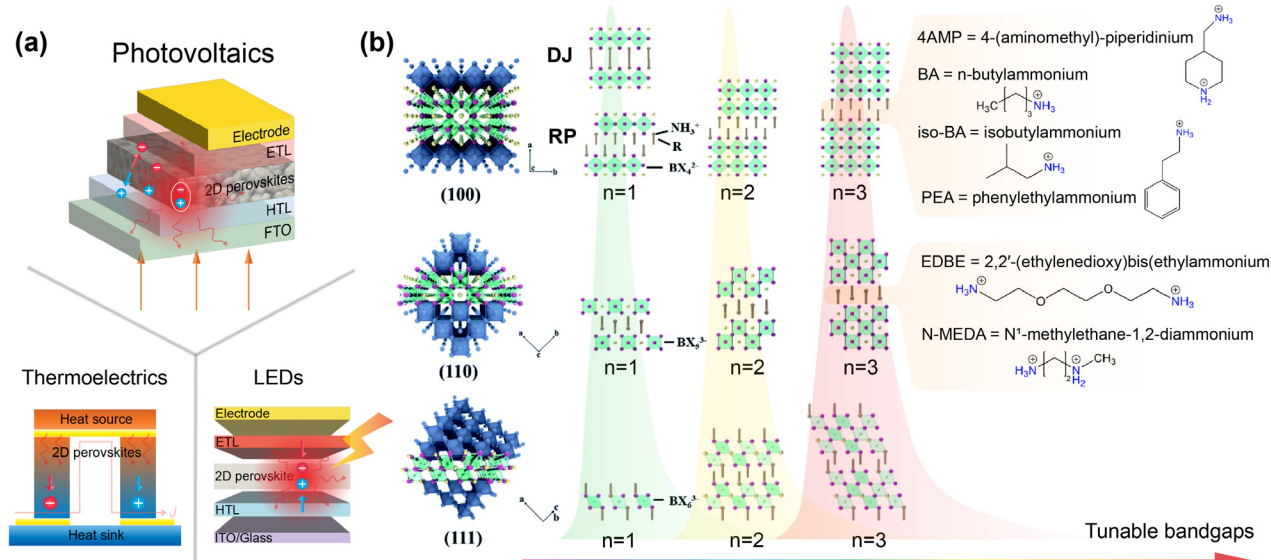


**FIG. 9.** (a) Upper panel: schematic of a representative PV application of 2D MHPs with free carriers and heat generated simultaneously following the absorption of light. ETL: electron transport layer. HTL: hole transport layer. FTO: fluorine-doped tin oxide. Lower panel: thermoelectrics adopting 2D MHPs with efficient charge transfer and suppressed thermal transport between the heat source and sink (left). LEDs enabled by the strong excitonic effect in 2D MHPs and heat accumulation from the carrier recombination (right). (b) Crystal structures of (100)-, (110)-, and (111)-oriented 2D MHPs with tunable bandgaps achieved by varying the thickness of the inorganic layers (e.g., from  $n = 1$  to  $n = 3$ ). Reproduced with permission from Liu *et al.*, Sustainable Energy Fuels 5, 3950–3978 (2021). Copyright 2021 Royal Society of Chemistry.<sup>280</sup> Some typical organic spacers that provide feasible approaches to modify the materials such as the structure orientation are also presented. Reproduced with permission from Mao *et al.*, J. Am. Chem. Soc. 141, 1171–1190 (2019). Copyright 2019 American Chemical Society.<sup>290</sup>

phonons is even more pronounced in the cross-plane thermal transport in 2D MHPs due to the strong confinement effect on charge carriers imposed by the quantum-well-like structures.<sup>19,299</sup> The low  $\kappa$  in 2D MHPs partially comes from similar phonon dispersions to their 3D counterparts, characterized by low phonon group velocities and short phonon lifetimes, which originate from enhanced phonon scattering as a result of the significant overlap between acoustic and optical phonon branches.<sup>123,260,300,301</sup> Moreover, the ultralow  $\kappa$  of 2D MHPs exceeds the minimum limit of disordered crystals predicted by the Cahill–Watson–Pohl (CWP) model<sup>38</sup>

$$\kappa_{\min} = \frac{1}{6} n_{\text{atom}}^{1/3} \sum_j \int_0^{\Theta_j} \frac{\hbar^2 \omega^2}{k_B T^2} \frac{e^{\hbar\omega/k_B T}}{(e^{\hbar\omega/k_B T} - 1)^2} d\omega, \quad (11)$$

where the  $\kappa$  is calculated by summing over all  $j$ th phonon modes (one longitudinal and two transverse),  $n_{\text{atom}}$  is the atomic density,  $\omega$  is the phonon angular frequency, and  $\Theta_j = v_j(6\pi^2 n)^{1/3}$  is the cutoff frequency for mode  $j$  with a phonon group velocity  $v_j$ .<sup>302</sup>

The  $\kappa$  of 2D MHPs are found to be almost an order of magnitude lower than the predicted minimum values, the discrepancy of which is much more pronounced compared with their 3D analog.<sup>38</sup> Such unexpectedly low  $\kappa$  has been attributed to diffuse phonon scattering occurring at the organic–inorganic interfaces caused by a large mismatch in acoustic impedances<sup>261</sup> (reaching about 25.1 in a literature report<sup>303</sup>). A possible explanation for the experimental observation by Luckyanova *et al.* is that thermal transport falls into the classical Casimir regime wherein phonons travel ballistically or quasi-ballistically through the interiors of each perovskite layer and scatter diffusely at the interfaces and boundaries.<sup>263</sup> This implies an incoherent thermal transport scheme at the organic–inorganic interfaces, where phonons behave more like particles that scatter randomly off the interfaces and lose their phase information as schematically illustrated in Fig. 10(a). This picture of thermal transport can be quantitatively described by a stacked interfacial thermal conductance model (SITCM) that has been validly applied to self-assembled monolayers<sup>267,304</sup> and nanocrystal arrays<sup>266</sup> with similar organic–inorganic layered structures. An intuitive prediction one can make with this model is that increasing the interlayer distance will lead to a decreased density of interfaces, consequently resulting in a higher effective  $\kappa$  in the cross-plane direction. That is to say, increased  $\kappa$  should be observed in 2D MHPs with larger periodicity, i.e., thicker inorganic layer (larger  $n$  number in the formula) or organic layer (longer-chain spacers). This trend coming from the incoherent interface scattering was observed for structurally similar organic–inorganic hybrid superlattices,<sup>266,305,306</sup> and also all-inorganic layered composites where the acoustic impedance mismatch is smaller.<sup>264,307</sup>

The as-predicted trend was experimentally verified by Dahod *et al.* through systematic research on  $(\text{C}_x\text{H}_{2x+1}\text{NH}_3)_2(\text{MA})_{n-1}\text{Pb}_n\text{Br}_{3n+1}$  using DSC and FDTR.<sup>258</sup> For stoichiometry with  $n$  larger than one, it represents a quasi-2D MHP comprising  $n$  layers of  $[\text{PbBr}_6]^{4-}$  octahedra stacked in the (100) direction, confined by the organic layers. By varying the  $n$  number and the value of  $x$ , the thickness of the inorganic layer and the organic layer can be systematically altered, respectively. In this meticulous work, the 2D MHPs were treated as superlattice-like hybrid materials that fit in the incoherent thermal transport model presented in Fig. 10(a), with phonons treated as particles described by the Boltzmann transport equation with boundary conditions involving diffuse interface scattering.<sup>265</sup> Two key

assumptions underpin this model: (1) the phonon MFP of the bulk material making up the superlattice is comparable or slightly larger than the period thickness so that phonons within individual layers travel ballistically or quasi-ballistically without coherent correlation with adjacent layers and scatter diffusely at the interfaces and (2) each layer is governed by its bulk dispersion relations.<sup>308</sup>

Dahod *et al.* posited similar phonon MFPs in 2D MHPs as in their 3D form,<sup>258</sup> which is comparable to or slightly larger than the periodicity of the alternating layers (1–2 nm),<sup>309,310</sup> ensuring ballistic behavior of phonons inside the inorganic layers. Although counter-intuitive, phonons were also assumed by Dahod *et al.* to be traveling ballistically through the organic layers, despite the intrinsically ultralow  $\kappa$  of alkanes. According to the second assumption, the heat capacity and sound speed within the perovskite octahedra and alkylammonium chain layers are taken to be analogous to those in 3D  $\text{MAPbBr}_3$  and liquid alkanes, respectively. The decoupling of phonon branches between different layers here is a reasonable assumption, given that the vibrational density of states of 2D MHPs resemble the sum of those of the organic and inorganic sub-lattices as implied by low-frequency Raman spectroscopy.<sup>303</sup> The monotonic trend of increasing  $\kappa$  with the thickness of either the organic or the inorganic layer [Fig. 10(b)] is well described by the following equation, originally derived for superlattices:<sup>264</sup>

$$\kappa = \frac{1}{2} \left( \frac{1}{C_1 v_1} + \frac{1}{C_2 v_2} \right)^{-1} \frac{(d_1 + d_2)}{2}, \quad (12)$$

where the subscripts represent different layer components, organic or inorganic,  $C_i$  is the bulk volumetric heat capacity,  $v_i$  is the sound velocity, and  $d_i$  is the layer thickness. Moreover, the measured heat capacities show fair alignment with this model assuming the overall heat capacity to be the mass average between the organic and inorganic subphases [Fig. 10(b)].

More researchers, however, have observed consistent or even decreasing  $\kappa$  of 2D MHPs with an increasing layer thickness, which brought about the existence of a distinct thermal transport mechanism in the cross-plane direction that is dominated by coherent acoustic phonons.<sup>256,257,260</sup> In this picture, as shown in Fig. 11(a), phonons move in a wave-like manner and propagate through layers via collective vibrations of the whole materials, akin to an inorganic superlattice in the  $\kappa$  recovering regime.<sup>263</sup> Phonons of this kind feature MFPs much larger than the periodicity and preserve coherence for up to several layers. The relevant literature reports for this model are discussed below.

### C. Partially coherent cross-plane thermal transport

The existence of coherent longitudinal acoustic phonons (CLAPs) in 2D RP-phase MHPs,  $(\text{BA})_2(\text{MA})_{n-1}\text{Pb}_n\text{I}_{3n+1}$  ( $n=1-6$ ), was first experimentally verified and investigated by P. Guo *et al.* using a pump-probe-based transient reflection technique.<sup>261</sup> An above-bandgap pump was used to excite hot charge carriers, which quickly thermalize through electron–phonon coupling, accompanied by emission of longitudinal optical (LO) phonons.<sup>311</sup> These emitted LO phonons rapidly decay to lower-energy longitudinal acoustic (LA) phonons<sup>312</sup> that propagate coherently in the cross-plane direction. The local strain induced along the propagation of such CLAPs causes depth-dependent modifications on the local material refractive index.

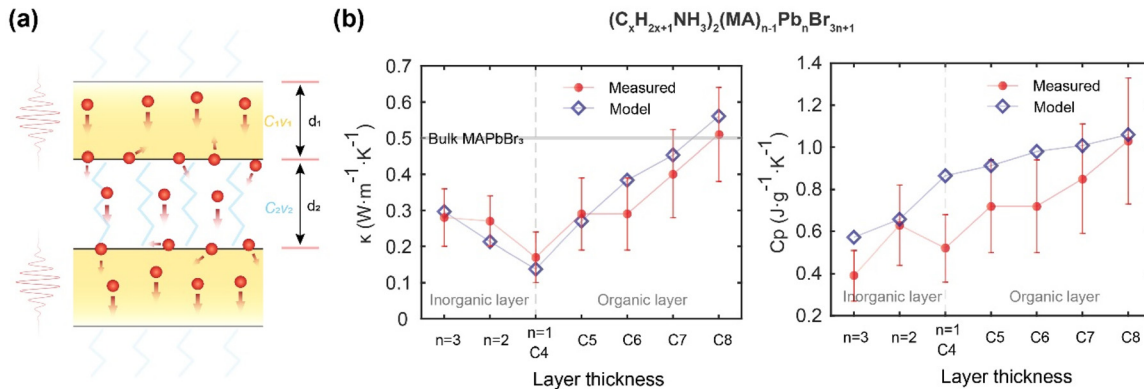


**FIG. 10.** (a) Incoherent thermal transport in the cross-plane direction of 2D hybrid MHPs where short-wavelength particle-like phonons travel ballistically through the interior of individual layers and scatter diffusely at the organic–inorganic interfaces. The cross-plane  $\kappa$  is solely determined by the specific heat ( $C$ ), phonon group velocity ( $v$ ), and layer thickness ( $d$ ) of the organic and inorganic layers. (b) Thermal conductivity (left panel) and heat capacity (right panel) trend of  $(C_xH_{2x+1}NH_3)_2(MA)_{n-1}Pb_nBr_{3n+1}$  with increasing thickness of inorganic ( $n$  value) and organic ( $x$  value) layers. Reproduced with permission from Dahod *et al.*, “Efficient thermal transport across molecular chains in hybrid 2D lead bromide perovskites,” arXiv:2303.17397 (2023). Copyright 2024 Authors, licensed under a Creative Commons Attribution (CC-BY) license.<sup>258</sup>

A below-bandgap (near-infrared) probe light was reflected by the sample and collected by a spectrometer. The interference coming from the spatial-temporal variation in refractive index results in oscillations in the probe intensity over time as shown in Fig. 11(b). Information about the CLAPs such as coherence time and group velocities can then be extracted from these oscillations. Evidently from Fig. 11(b), compounds with smaller  $n$  numbers show stronger coherence and longer lifetimes of CLAPs. Applying a similar technique to another 2D RP-phase MHPs,  $(PEA)_2(MA)_{n-1}Pb_nI_{3n+1}$ , Maity *et al.* further verified the existence of long-lived (extending up to nanoseconds) CLAPs, similar to those present in 3D MHPs, while the lifetime of optical phonons in the system is only on the sub-ps timescale.<sup>313</sup>

Despite featuring reduced group velocities and significant attenuation compared to the 3D counterparts due to the large acoustic impedance mismatch between organic and inorganic layers, the relatively long-lived CLAPs could serve as important heat carriers in cross-plane thermal transport and potentially lead to increased  $\kappa$ . Several studies provide compelling evidence of another more complex thermal transport scheme involving coherent phonon transport across the layer interfaces, contrary to the purely diffuse scattering model discussed in Sec. IV B. In this partially coherent thermal-transport picture, both incoherent interface scattering and coherent wave-like transport of phonons across the interfaces contribute to the overall heat transfer through the layered structures.<sup>265</sup>

While modeling the phonon propagation with a coherent wave equation, the diffuse interface scattering is accounted for by an imaginary part in the propagation wave vector of coherent phonons. This model is well-established to explain the period thickness dependence of  $\kappa$  in superlattices.<sup>265,314</sup> Two anomalous trends in  $\kappa$  of 2D MHPs, contrary to the prediction made by SITCM, are generally observed experimentally in a wide range of research, supporting the notion that a substantial amount of heat is carried by coherent phonons across the interfaces in 2D MHPs.

One observation is the cross-plane  $\kappa$  being nearly independent of the thickness of the organic layer (chain length of the organic

spacers).<sup>38,256,257</sup> A. Giri *et al.* revealed an insignificant influence of spacing distance between the inorganic layers on the  $\kappa$  with TDTR.<sup>38</sup> Furthermore, by increasing the organic chain length in  $(C_nH_{2n+1}NH_3)_2PbI_4$  from  $n=4$  to  $n=7$ , an almost constant, and even decreasing  $\kappa$  was found with the same TDTR technique at 330 K [Fig. 11(c)].<sup>256</sup> This trend is inconsistent with the prediction of the incoherent thermal transport model, i.e., SITCM, and is attributed to phonons propagating coherently across interfaces. The coherence of phonons is expected to be disrupted by larger periodicity, coming from the lengthened organic spacers according to the partially coherent model. A recent work, up to the point of this review, reported an almost twofold decrease in  $\kappa$  (at room temperature) as the organic chain length increases from  $n=4$  to  $n=6$  in  $(C_nH_{2n+1}NH_3)_2PbI_4$ , also measured with TDTR.<sup>259</sup>

Another unexpected trend is the decreasing cross-plane  $\kappa$  with thicker inorganic layers (larger  $n$  number in the general formula).<sup>260</sup> Christodoulides *et al.* used FDTR to investigate the  $\kappa$  dependence on the inorganic layer thickness by measuring  $(BA)_2(MA)_{n-1}Pb_nI_{3n+1}$  with  $n$  increasing from 1 to 4 for thin films and  $n=3-6$  for single crystals. A monotonically decreasing trend of  $\kappa$  with  $n$  was observed [Fig. 11(d)], which contrasts with the results from Dahod *et al.* that assumed totally incoherent thermal transport across interfaces.<sup>258</sup> Both Christodoulides *et al.* and Guo *et al.* applied a simple harmonic bead-spring model [Fig. 11(e)] to capture the coherent nature of these systems and revealed a stronger band-flattening effect in the phonon dispersions for systems with higher  $n$  values.<sup>260,261</sup> Relationship between the phonon dispersion and material  $\kappa$  is given by an equation similar to Eq. (11)<sup>265,315</sup>

$$\kappa_i = \sum_{\lambda} C_{ph}(\omega_{\lambda}) \cdot \left| \frac{\partial \omega}{\partial k_i} \right| \cdot MFP_{SL}, \quad (13)$$

where  $i$  specifies the direction of thermal transport,  $\lambda$  denotes the phonon mode,  $C_{ph}(\omega_{\lambda})$  stands for the mode specific heat,  $\omega$  is the angular frequency, and  $k$  is the wave vector.  $MFP_{SL}$  represents the total phonon mean-free path in the superlattice-like structure as defined elsewhere.<sup>265</sup>

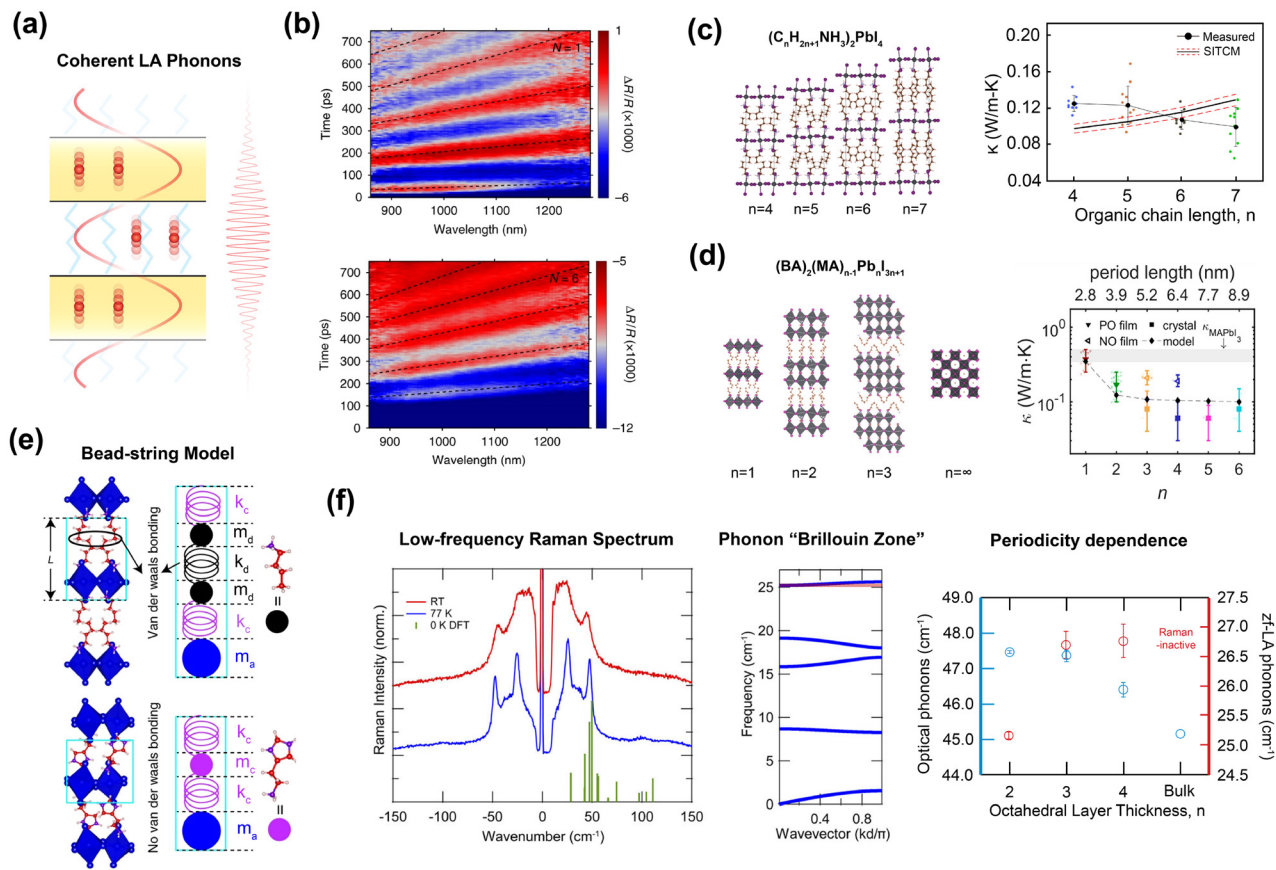


**FIG. 11.** (a) Coherent thermal transport in the cross-plane direction of 2D hybrid MHPs where coherent LA phonons with MFPs spanning several layers behave wave-like and travel coherently across layers with minimal or no interface scattering. (b) Transient reflection ( $\Delta R/R$ ) spectral maps for  $(BA)_2(MA)_{N-1}Pb_{N-3}I_{3N+1}$  with  $N=1$  (upper panel) and  $N=6$  (lower panel) showing oscillations that indicate the presence of coherent longitudinal acoustic phonons (CLAPs). Reproduced with permission from Guo *et al.*, Nat. Commun. **9**, 2019 (2018). Copyright 2018 Authors, licensed under a Creative Commons Attribution (CC-BY) license.<sup>261</sup> (c) Decreasing thermal conductivity of RP-phase 2D MHPs with increasing thickness of organic layers, i.e., number of carbons in the alkylammonium chain length from  $n=4$  to 7, measured with TDTR (indicated by the scatters), and an opposite trend predicted by the stacked interface model (solid and dashed lines). Reproduced with permission from Rasel *et al.*, ACS Appl. Mater. Interfaces **12**(48), 53705–53711 (2020). Copyright 2020 American Chemical Society.<sup>256</sup> (d) Decreasing thermal conductivity of RP-phase 2D MHPs with increasing thickness of inorganic layers measured with FDTR on single crystals and films, and calculated with a harmonic bead-string model. Reproduced with permission from Christodoulides *et al.*, ACS Nano **15**(3), 4165–4172 (2021). Copyright 2021 American Chemical Society.<sup>260</sup> (e) A harmonic bead-string model for the cross-plane thermal transport of 2D hybrid MHPs with monovalent spacer cations (upper panel) and divalent spacer cations (lower panel). Reproduced with permission from Guo *et al.*, Nat. Commun. **9**, 2019 (2018). Copyright 2018 Authors, licensed under a Creative Commons Attribution (CC-BY) license.<sup>261</sup> (f) Left panel: low-frequency Raman spectra of  $n=2$   $(BA)_2MAPb_2I_7$ , measured at room temperature (red) and 77 K (blue), and calculated at 0 K with DFT (green). The sharp peaks at  $47.5$  and  $25.2\text{ cm}^{-1}$  correspond to the inorganic cage distortion and zone-fold longitudinal acoustic (zf-LA) phonon mode, respectively. Middle panel: calculated phonon "Brillouin zone" dispersion (blue) and experimentally measured zf-LA phonon mode frequency (red). Right panel: periodicity dependence of the optical (blue) and zf-LA (red) phonon energy, measured with increasing inorganic layer thickness from  $n=2$  to 4 and for bulk  $MAPbI_3$ . Reproduced with permission from Dahod *et al.*, J. Chem. Phys. **153**(4), 044710 (2020), of AIP Publishing.

The simulated band flattening is considered to reduce the group velocities,  $\left|\frac{\partial\omega}{\partial k_i}\right|$ , of CLAPs, accounting for the  $\kappa$  diminishment in high- $n$  samples. More intriguingly, a universal coherent phonon lifetime across  $n=1$ –6 is extracted to be  $\sim 100$  ps, which corresponds to phonon MFPs of 7 nm for  $n=6$  and 12 nm for  $n=1$  in the cross-plane direction. The much larger MFPs than the interlayer spacing<sup>309</sup> further highlight the wave-like properties of phonons in RP-phase 2D MHPs. The decreasing trend of MFPs, along with slowed group velocities as the thickness of the inorganic layer increases, demonstrates the reduction in  $\kappa$  dictated by Eq. (13).

In addition to the direct measurements of  $\kappa$ , Raman spectroscopy serves as another powerful technique to provide insights into the partially coherent thermal transport nature in 2D MHPs.<sup>303,316</sup> Similar to their 3D counterparts, 2D MHPs exhibit low-frequency (between 30 and  $100\text{ cm}^{-1}$ ) LO and transverse optical (TO) modes, corresponding to octahedral twists and distortions coupled to the organic cations, shown as a sharp Raman mode at  $47.5 \pm 0.1\text{ cm}^{-1}$  for an  $n=2$   $(BA)_2(MA)Pb_2I_7$  in Fig. 11(f). Additionally, ultra-low-frequency modes have been identified by Raman spectroscopy below this region ( $< 30\text{ cm}^{-1}$ ) and are attributed to zone-folded longitudinal acoustic (zf-LA) phonons resulting from the superlattice-like layered structure

of 2D MHPs.<sup>303,316</sup> The periodically varying elastic properties in the cross-plane direction lead to a periodic environment resembling the periodic potential wells experienced by electrons in crystals. Consequently, a phonon “Brillouin zone” is formed in the dispersion of phonons propagating along the direction of this discrete periodicity as illustrated in the calculated phonon dispersion diagram in Fig. 11(f). The LA phonon branches extending out of the first Brillouin zone can then be zone-folded back to the first zone. Such zone-folding behavior is widely observed and well-studied in superlattices.<sup>314,315,317,318</sup>

Evident in the calculated dispersions in Fig. 11(f), two anomalous phonon properties arise from this phonon Brillouin zone picture. One is the presence of Raman-active LA modes with non-zero frequency at the zone center. The second is the emergence of phonon bandgaps (only for the longitudinal modes) in the dispersion for phonon wavelengths satisfying the Bragg condition. These properties of LA phonons are widely observed in inorganic superlattices sharing a similar, layered structure.<sup>317–319</sup> Note that only the low-lying LA phonon branches experience the zone-folding effect, because LA phonons with high frequencies corresponding to wavelengths shorter than the period thickness will behave more particle-like and scatter off the interfaces instead of transmitting coherently and forming the phonon Brillouin zone. Furthermore, higher  $n$ -value 2D MHPs with thicker inorganic layers (larger periodicity) were verified to also support the zf-LA mode, featuring a qualitatively similar Raman spectrum to the  $n = 1$  MHP in the  $n = 2$  sample.<sup>303</sup> Notably, from the  $n$ -number-dependent phonon dispersion relation in Fig. 11(f), the optical phonon modes originating from the inorganic cage distortion redshift toward the bulk value in 3D MHPs, and the zf-LA phonon branches shift upward. It can thus be well anticipated that at higher  $n$  values, the softened optical modes and hardened acoustic modes begin to overlap, leading to more prominent phonon scattering, thereby a lower  $\kappa$ . Also, at a high enough  $n$  value, i.e., large enough periodicity, the LA modes will no longer be observable in Raman as the periodicity becomes larger than the wavelength of the LA phonons. These arguments from Raman spectroscopic measurement align well with the thermal transport measurements discussed above.

#### D. Measuring anisotropic thermal transport

All the above-discussed thermal transport and Raman characterizations revealed a partially coherent nature of thermal transport in the cross-plane direction of 2D MHPs. Along the in-plane direction, where phonons propagate within each constituent layer, 2D MHPs are expected to exhibit higher  $\kappa$ , akin to other layered structures.<sup>320–323</sup> However, the in-plane thermal transport has been less investigated than cross-plane transport due to the inherent low sensitivity of TDTR and FDTR to in-plane thermal transport (i.e., caused by heat spreading in the metallic transducers), as well as a stringent requirement on the surface smoothness.<sup>88,89</sup> Measuring the in-plane  $\kappa$  of layered materials, especially single crystals, remains a challenging topic.

Alternatively, measurements can be conducted on polycrystalline films of 2D MHPs, where the orientation of the layers relative to the substrate can be meticulously controlled through various deposition techniques.<sup>324</sup> While spin-coated films generally favor a horizontal orientation—where the layers are parallel to the substrate, a vertical orientation with layers perpendicular to the substrate is sometimes more desirable because of the significantly better electrical conductivity and carrier mobility along the planes. TDTR and FDTR have been

successfully applied to measure the in-plane  $\kappa$  of 2D MHPs on vertically oriented films.<sup>38,260</sup> Nonetheless, the high density of grain boundaries and defects in films considerably impede thermal transport, leading to challenges in accurately extracting the intrinsic anisotropic thermal properties of these materials.

Despite these challenges, methods other than TDTR or FDTR, such as LFA, TTG, and SThM, as introduced in Sec. II have been utilized to measure the anisotropic thermal transport properties of 2D MHPs.<sup>123,125,255,325</sup> The exceptional directional sensitivity of TTGs allows for the detection of lateral thermal transport near the surface.<sup>126</sup> The in-plane thermal conductivity ( $\kappa_{\parallel}$ ) of  $(BA)_2PbI_4$  single crystals was measured with TTG to be  $0.28 \pm 0.01 \text{ W}\cdot\text{m}^{-1}\cdot\text{K}^{-1}$  at 300 K, aligning well with MD simulation predictions.<sup>123</sup> Given that the cross-plane thermal conductivity ( $\kappa_{\perp}$ ) predicted by the same MD simulation is  $0.18 \pm 0.01 \text{ W}\cdot\text{m}^{-1}\cdot\text{K}^{-1}$ , it was concluded that  $(BA)_2PbI_4$  exhibits a relatively low anisotropy ( $\kappa_{\parallel}/\kappa_{\perp} \sim 1.5$ ) compared to van der Waals layered materials that exhibit tens or hundreds of anisotropic ratio.<sup>320,321,323,326</sup> In another work, simultaneous measurement of  $\kappa_{\parallel}$  and  $\kappa_{\perp}$  was achieved with cross-sectional SThM on a film of  $(PEA)_2PbI_4$ , and lower-than-expected anisotropy ( $\kappa_{\parallel}/\kappa_{\perp} \sim 3.4$ ) was also found.<sup>325</sup> This minimal anisotropy in 2D MHPs may be contributed by the CLAPs that are carrying substantial heat across the layer interfaces. Using DynaCool physical property measurement system (PPMS), which is based on steady-state methods, Mandal *et al.* measured the anisotropic thermal conductivity of a lead-free RP-phase 2D double perovskite,  $(PA)_4CuInCl_8$  ( $PA = C_3H_7NH_3^+$ ), to be 0.15 and  $0.28 \text{ W}\cdot\text{m}^{-1}\cdot\text{K}^{-1}$  in the cross-plane and in-plane directions, respectively.<sup>242</sup> The measurement was conducted on highly oriented powder-compressed pellets, enabling the use of commercial instrument.

Beyond organic-inorganic hybrid 2D MHPs, the thermal transport properties of all-inorganic 2D MHPs are also of great research interest. Acharyya *et al.* employed a commercial LFA instrument to measure both  $\kappa_{\perp}$  and  $\kappa_{\parallel}$  of high-quality, Bridgman-grown all-inorganic 2D  $Cs_2PbI_2Cl_2$  and  $Cs_3Bi_2I_6Cl_3$  single crystals.<sup>255,327</sup> As anticipated, all-inorganic 2D MHPs show higher  $\kappa$  in both in-plane and cross-plane directions compared to organic-inorganic hybrid 2D MHPs. In addition, the absence of organic-inorganic interfaces, which introduce strong diffuse scattering of phonons particularly in the cross-plane direction, together with the weak interlayer interaction, results in a remarkably low thermal transport anisotropy of  $\kappa_{\parallel}/\kappa_{\perp} \sim 1.1$  in  $Cs_2PbI_2Cl_2$ . The  $\kappa$  of single crystalline and polycrystalline 2D MHPs measured with different techniques in either in-plane or cross-plane directions are summarized in Table III and Fig. 12.

It is noteworthy that while LFA experiments based on well-established commercial instruments offer a straightforward and fast-handed approach to measuring the thermal transport properties, the stringent requirement on the quality and size of the sample largely limits its applicability. Typical LFA instruments require the samples to be millimeters in both size and thickness,<sup>48,50</sup> which is nontrivial to meet for hybrid 2D MHPs.<sup>292,328</sup> Therefore, LFA is predominantly applied on powder-compressed pellets, which only reflects an effective isotropic  $\kappa_{\text{eff}}$ . The circular markers in Fig. 12 represent the effective  $\kappa_{\text{eff}}$  without any consideration of anisotropy.

#### E. Temperature-dependent thermal transport

At high temperatures (i.e., temperatures above the Debye temperature),  $\kappa$  of semiconducting or insulating solids generally goes as an

**TABLE III.** Summary of heat capacities and thermal conductivities of quasi-2D and lower dimensional (1D and 0D) MHPs.

Material	Form	Heat capacity ( $J \cdot g^{-1} \cdot K^{-1}$ )	$\kappa_{\perp}$ ( $W \cdot m^{-1} \cdot K^{-1}$ )	$\kappa_{\parallel}$ ( $W \cdot m^{-1} \cdot K^{-1}$ )	Method	Reference
(BA) <sub>2</sub> PbI <sub>4</sub>	Film	0.439	0.18 ± 0.04		TDTR	38
	Film		0.37 ± 0.13/0.12		FDTR	260
	Film		0.204 ± 0.009		TDTR	259
	SC	0.546	0.125 ± 0.009 (330 K)		TDTR	256
	SC	0.48		0.28 ± 0.01	TTG	123
	SC		0.18 ± 0.01	0.27 ± 0.01	MD	123
	Powder	0.41 (200 K)	0.149 (300 K)–0.155 (385 K)		LFA	43
		0.55 (300 K)				
		0.63 (450 K)				
	SC		0.158	0.289	MD	262
<sup>a</sup> (PeA) <sub>2</sub> PbI <sub>4</sub>	SC	0.697	0.123 ± 0.021 (330 K)		TDTR	256
<sup>a</sup> (HexA) <sub>2</sub> PbI <sub>4</sub>	SC	0.675	0.107 ± 0.011 (330 K)		TDTR	256
<sup>a</sup> (HepA) <sub>2</sub> PbI <sub>4</sub>	Film		0.105 ± 0.007		TDTR	259
	SC	0.879	0.099 ± 0.021 (330 K)		TDTR	256
	Film	0.437	0.10 ± 0.02		TDTR	38
(isoBA) <sub>2</sub> PbBr <sub>4</sub>	Film	0.576	0.11 ± 0.02		TDTR	38
(BA) <sub>2</sub> (MA)Pb <sub>2</sub> I <sub>7</sub>	Film		0.17 ± 0.08/0.07		FDTR	260
	SC		0.182	0.292	MD	262
	Film		0.08 ± 0.06/0.04	0.21 ± 0.05/0.04	FDTR	260
	SC		0.192	0.299	MD	262
	SC			0.17 ± 0.03	TDTR	38
(BA) <sub>2</sub> (MA) <sub>3</sub> Pb <sub>4</sub> I <sub>13</sub>	Film		0.11 ± 0.02		TDTR	38
	Film			0.19 ± 0.04/0.03	FDTR	260
	Film				FDTR	260
	SC		0.06 ± 0.04/0.03		FDTR	260
	SC		0.215	0.309	MD	262
(BA) <sub>2</sub> (MA) <sub>4</sub> Pb <sub>5</sub> I <sub>16</sub>	SC		0.06 ± 0.03		FDTR	260
(BA) <sub>2</sub> (MA) <sub>5</sub> Pb <sub>6</sub> I <sub>19</sub>	SC		0.08 ± 0.07/0.04		FDTR	260
(PEA) <sub>2</sub> PbI <sub>4</sub>	Film	0.467	0.15 ± 0.03		TDTR	38
	Film		0.19 ± 0.03		TDTR	257
	Film		0.13 ± 0.05	0.45 ± 0.05	SThM	325
	Film		0.100 ± 0.005		TDTR	259
	SC		0.38		MD	257
	Powder	0.38 (200 K)	0.135 (300–385 K)		LFA	43
		0.50 (300 K)				
		0.80 (450 K)				
<sup>a</sup> (PEA)(PA)PbI <sub>4</sub>	Film		0.185 ± 0.014		TDTR	259
(PEA)(BA)PbI <sub>4</sub>	Film		0.145 ± 0.005		TDTR	259
(PEA) <sub>2</sub> PbBr <sub>4</sub>	Film	0.535	0.13 ± 0.03		TDTR	38
(BA) <sub>2</sub> PbBr <sub>4</sub>	Film	0.578	0.19 ± 0.04		TDTR	38
(BA) <sub>2</sub> PbBr <sub>4</sub>	SC	0.52 ± 0.16	0.19 ± 0.07		FDTR	258
	SC	0.72 ± 0.22	0.29 ± 0.1		FDTR	258
(HexA) <sub>2</sub> PbBr <sub>4</sub>	SC	0.72 ± 0.22	0.29 ± 0.1		FDTR	258
(HepA) <sub>2</sub> PbBr <sub>4</sub>	SC	0.85 ± 0.26	0.40 ± 0.12		FDTR	258
<sup>a</sup> (OA) <sub>2</sub> PbBr <sub>4</sub>	SC	1.03 ± 0.3	0.51 ± 0.13		FDTR	258
(BA) <sub>2</sub> (MA)Pb <sub>2</sub> Br <sub>7</sub>	SC	0.63 ± 0.19	0.27 ± 0.07		FDTR	258
(BA) <sub>2</sub> (MA) <sub>2</sub> Pb <sub>3</sub> Br <sub>10</sub>	SC	0.39 ± 0.12	0.28 ± 0.08		FDTR	258
<sup>a</sup> (S-MePEA)(PA)PbI <sub>4</sub>	Film		0.106 ± 0.005		TDTR	259
(S-MePEA)(BA)PbI <sub>4</sub>	Film		0.105 ± 0.008		TDTR	259

TABLE III. (Continued.)

Material	Form	Heat capacity ( $\text{J}\cdot\text{g}^{-1}\cdot\text{K}^{-1}$ )	$\kappa_{\perp}$ ( $\text{W}\cdot\text{m}^{-1}\cdot\text{K}^{-1}$ )	$\kappa_{\parallel}$ ( $\text{W}\cdot\text{m}^{-1}\cdot\text{K}^{-1}$ )	Method	Reference
(S-MePEA)(HexA) $\text{PbI}_4$	Film		$0.118 \pm 0.0075$		TDTR	259
(S-MePEA)(OA) $\text{PbI}_4$	Film		$0.098 \pm 0.0055$		TDTR	259
(S-MePEA)(PEA) $\text{PbI}_4$	Film		$0.109 \pm 0.008$		TDTR	259
(S-MePEA) $_2\text{PbI}_4$	Film		$0.134 \pm 0.006$		TDTR	259
<sup>a</sup> (S-MBA) $_2\text{PbI}_4$	Film		$0.139 \pm 0.0055$		TDTR	259
<sup>a</sup> (4AMP) $\text{PbI}_4$	Film		$0.18 \pm 0.03$		TDTR	257
	SC		0.38		MD	257
<sup>a</sup> (4Tm) $_2\text{FASn}_2\text{I}_7$	Film		0.124		$3\omega$	288
	Film		0.146		TDTR	288
<sup>a</sup> (HIST) $\text{PbI}_4$	Powder		$0.16 \pm 0.01$		LFA	295
$\text{CsPb}_2\text{Br}_5$	Film	0.18	$0.33 \pm 0.02$		$3\omega$ -SThM	236
$\text{Cs}_2\text{PbI}_2\text{Cl}_2$	SC		0.37 (300 K)–0.28 (523 K)	0.41 (300 K)–0.3 (532 K)	LFA	255
$\text{Cs}_3\text{Bi}_2\text{I}_6\text{Cl}_3$	SC		0.20	0.22	LFA	327
	SC		0.130	0.227	MD	340
<sup>a</sup> (PA) $_4\text{CuInCl}_8$	Powder		0.15	0.28	PPMS	242
<sup>a</sup> (4N4) $_2\text{CuInCl}_8$	Powder			0.27	PPMS	242
<sup>a</sup> (4N4) $_2\text{CuRuCl}_8$	Powder			0.3	PPMS	242
<sup>a</sup> (IMI) $\text{PbI}_3$ (1D)	Powder		$0.16 \pm 0.01$		LFA	295
$\text{Cs}_4\text{PbCl}_6$ (0D)	Film	$0.15 \pm 0.08$	$0.30 \pm 0.03$		$3\omega$ -SThM	237
$(\text{MA})_3\text{Bi}_2\text{I}_9$ (0D)	Powder	0.34	$0.21$ (300–450 K)		LFA	218
	Powder	0.34	$0.23 \pm 0.02$		LFA	300
$\text{Cs}_3\text{Bi}_2\text{I}_9$ (0D)	Powder		$0.20$ (30–523 K)		LFA	348
$[\text{Mn}(\text{C}_2\text{H}_6\text{OS})_6]\text{I}_4$ (0D)	Powder		$0.15 \pm 0.01$		LFA	350
	Film			0.21 $\pm 0.01$	$3\omega$	350

<sup>a</sup>PA = Propyl ammonium; PeA = Pentyl ammonium; HexA = Hexyl ammonium; HepA = Heptyl ammonium; OA = Octyl ammonium; S-MePEA = (S)-Methyl-phenyl-ethyl-ammonium; S-MBA = (S)-Methyl-benzyl-ammonium; 4Tm = 2-(3'',4'-dimethyl[2,2':5',2'':5'',2''''-quaterthiophen]-5-yl)ethan-1-ammonium; HIST = Histammonium; 4N4 = 1,4-butane diammonium; and IMI = Imidazolium.

inverse relationship with temperature, i.e.,  $\kappa(T) \propto T^{-\alpha}$ , due to strong phonon–phonon scattering.<sup>329</sup> In a crystal where the thermal transport is primarily limited by the lowest-order three-phonon processes (both Umklapp and normal scattering), a linearly inverse dependence is followed, i.e.,  $\alpha = 1$ . Practically, however, thermal transport in typical inorganic bulk PV materials involves higher-order phonon–phonon scatterings (involving more than three phonons), leading to a steeper temperature dependence, i.e.,  $1 < \alpha \leq 2$ .<sup>296,330,331</sup>

A higher value of  $\alpha$ , which stands for a stronger temperature dependence, implies more prominent temperature-dependent phonon scattering. As discussed in the previous section, anisotropic thermal transport arises in 2D MHPs due to the difference in dominating phonon scattering mechanisms in cross-plane and in-plane directions. In the cross-plane direction, the temperature-insensitive interface scattering plays a significant role in affecting the cross-plane  $\kappa$ , whereas in-plane thermal transport is dominated by the more temperature-dependent phonon–phonon scattering. The  $\kappa$  in either in-plane or cross-plane direction is thus expected to exhibit different extents of temperature dependence, with  $\kappa_{\parallel}$  showing stronger temperature dependence than  $\kappa_{\perp}$ .<sup>265</sup> Although this behavior has not been reported experimentally for 2D MHPs to the best of our knowledge, it has been well studied by the same partially coherent model discussed in

Sec. IVB for superlattices. A representative temperature-dependent  $\kappa$  in both in-plane and cross-plane directions of GaAs/AlAs superlattice calculated from this model is shown in Fig. 13(a).

Temperature dependence of  $\kappa$  could shed light onto the underlying complex phonon scattering process of thermal transport in 2D MHPs. However, it is challenging to conduct temperature-varying thermal transport measurements on 2D MHPs, especially on hybrid ones due to phase or structural transitions. For instance,  $(\text{BA})_2\text{PbI}_4$  goes through a structural phase transition featured by the shifting of  $\text{BA}^+$  cations relative to the inorganic layers at 274 K.<sup>43</sup> Such phase transitions lead to abrupt changes in thermal transport properties, such as jumps in  $\kappa$  and divergence in specific heat, thereby obscuring the intrinsic temperature dependence. Therefore, temperature-dependent measurements on 2D MHPs are typically limited to a relatively narrow range, in which case the temperature dependence, i.e., the form of  $T^{-\alpha}$ , is hard to extract.<sup>43,218,255,256</sup>

By measuring the temperature-dependent thermal diffusivity of  $(\text{BA})_2\text{PbI}_4$  and  $(\text{PEA})_2\text{PbI}_4$  pellets with LFA, and the corresponding heat capacity with DSC, R.-I. Biega *et al.* obtained an almost constant  $\kappa$  of  $\sim 0.135 \text{ W}\cdot\text{m}^{-1}\cdot\text{K}^{-1}$  for  $(\text{PEA})_2\text{PbI}_4$  and  $\sim 0.152 \text{ W}\cdot\text{m}^{-1}\cdot\text{K}^{-1}$  for  $(\text{BA})_2\text{PbI}_4$  in a moderate temperature range of 300–385 K as summarized in Fig. 13(b).<sup>43</sup> Although the 3D counterpart, i.e., MAPbI<sub>3</sub>,

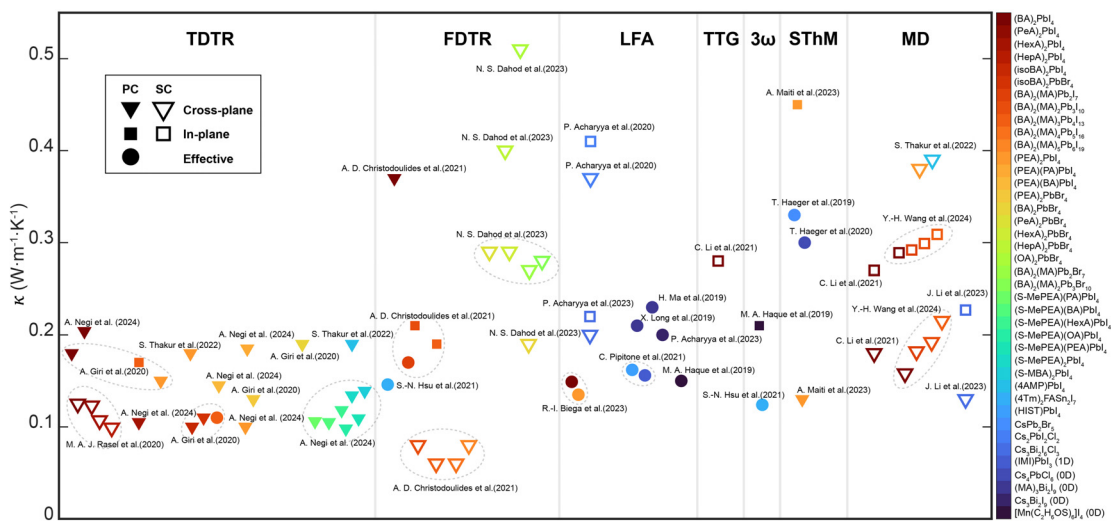


**FIG. 12.** Summary of anisotropic thermal conductivities of quasi-2D and other lower-dimensional MHPs measured (and calculated) with different techniques. The color of the marker indicates the specific material. The triangular and square markers represent the cross-plane and in-plane thermal conductivities, respectively. The effective (circular marker) values come from measurements on randomly oriented polycrystals. The hollowed markers stand for values of single crystals, while the filled markers are for polycrystalline samples, including films, powders, and powder-pressed pellets. A summary of thermal conductivity values, specific heat, and references can be found in Table III.

undergoes a phase transition within this temperature range, 300 K is well above the transition temperature of both (BA)-based and (PEA)-based 2D MHPs. While a clear decreasing trend in the measured thermal diffusivities with increasing temperature was recognized, the corresponding increase in heat capacity compensates for the trend, yielding a nearly invariant  $\kappa_{\text{eff}}$ , as dictated by Eq. (2).

The evaluated  $\kappa_{\text{eff}}$  here are the effective values of the powder-compressed pellets, as opposed to values measured on single crystals or highly oriented films.<sup>38,123,256,260</sup> Moreover, the temperature range applied here is too small to accurately fit any  $T^{-\alpha}$  dependence. In spite of the experimental difficulties, numerical methods such as MD simulations have been successfully applied to calculate the temperature-dependent  $\kappa_{\perp}$  of 2D MHPs in a relatively large temperature range, revealing a remarkably small temperature dependence for hybrid 2D MHPs, with  $\alpha = 0.41$  for DJ-phase (4AMP)PbI<sub>4</sub> and  $\alpha = 0.44$  for RP-phase (PEA)<sub>2</sub>PbI<sub>4</sub><sup>257</sup> as illustrated in Fig. 13(c).

Temperature-dependent thermal transport measurements were also performed on all-inorganic 2D MHPs. Although 3D all-inorganic MHPs suffer severe phase transitions even in ambient conditions,<sup>332</sup> a 2D all-inorganic RP-phase MHP, Cs<sub>2</sub>PbI<sub>2</sub>Cl<sub>2</sub> remains phase transition-free over a large temperature range (100–700 K),<sup>333</sup> making it a promising material to investigate the temperature-dependent thermal transport in 2D MHPs. Both  $\kappa_{\parallel}$  and  $\kappa_{\perp}$  of Cs<sub>2</sub>PbI<sub>2</sub>Cl<sub>2</sub> were measured in the temperature range of 295–523 K with LFA as shown in Fig. 13(d).<sup>255</sup> Temperature-dependent Raman spectra also revealed a decreasing phonon lifetime with increasing temperature, accounting for the decreasing  $\kappa$ . Interestingly,  $\kappa_{\parallel}$  shows a more prominent temperature dependence than  $\kappa_{\perp}$ . This difference is consistent with the prediction made by the partially coherent thermal transport model, which states that cross-plane thermal transport that experiences more temperature-independent interface scattering should have a weaker temperature dependence than in-plane transport. This implies the

potential existence of CLAPs in the all-inorganic 2D MHPs. To this end, a quantitative analysis of the ratio of coherent and incoherent phonons responsible for the cross-plane thermal transport is theoretically possible through measuring the temperature-dependent  $\kappa_{\perp}$  and comparing the extent of discrepancies between the stacked-interface model and partially coherent model.

Another point to note is that Cs<sub>2</sub>PbI<sub>2</sub>Cl<sub>2</sub> intrinsically features higher  $\kappa$  in all temperatures than other hybrid 2D MHPs due to the absence of poorly conductive organic spacers separating the layers. Reduced acoustic impedance mismatch between adjacent layers also facilitates cross-plane thermal transport.<sup>266</sup> Even so, Cs<sub>2</sub>PbI<sub>2</sub>Cl<sub>2</sub> still possesses much lower  $\kappa$  than other inorganic PV materials,<sup>209,298,331,334–337</sup> originating from its layered structure, and strong anharmonic coupling between the acoustic phonons and flat, low-energy optical phonons.<sup>255</sup> At the same time, the layered structure leads to a very low temperature dependence of  $\kappa_{\perp}(T) \propto T^{-\alpha}$  with  $\alpha$  much lower than other inorganic PV semiconductors, approaching the inorganic superlattices.<sup>93,338,339</sup>

An anomalous glass-like temperature dependence,  $\alpha < 0$ , was found in a (111)-oriented all-inorganic 2D MHP, Cs<sub>3</sub>Bi<sub>2</sub>I<sub>6</sub>Cl<sub>3</sub> by Acharyya *et al.*<sup>327</sup> The  $\kappa$  below room temperature down to 2 K was measured using a physical properties measurement system (DynaCool PPMS), and thermal diffusivity from 300 to 400 K was measured by LFA to obtain the  $\kappa$  above room temperature. As shown in Fig. 13(e), three counterintuitive features can be observed: (1) a deviation from the  $T^3$  dependence at low temperature (below the Debye temperature); (2) the absence of a peak in  $\kappa$  as present in general crystalline materials; and (3) a plateau in  $\kappa$  followed by a glass-like increase approaching the glass limit. The unexpected presence of these glass-like behaviors in single crystalline MHPs is attributed to low-frequency acoustic phonons and strong anharmonicity in the crystals.<sup>327,340</sup>

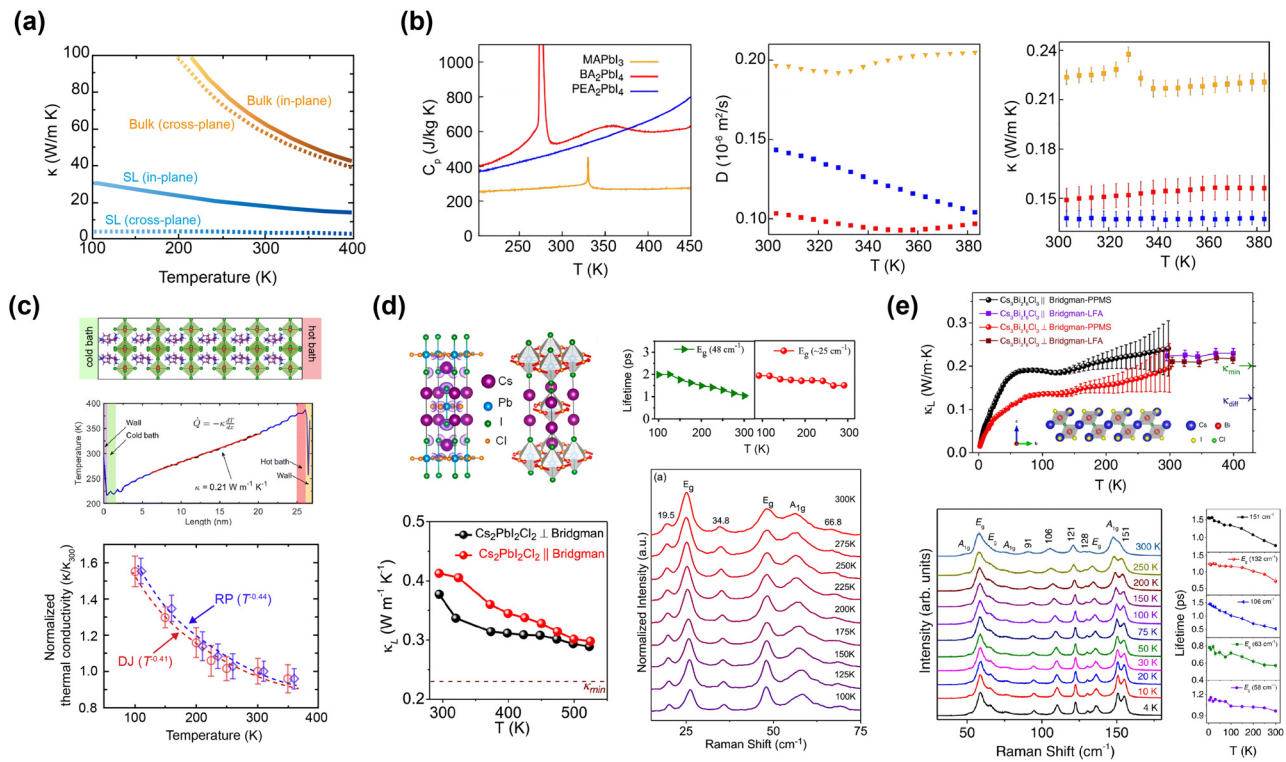


**FIG. 13.** (a) Temperature-dependent thermal conductivity of a typical superlattice, GaAs/AlAs, calculated with the partially coherent model and effective bulk values based on Fourier's law as  $\kappa_{\text{bulk,in-plane}} = (\kappa_1 + \kappa_2)/2$ , and  $\kappa_{\text{bulk,cross-plane}} = 2\kappa_1\kappa_2/(\kappa_1 + \kappa_2)$ . Reproduced with permission from Yang and Chen, Phys. Rev. B **67**, 195311 (2003). Copyright 2003 American Physical Society.<sup>265</sup> (b) Measured heat capacity, thermal diffusivity, and determined thermal conductivity of 3D MAPbI<sub>3</sub> (yellow), 2D (BA)<sub>2</sub>PbI<sub>4</sub> (red) and (PEA)<sub>2</sub>PbI<sub>4</sub> (blue) from 300 to 385 K. Reproduced with permission from Biega *et al.*, J. Phys. Chem. C **127**(19), 9183–9195 (2023). Copyright 2023 American Chemical Society.<sup>43</sup> (c) Upper panel: schematic of MD simulation domain for DJ-phase 2D MHPs. Middle panel: thermal conductivity calculation from the temperature gradient across the domain when subjected to a cross-plane heat flux invoking Fourier's law. Lower panel: predicted temperature-dependent thermal conductivities of DJ-phase (4AMP)PbI<sub>4</sub> and RP-phase (PEA)<sub>2</sub>PbI<sub>4</sub> from 100 to 350 K (normalized by the thermal conductivity of DJ phase at 300 K). Temperature dependence ( $T^{-\alpha}$ ) of  $\alpha = 0.41$  and 0.44 is extracted from the fitted curves for DJ and RP phase, respectively. Reproduced with permission from Thakur *et al.*, Mater. Horiz. **9**, 3087–3094 (2022). Copyright 2022 Royal Society of Chemistry.<sup>257</sup> (d) Crystal structure (upper left), temperature-dependent lattice thermal conductivity along the in-plane (||) and cross-plane direction (⊥) (lower left), and temperature-dependent Raman spectra (lower right) of all-inorganic 2D RP-phase Cs<sub>2</sub>PbI<sub>2</sub>Cl<sub>2</sub> showing decreasing lifetimes of the two E<sub>g</sub> phonon modes with increasing temperature (upper right). Reproduced with permission from Li *et al.*, J. Am. Chem. Soc. **140**(35), 11085–11090 (2018). Copyright 2018 American Chemical Society.<sup>333</sup> (e) Upper panel: temperature-dependent lattice thermal conductivity of (111)-oriented all-inorganic 2D MHP, Cs<sub>3</sub>Bi<sub>2</sub>I<sub>9</sub>, along in-plane (||) and cross-plane (⊥) directions measured with DynaCool physical property measurement system (PPMS) in 2–300 K and with LFA in 300–400 K. The inset shows one slice of the layered crystal structure. Lower panel: temperature-dependent Raman spectra and temperature variation of phonon lifetimes for the modes at 151 cm<sup>-1</sup> (black), 132 cm<sup>-1</sup> (red), 106 cm<sup>-1</sup> (blue), 63 cm<sup>-1</sup> (green), and 58 cm<sup>-1</sup> (purple). Reproduced with permission from Acharyya *et al.*, Nat. Commun. **13**(1), 5053 (2022). Copyright 2022 Authors, licensed under a Creative Commons Attribution (CC-BY) license.<sup>327</sup>

## F. Lower dimensionality

Lower-dimensional MHPs have been integrated into PV devices to achieve enhanced performance.<sup>276,341–344</sup> Furthermore, reducing the dimensionality of MHPs from 2D to 1D and 0D brings up different thermal properties. A decreasing  $\kappa$  is observed using SThM for all-inorganic MHPs as the dimensionality is reduced from 3D CsPbCl<sub>3</sub> (0.49 W·m<sup>-1</sup>·K<sup>-1</sup>) to 2D CsPb<sub>2</sub>Cl<sub>5</sub> (0.40 W·m<sup>-1</sup>·K<sup>-1</sup>) and further to 0D Cs<sub>3</sub>PbCl<sub>6</sub> (0.3 W·m<sup>-1</sup>·K<sup>-1</sup>) [Fig. 14(a)].<sup>36,237</sup> A 1D MHP, namely, imidazolium lead iodide, (IMI)PbI<sub>3</sub>, comprised of face-sharing octahedra chains was measured by LFA.<sup>295</sup> The porosity of the powder-compressed pellets necessitated by LFA was shown to influence the value of the measured  $\kappa$ , as evidenced by subsequent measurements in He and Ar atmosphere. After accounting for the dependence of  $\kappa$  on

the porosity, effective “bulk” values of  $\kappa$  were extrapolated to be 0.16 W·m<sup>-1</sup>·K<sup>-1</sup> that is almost constant in a temperature range of 300–500 K.

The low-toxicity and air-stable 0D Cs<sub>3</sub>Bi<sub>2</sub>I<sub>9</sub>, which contains discrete face-sharing octahedral dimers [Bi<sub>2</sub>I<sub>9</sub>]<sup>3-</sup> [Fig. 14(b)],<sup>345</sup> are gaining substantial interests for PV and photoelectric applications due to its excellent charge-transport properties despite the low dimensionality.<sup>346,347</sup> As shown in Fig. 14(b), a nearly temperature-independent low lattice  $\kappa$  of Cs<sub>3</sub>Bi<sub>2</sub>I<sub>9</sub> was measured to be  $\sim 0.20$  W·m<sup>-1</sup>·K<sup>-1</sup> within 30–523 K by LFA.<sup>348</sup> At the lower temperature limit (<30 K), the  $\kappa$  is well-described by the Debye–Callaway model, with a peak (2.8 W·m<sup>-1</sup>·K<sup>-1</sup>) at 3 K. Notably, the  $\kappa$  at high temperature is approaching the diffusive  $\kappa$  limit (0.13 W·m<sup>-1</sup>·K<sup>-1</sup>) as indicated by

the dashed line in Fig. 14(b). This value ranks among the lowest  $\kappa$  for all-inorganic PV materials.<sup>300</sup> Temperature-dependent Raman spectra and DFT calculation revealed that this ultralow  $\kappa$  originates from (1) the soft crystal structure induced by the extended filled antibonding states near the Fermi level by Bi (6s)-I (5p) orbitals; (2) the strong anharmonicity due to the bi-octahedral rotational and torsional modes; and (3) the strong coupling between the optical phonons associated with the  $\text{Cs}^+$  motion and the transverse acoustic phonon modes.

A similar lead-free 0D MHP,  $(\text{MA})_3\text{Bi}_2\text{I}_9$ , has also been recognized as a potential candidate PV material. Due to its low toxicity and high stability, it has been adopted as the absorbing layer in replacement of or integrated with  $\text{MAPbI}_3$ .<sup>342,349</sup> An analogously low  $\kappa$  of  $\sim 0.2 \text{ W}\cdot\text{m}^{-1}\cdot\text{K}^{-1}$  insensitive to temperature change from 300 to 450 K was measured by LFA (Fig. 14(c)).<sup>218,300</sup> Similar to the isostructural  $\text{Cs}_3\text{Bi}_2\text{I}_9$ , the soft phonon dispersion, strong optical-acoustic phonon coupling and thus short phonon lifetimes, and weak chemical bonds all contribute to the poor thermal conduction in  $(\text{MA})_3\text{Bi}_2\text{I}_9$ .

Another type of lead-free 0D MHP,  $[\text{Mn}(\text{C}_2\text{H}_6\text{OS})_6]\text{I}_4^-$  with a more preferable bandgap (1.6 eV) than both  $\text{Cs}_3\text{Bi}_2\text{I}_9$  and  $(\text{MA})_3\text{Bi}_2\text{I}_9$  ( $\sim 2$  eV) for PV uses, is also found to exhibit a substantially low  $\kappa$  of  $0.15 \pm 0.01 \text{ W}\cdot\text{m}^{-1}\cdot\text{K}^{-1}$  from 300 to 375 K.<sup>350</sup> Moreover, the extending ligands on each individual  $[\text{MnO}_6]^{8-}$  octahedra interact to form a 3D supramolecular network through hydrogen bonding, resulting in effectively anisotropic thermal transport. By employing  $3\omega$  method on a highly oriented film, the in-plane  $\kappa_{||}$  was consequently measured to be  $0.21 \pm 0.01 \text{ W}\cdot\text{m}^{-1}\cdot\text{K}^{-1}$  at room temperature and rapidly decrease to  $\sim 0.08 \text{ W}\cdot\text{m}^{-1}\cdot\text{K}^{-1}$  at 345 K.

## V. COMPOSITIONAL ORIGINS OF THE ULTRALOW THERMAL CONDUCTIVITIES OF MHPs

In general, the MHPs families, from 3D to 0D, exhibit significantly low thermal conductivities. Despite the difference in their crystal structures, dimensionalities, and compositions, similar phonon behaviors are common among them that contribute to their poor thermal conductive properties. While 3D MHPs feature a general formula of

$\text{AB}_3$ , quasi-2D perovskites have a more complex composition,  $\text{A}'_2\text{A}_{n-1}\text{B}_n\text{X}_{3n+1}$ .

To provide guidance on thermal-property tailoring by chemical engineering, in this section, we will present a general view of how the thermal transport properties of MHPs are related to their constituents. From Sec. III C, we discussed the dominating role of  $[\text{BX}_6]^{4-}$  octahedral cages in influencing the thermal conductivities of 3D MHPs. Although by switching the A-site cations from organic to inorganic ones (e.g., from  $\text{MAPbI}_3$  to  $\text{CsPbI}_3$ ), slightly higher thermal conductivity can be obtained, the values still lie within a low region. This behavior is not unique to 3D MHPs but a common trend found also in 2D MHPs. The low anisotropic ratio ( $\kappa_{||}/\kappa_{\perp}$ ) of quasi-2D MHPs compared with other layered materials, as discussed in Sec. IV D, can be partially attributed to this feature. While thermal transport along the in-plane direction usually features a much faster rate than that in cross-plane direction, the heat flow within the inorganic layer in 2D MHPs is still greatly hindered by the intrinsically poor thermal conductance of the octahedral network. Understanding the contributions of  $[\text{BX}_6]^{4-}$  octahedra and also the A-site (or A'-site) cation in the system will help provide more insights to chemists in engineering the thermal transport properties.

### A. Role of A-site cation and $[\text{BX}_6]^{4-}$ octahedra

The correlation between heat transfer and phonon behavior is important for understanding the low  $\kappa$  of MHPs. Materials' phonon dispersion can be determined through inelastic scattering experiments or first-principle calculations to provide more wholistic information for understanding the roles of each constituent in thermal transport.

As discussed in Sec. III C, a decreasing trend in  $\kappa$  is observed when heavier halides ( $X^-$ ) is included, i.e.,  $\kappa_{\text{Cl}} > \kappa_{\text{Br}} > \kappa_{\text{I}}$ . Such a trend can be well explained from the perspective of phonon behaviors. Ferreira *et al.* conducted coherent inelastic neutron scattering spectroscopy and Brillouin light scattering to investigate the low-frequency acoustic phonons in several MHPs.<sup>351</sup> The speed of longitudinal acoustic (LA) and transverse acoustic (TA) phonons in different MHPs can be fitted from the slope of the acoustic phonon dispersion [Figs. 15(a)

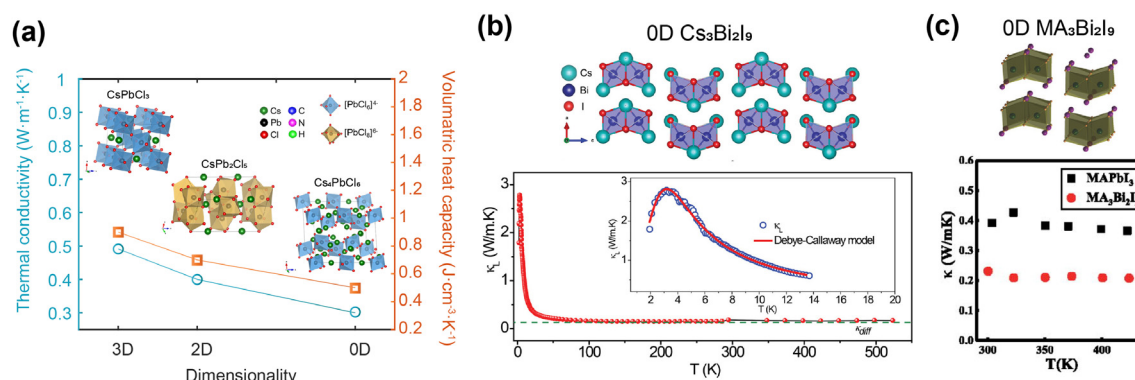


**FIG. 14.** (a) Crystal structures<sup>447</sup> and dimensionality-dependent thermal conductivities<sup>36</sup> of 3D  $\text{CsPbCl}_3$ , 2D  $\text{CsPb}_2\text{Cl}_5$ , and 0D  $\text{Cs}_4\text{PbCl}_6$ . Reproduced with permission from ACS Mater. Lett. **4**, 1255–1263 (2022). Copyright 2022 American Chemical Society. Reproduced with permission from J. Mater. Chem. C **8**, 14289–14311 (2020). Copyright 2020 Royal Society of Chemistry. (b) Crystal structure and thermal conductivity of 0D  $\text{Cs}_3\text{Bi}_2\text{I}_9$  as a function of temperature in 2 to 532 K measured by LFA. Reproduced with permission from Adv. Funct. Mater. **33**, 2304607 (2023). Copyright 2023 John Wiley and Sons.<sup>348</sup> (c) Crystal structure<sup>342</sup> and thermal conductivity of 0D  $\text{MA}_3\text{Bi}_2\text{I}_9$  as a function of temperature from 300 to 450 K measured by LFA.<sup>218</sup> Reproduced with permission from Adv. Energy Mater. **8**, 1703620 (2018). Copyright 2018 John Wiley and Sons. Reproduced from Appl. Phys. Lett. **115**, 072104 (2019), with the permission of AIP Publishing.

and 15(b)]. With the experimentally fitted phonon group velocities, a complete set of elastic constants such as  $C_{11}$ ,  $C_{44}$ ,  $C_{12}$  and the bulk modulus were further deduced as listed in Fig. 15(c). Their significant finding was that among these elastic constants,  $C_{44}$  is extremely small, which is likely related to the rotation and tilting of the Pb-X octahedra.<sup>352</sup> This finding revealed the dominating role of  $[BX_6]^{4-}$  phonon modes in regulating the thermal transport.

Using inelastic neutron scattering, B. Li *et al.* investigated the atomic dynamics in MAPbI<sub>3</sub> and revealed that the dynamics of A-site MA<sup>+</sup> primarily influences the optical phonon properties of the material.<sup>353</sup> Specifically, they distinguished the jumping rotational modes of MA<sup>+</sup> in the orthorhombic phase, as well as an optical phonon mode related to the orientational disorder of MA<sup>+</sup>, which appears after the orthorhombic-to-tetragonal phase transition. The emergence of this orientational disorder reduces the relaxation time of the jumping mode by an order of magnitude. While the contribution of optical phonons to heat transfer is generally considered to be minimal—given their sub-picosecond lifetime and nearly zero group velocity—in the case of MAPbI<sub>3</sub>, optical phonons can indirectly influence the lifetime of acoustic phonons (from 5.4 to 3.61 ps) by phonon–phonon interactions, ultimately reducing  $\kappa$ .<sup>353</sup> This explains the experimentally observed sudden change in  $\kappa$  during the orthorhombic–tetragonal phase transition of MAPbI<sub>3</sub> from a microscopic perspective.

Numerical simulations were also employed to shed light on the origins of low  $\kappa$  in 3D MHPs. Yue *et al.* examined the effective phonon dispersions of the inorganic cages of MAPbI<sub>3</sub> by freezing the A-site MA<sup>+</sup> cations.<sup>233</sup> Nonequilibrium *ab initio* MD simulations indicate that MA<sup>+</sup> significantly influences the vibrational modes of the inorganic cages, although these effects are predominantly observed in the higher energy regions [Fig. 15(d)]. In contrast, the impact of A-site organic cations on the low-energy phonon spectrum can be considered negligible, which supports the claim that low  $\kappa$  is an intrinsic characteristic of the octahedral network. DFT calculations further revealed that clusters composed of Pb and I atoms are important phonon scattering sources in the low-frequency region.<sup>235</sup> The complex scattering mechanism results in a phonon MFP below 10 nm in many MHPs, e.g., as low as 3.9 nm in CsSnI<sub>3</sub> and 5.6 nm in CsPbBr<sub>3</sub>.<sup>235</sup> Combining the BTE and DFT, the cumulative  $\kappa$  with respect to phonon MFPs was calculated [Fig. 15(e)].<sup>235</sup> In the kinetic theory, the  $\kappa$  as a function of volumetric phonon heat capacity  $C$ , average group velocity  $v_g$ , and average MFP of phonons  $\bar{\Lambda}$  is expressed as<sup>34,247</sup>

$$\kappa = \frac{1}{3} Cv_g \bar{\Lambda}. \quad (14)$$

With this relation, the experimental average MFP can be estimated if the group velocity of phonon and heat capacity are known. Surprisingly, when the experimental data are organized by plotting  $\kappa$  as a function of  $Cv_g$ , the various 3D MHPs align quite linearly [Fig. 15(f)].<sup>34</sup> This suggests that all the 3D MHPs share a similarly low  $\bar{\Lambda}$  less than 10 nm and, importantly, that variations in  $\kappa$  among MHPs stem largely from differences in the sound speeds.

As for quasi-2D MHPs, besides the layered interfaces that serve as extra phonon scattering sources in the system compared with their 3D counterparts,  $[BX_6]^{4-}$  octahedra still play a crucial role in determining the phonon behaviors, in turn the thermal transport properties. The phonon modes of (C<sub>x</sub>H<sub>2x+1</sub>NH<sub>3</sub>)<sub>2</sub>PbI<sub>4</sub> ( $x=4-9$ ) in the range below 100 cm<sup>-1</sup> are predominantly attributed to the motions of the

Pb-I cage, as determined by investigating the influence of organic chain length on phonon spectrum with Raman spectroscopy [Fig. 16(a)].<sup>299</sup> Despite the high volumetric ratio of the organic sublattice in 2D organic-inorganic MHPs (~78%), the motion of the alkylammonium chain is shown to be primarily driven by the pulling of the heavy halide ions through Coulombic interactions and hydrogen bonding. This dynamic nature results in almost invariant phonon mode frequencies even when the organic chain length is doubled. Evidently, the halide ions dominate the overall vibrational modes, which suggests the feasibility of phonon engineering on both 3D and 2D MHPs, and consequently  $\kappa$  modification, by altering the  $[BX_6]^{4-}$  cages (e.g., constituents, connectivities, and distortions).

For instance, an effective  $\kappa$  of  $0.33 \pm 0.02 \text{ W}\cdot\text{m}^{-1}\cdot\text{K}^{-1}$  along with a thermal diffusivity of  $0.3 \pm 0.1 \text{ mm}^2\cdot\text{s}^{-1}$  and a small heat capacity of  $0.18 \pm 0.6 \text{ J}\cdot\text{g}^{-1}\cdot\text{K}^{-1}$  were measured and mapped simultaneously with 3 $\omega$ -based STHM on thin film CsPb<sub>2</sub>Br<sub>5</sub>.<sup>236</sup> In contrast, the effective  $\kappa$  of 2D CsPb<sub>2</sub>Cl<sub>5</sub> was measured to be  $0.40 \text{ W}\cdot\text{m}^{-1}\cdot\text{K}^{-1}$ .<sup>36</sup> The higher  $\kappa$  in chloride-based 2D MHPs compared to the bromide-based one aligns with the general trend that lighter halide ions lead to higher  $\kappa$  as observed in most MHPs regardless of dimensionalities.

## B. Role of A'-site organic spacers in 2D MHPs

In spite of the common roles of  $[BX_6]^{4-}$  in contributing to the low  $\kappa$  of MHPs, 2D (and quasi-2D) MHPs are subject to the impact of another constituents, A-site spacers. In Sec. IV, we primarily discussed the structural origins of the ultralow  $\kappa$  in 2D MHPs, which is even lower than their 3D counterparts due to the introduced interfacial scatterings. Here, the intrinsic influences of the A'-site spacers are discussed, which can serve as another angle to engineer the thermal transport properties of 2D MHPs. Note that we will primarily focus on the roles of organic spacers in hybrid 2D MHPs, as all-inorganic 2D MHPs with inorganic A'-site spacers generally contain mixed halides to form a stable structure (examples in Secs. IV D and IV E) and the sole effect of spacers are hard to distinguish.

Despite the insignificant role of organic-spacer lengths in dictating the thermal transport properties of 2D hybrid MHPs,<sup>256,299</sup> the lateral spacing and rigidity of the organic spacers were found to induce considerable changes in  $\kappa$ .<sup>257,316,354</sup> As shown in Fig. 16(b), MD simulations predict drastically increased  $\kappa$  in both the in-plane and cross-plane directions when the lateral distance between the adjacent organic chains is decreased.<sup>257</sup> The lateral van der Waals interactions between the organic chains contribute to the stiffness of the organic layer. The enhanced  $\kappa$  arises from the vibrational hardening, i.e., higher vibrational frequency, of the organic layer due to the increased van der Waals interactions at closer distances.<sup>316</sup> Experimentally, the lateral distance between the organic chains in the spacer layer can be tuned by varying the organic cations inside the inorganic subphase, or other constituent elements, thereby allowing synthetical manipulation of the metal-halide bond lengths and interlayer spacing.<sup>290</sup>

The rigidity of the organic spacer also plays a crucial role. 2D hybrid MHPs with aromatic groups as spacers, e.g., (PEA)<sub>2</sub>PbI<sub>4</sub> and (PEA)<sub>2</sub>PbBr<sub>4</sub>, were measured to have higher thermal diffusivities than those with alkyl-chain groups,<sup>38,257</sup> originating from the increased rigidity of organic spacer molecules via strong  $\pi-\pi$  interactions that facilitates faster energy transport<sup>355</sup> and decreases the phonon dephasing rates, i.e., weakens the phonon anharmonicity.<sup>43,354</sup> Temperature-dependent phonon dephasing rates of (PEA)<sub>2</sub>PbBr<sub>4</sub> and (BA)<sub>2</sub>PbBr<sub>4</sub>

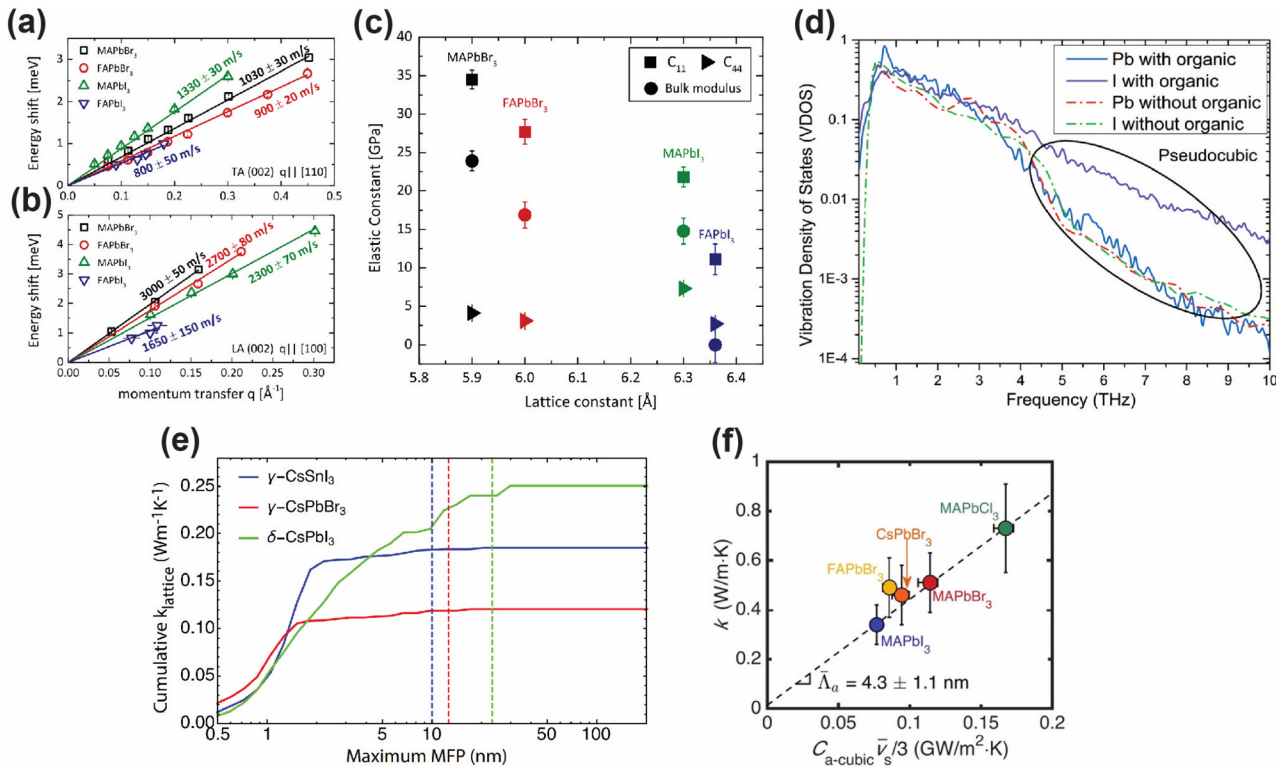


**FIG. 15.** (a) Transverse and (b) longitudinal acoustic phonon dispersion curves of MAPbBr<sub>3</sub> (black), FAPbBr<sub>3</sub> (red), MAPbI<sub>3</sub> (green), and FAPbI<sub>3</sub> (blue) at around the (002) Bragg reflection, measured by inelastic neutron scattering.<sup>351</sup> (c) Elastic constants  $C_{11}$  and  $C_{44}$  as well as the bulk modulus  $K$  as functions of the cubic lattice constant of each compound. Reproduced with permission from Phys. Rev. Lett. **121**, 085502 (2018). Copyright 2018 American Physical Society.<sup>351</sup> (d) Comparison of the partial vibrational density of states of Pb and I ions in the inorganic cages with and without organic MA<sup>+</sup> clusters. The solid lines are the results of normal pseudocubic structures (with MA<sup>+</sup>) and the dashed-dotted lines represent the empty pseudocubic inorganic cages (without MA<sup>+</sup>). Reproduced with permission from Phys. Rev. B. **94**, 115427 (2016). Copyright 2016 American Physical Society.<sup>233</sup> (e) Cumulative  $\kappa_{\text{lattice}}$  with respect to phonon MFPs at room temperature computed by a combination of BTE and DFT. Reproduced with permission from Proc. Natl. Acad. Sci. **114**, 8693–8697 (2017). Copyright 2017 National Academy of Sciences.<sup>235</sup> (f)  $\kappa$  as a function of  $C_{\text{a-cubic}}\sqrt{s}/3$ , where  $C_{\text{a-cubic}}$  is the volumetric heat capacity of acoustic phonons based on a cubic unit cell. The dashed line is a linear fit for MAPbX<sub>3</sub>. CsPbBr<sub>3</sub> is on the trendline, while FAPbBr<sub>3</sub> is above the trendline. The slope of the fit gives the average acoustic phonon mean free path  $\bar{\Lambda}_a = 4.3 \pm 1.1 \text{ nm}$ . Reproduced with permission from Elbaz *et al.*, Nano Lett. **17**(9), 5734–5739 (2017). Copyright 2017 American Chemical Society.<sup>34</sup>

were simulated with MD from 50 to 300 K [Fig. 16(c)]. A smaller phonon dephasing rate across all temperatures for (PEA)<sub>2</sub>PbBr<sub>4</sub> was present, indicating smaller anharmonicity. Additionally, the phonon dephasing of (BA)<sub>2</sub>PbBr<sub>4</sub> showed a very weak temperature dependence, which was attributed to the more significant disorder in its lattice, quantified by the spatial correlation relation between the nitrogen–carbon dipoles as  $C(r) = \langle \mu(0) \cdot \mu(r) \rangle$ . Here,  $\mu$  is the dipole moment separated by a distance of  $r$ . As shown in Fig. 16(c), the lower long-range correlation in (BA)<sub>2</sub>PbBr<sub>4</sub> implies a more amorphous packing, which is responsible for its temperature-insensitive phonon relaxation rate. Note that although PEA-based 2D MHPs generally exhibit larger thermal diffusivities than the BA-based counterparts, the thermal conductivities follow an opposing trend. The origin of this discrepancy is that thermal diffusivity and thermal conductivity are two properties describing different aspects of thermal transport. Thermal diffusivity is a measure of speed or rate of heat flow and mainly correlates with how quickly a material responds to temperature change. On the other hand, thermal conductivity is a measure of ability to conduct heat, which is about the magnitude of heat flow rather than speed, and

influenced by other material properties such as density and heat capacity as in Eq. (2).

For RP-phase 2D MHPs wherein monovalent cation spacers are included, the interaction strength at the interfaces of two spacers was shown to have significant influence on both thermal and mechanical behaviors of the materials.<sup>259,356</sup> While a positive correlation between elastic modulus and  $\kappa$  is usually observed for soft materials,<sup>357,358</sup> by engineering the interactions between spacers, Negi *et al.* achieved anomalous correlations, i.e., anti-correlation and uncorrelation, between these two properties as summarized in Fig. 16(d).<sup>259</sup> Grounded in the tendency that stronger interactions at the interfaces generally lead to faster but weaker capability to conduct heat across the interface,<sup>267,358,359</sup> and higher stiffness (i.e., larger elastic modulus),<sup>360–362</sup> independent modifications on the thermal and mechanical properties of 2D RP MHPs were managed by choosing the bonding types and ratios at the spacer interfaces. When both alkyl and aryl spacers are present, possible interactions at the interfaces include van der Waals (alkyl–alkyl), CH– $\pi$  (alkyl–aryl), and  $\pi$ – $\pi$  (aryl–aryl) with increasing strengths. Hard but thermally insulative or soft but thermally conductive 2D

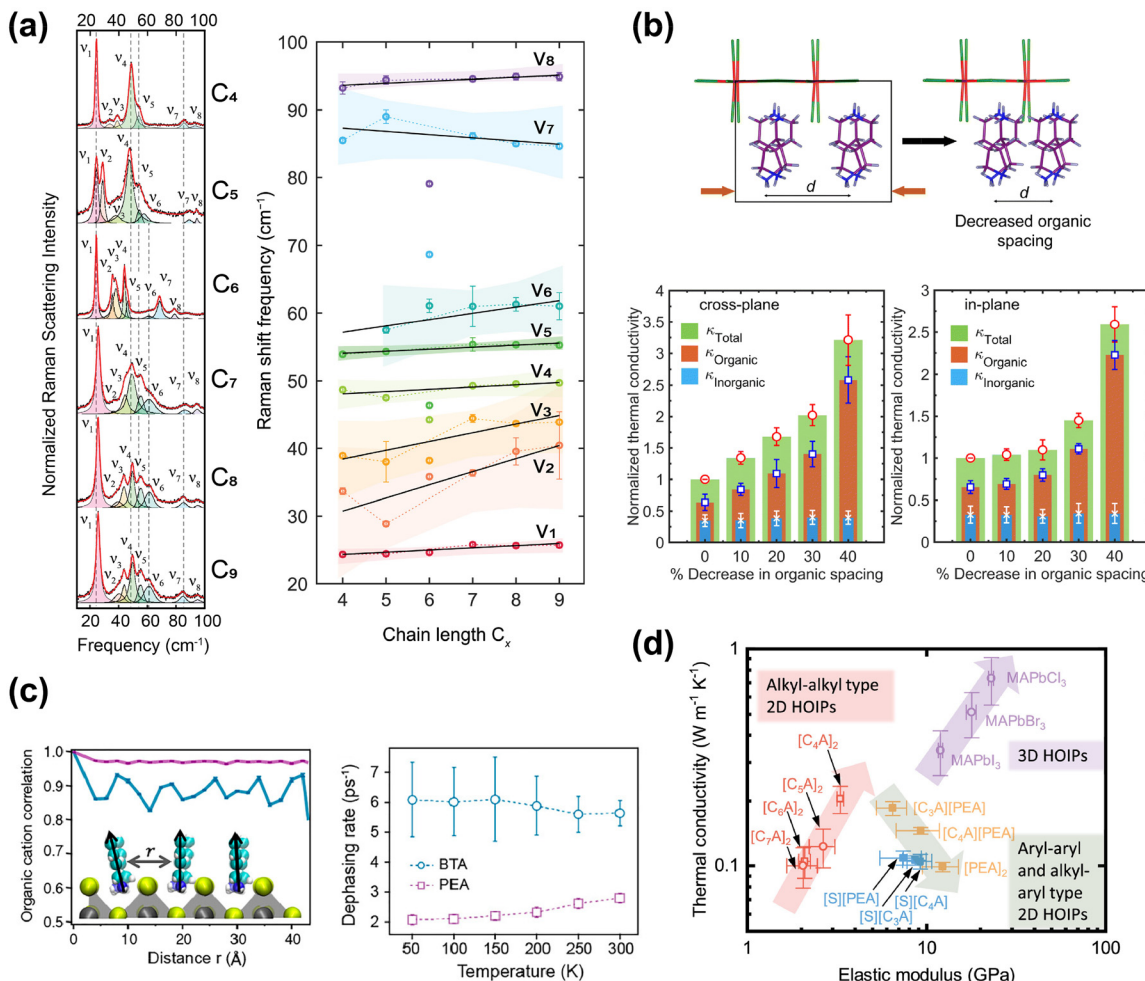


**FIG. 16.** (a) Left panel: non-resonant continuous wave Raman spectra of 2D MHPs with varying lengths of alkylammonium (number of carbons from 4 to 9) at 78 K. Right panel: Raman shifts of the modes as a function of chain lengths. Reproduced with permission from Mauck *et al.*, *J. Phys. Chem. C* **123**(45), 27904–27916 (2019). Copyright 2019 American Chemical Society.<sup>299</sup> (b) Enhanced thermal conductivities in both cross-plane and in-plane directions with decreasing lateral spacing between the organic spacers, calculated with MD simulation. Reproduced with permission from Thakur *et al.*, *Mater. Horiz.* **9**, 3087–3094 (2022). Copyright 2022 Royal Society of Chemistry.<sup>257</sup> (c) MD-simulated spatial correlations between the nitrogen–carbon dipole in the organic spacers as a function of the lateral distance between the dipoles (left panel), and the dephasing rate of the lowest optical mode (right panel) in (BA)<sub>2</sub>PbBr<sub>4</sub> (blue) and (PEA)<sub>2</sub>PbBr<sub>4</sub> (purple). Reproduced with permission from Quan *et al.*, *Proc. Natl. Acad. Sci. U. S. A.* **118**(25), e2104425118 (2021). Copyright 2021 National Academy of Sciences.<sup>354</sup> (d) Correlations between thermal conductivities and elastic moduli of various 2D MHPs. Different interactions are present in 2D MHPs with different spacers incorporated. [C<sub>n</sub>A] represents (C<sub>n</sub>H<sub>2n+1</sub>NH<sub>3</sub>)<sup>+</sup>, and [S] represents (S-MePEA)<sup>+</sup>. Reproduced with permission from Negi *et al.*, *ACS Nano* **18**, 14218–14230 (2024). Copyright 2024 American Chemical Society.

MHPs exhibiting anti-correlation can thus be designed through tailoring the spacer interactions by mixing different spacers, as illustrated in the yellow marked materials in Fig. 16(d). Furthermore, introduction of chiral spacers was found to affect the structural and molecular packing, and also induce diverse orientations of phenyl rings, which contribute collectively to almost constant (uncorrelated)  $\kappa$  with increased elastic modulus.

## VI. OTHER THIRD-GENERATION PHOTOVOLTAIC MATERIALS

Beyond MHPs, thermal transport measurements of other third-generation PV materials, such as 0D QDs and environmental-friendly

CZTS, are summarized in this section. We note that the thermal transport properties of conventional PV materials, such as silicon, GaAs, CdTe, and CIGS, have been extensively studied with the steady-state heat flow,<sup>336,363</sup> laser flash,<sup>42,364</sup> and photoacoustic methods.<sup>334,365,366</sup>

### A. Quantum Dots (QDs)

As a branch of third-generation PV materials, colloidal QDs hold promise for exceeding the Shockley–Queisser single-junction limit through the more efficient multi-carrier generation.<sup>367</sup> Various materials in their QD form have been successfully integrated into solar cells,

such as PbS,<sup>368</sup> PbSe,<sup>369</sup> CdTe,<sup>370,371</sup> CdSe,<sup>370,372,373</sup> CdS,<sup>373,374</sup> and graphene.<sup>375–378</sup>

The phonon bottleneck effect, which slows the hot carrier cooling rate, can facilitate the impact ionization effect for multi-exciton generation in these materials, potentially resulting in higher PV efficiency. Such effect was first reported for CdSe QDs<sup>379,380</sup> and later also observed in hybrid MHPs.<sup>294</sup> As mentioned in previous sections, a stronger phonon bottleneck effect could benefit from the low  $\kappa$  of the materials. On the other hand, the low  $\kappa$  of QDs also presents challenges for heat dissipation in practical solar cells and LEDs with high operating temperatures to ensure a longer device lifetime and more stable performance.<sup>381–383</sup> The low  $\kappa$  and appropriate electrical conductivity also make them favorable for thermoelectrics.<sup>384</sup> Despite numerous efforts on measuring the electrical transport properties of QDs, research focusing on their thermal transport properties remains relatively limited,<sup>170,385–397</sup> yet equally important for both better thermal managements and PV performance.

### 1. Metal chalcogenide QDs

Two features that significantly influence the thermal transport properties of QDs or nanocrystals (NCs) come with the intrinsic low dimensionality (several digits of nm in sizes). One is the increased heat capacity due to increased surface-to-volume ratio,<sup>395,398,399</sup> second is the high density of organic-inorganic interfaces between the ligands and cores,<sup>400</sup> both of which will largely suppress thermal transport. The first systematic investigation on the thermal transport properties and influencing factors of QDs is credited to Ong *et al.*, who measured ultralow  $\kappa$  of several NCs using FDTR and obtained a high tunability on thermal transport properties by modifying the surface chemistry.<sup>390</sup>

Multiple factors have been reported to influence the thermal transport properties, among which the size effect is a most prominent factor. As shown in Fig. 17(a), QDs with larger particle sizes exhibit higher  $\kappa$ ,<sup>391,396,401</sup> which is attributed to the decreased heat capacity<sup>390,395</sup> and interfacial density.<sup>390</sup> Concurrently, the sound speed and phonon MFPs were also found to increase with sizes, all the above contributions lead to an over 100% enhancement in  $\kappa$  of PbS NC superlattice, from 0.32 to 0.75 W·m<sup>-1</sup>·K<sup>-1</sup>, when the diameters of PbS NCs increase from 3 nm to 6.1 nm.<sup>396</sup> Similarly, highly grain size-dependent  $\kappa$  of CdSe NC films were measured to range 0.2–0.45 W·m<sup>-1</sup>·K<sup>-1</sup> for grain sizes within 3–6 nm, the value of which is notably lower than the amorphous limit.<sup>391</sup> The greatly suppressed thermal transport and strong size effect of  $\kappa$  suggest the dominant role of boundary scatterings in these systems.

In addition to the particle size, other factors also provide approaches to engineer the thermal transport properties of QDs, such as the ligand chemistry. Modification of the surface chemistry by exchanging the ligands is vastly applied to enhance the electrical properties of QDs,<sup>402–404</sup> and is also found to greatly influence the thermal transport properties.<sup>389,390,405</sup> The ligand chemistry may influence the overall  $\kappa$  in different ways as summarized in Fig. 17(b). First, the weak ligand–ligand interaction strength is considered as the primary limiting factors for efficient thermal transport.<sup>389</sup> The organic ligands connect with the inorganic core by strong covalent bonding, while the ligands interact with each other or with the environment with relatively weak van der Waals bonding.<sup>406–408</sup> Empirically, the rate of thermal transport across these interfaces scales with the interaction strength, i.e., stronger interaction at the interfaces should result in a

larger interfacial thermal conductance.<sup>359</sup> While it was found that with careful choices of ligands to strengthen the ligand–ligand interactions,  $\kappa$  of PbS QDs films was enhanced by up to 150%, little effect of ligand–core interaction or  $\kappa$  of cores was shown.<sup>389,390</sup> Second, in a system where QDs are dispersed in a matrix solvent, interaction between the ligands and environments provides another dimension to modify the thermal transport. Solvents with better solubility and more matching vibrational energies with the ligands were shown to facilitate the cooling of QDs by efficiently taking the heat away.<sup>393</sup> Exchanging the organic ligands with inorganic chalcogen ligands, such as Se<sup>2-</sup>, enables simultaneous enhancement in electronic and mechanical coupling between the QDs and environments, leading to better electrical conductivity and faster heat dissipation.<sup>409</sup> Moreover, even if the ligands have the same chemical characteristics, simply altering the length of the ligands to modify the spacing between cores will modify thermal transport properties, wherein a higher  $\kappa$  is observed for smaller spacing.<sup>389,390</sup> Other factors such as the long-range ordering and ligand grafting density also influence the thermal transport in QDs, with  $\kappa$  in ordered PbS NC superlattice up to ~3 times higher than randomly oriented films,<sup>396</sup> and larger interfacial thermal conductance between the core and ligands in QDs with larger ligand grafting density.<sup>266,389,397</sup>

The predominant role of ligand–ligand and ligand–environment interaction, and negligible effect of the core properties on the overall  $\kappa$  were explicitly verified by Liang *et al.* using an infrared-pump-electronic-probe (IPEP) spectroscopy,<sup>397</sup> which is a similar technique to VPVP as discussed in Sec. III B 4. By vibrationally exciting the C–H bonds in the ligands with an ultrashort infrared laser pulse, the heat flow across the ligand/core and ligand/environment interfaces during the heat-cool period of CdSe QDs was monitored by the transient absorption redshift of CdSe core using a visible probe light.<sup>392,393</sup> In contrast to other works discussed here that measured the overall thermal transport, this ultrafast spectroscopic method distinguishes the thermal transport across the core/ligand and ligand/solvent interfaces in the QD suspensions. As expected from the distinct bonding energies between the covalent and van der Waals bonds, the interfacial thermal conductance between the oleate ligand and CdSe core,  $h_{\text{NC-lig}} \approx 103 \text{ MW}\cdot\text{m}^{-2}\cdot\text{K}^{-1}$  was found to be almost an order of magnitude higher than that between ligands and solvent,  $h_{\text{lig-sol}} \approx 14 \text{ MW}\cdot\text{m}^{-2}\cdot\text{K}^{-1}$  for a broad range of grafting densities and sizes as illustrated in Fig. 17(c).<sup>397</sup> The finding again attributed the ligand–solvent interaction as the bottleneck to thermal transport in QD matrices.

### 2. Graphene QDs

While metal-sulfide and metal-selenide QDs have been the prevailing focus for photovoltaics, another promising carbon-based QDs, graphene QDs (GQDs), are emerging for their advantageous features such as low toxicity, excellent biocompatibility, and high photostability.<sup>375,377</sup> In addition to their wide applications as light-absorbers, carrier transport layers,<sup>376,411</sup> and sensitizers<sup>412,413</sup> in solar cells, their intrinsically ultrahigh  $\kappa$  makes them potential candidates for thermal management layers.<sup>388,414</sup> One of the primary configurations of incorporating QDs into solar cells is to disperse the QDs in the electron/hole conducting polymers,<sup>23,415</sup> which can alter the effective thermal transport properties. Therefore, instead of exploring the thermal transport in bare GQDs,<sup>388,416</sup> researchers focus more on the properties when GQDs are in suspension forms or form a composite with other

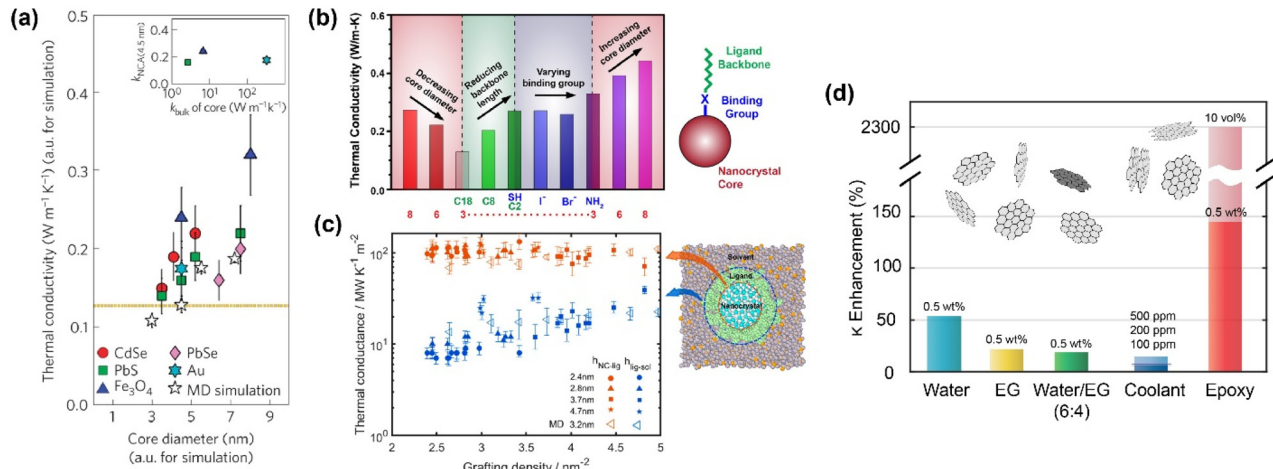


**FIG. 17.** (a) Size-dependent thermal conductivities of nanocrystalline CdSe, PbSe, PbS, Au, and  $\text{Fe}_3\text{O}_4$  films measured with FDTR, together with MD simulated values. The inset shows that the nanocrystal  $\kappa$  is insensitive to the bulk  $\kappa$  of the core materials. The orange-dashed line represents the  $\kappa$  of Pb oleate at 300 K. Reproduced with permission from Ong *et al.*, Nat. Mater. **12**(5), 410–415 (2013). Copyright 2013 Springer Nature.<sup>390</sup> (b) Thermal conductivities of PbS nanocrystals modified by core diameters (red and purple), ligand lengths (green), and ligand binding strengths (blue). Reproduced with permission from Liu *et al.*, ACS Nano **9**(12), 12079–12087 (2015). Copyright 2015 American Chemical Society.<sup>389</sup> (c) Interfacial thermal conductance of the nanocrystal-ligand (orange) and ligand-solvent (blue) interfaces with varying grafting densities and crystal sizes. Reproduced with permission from Liang *et al.*, Nano Lett. **23**(9), 3687–3693 (2023). Copyright 2023 American Chemical Society.<sup>397</sup> (d) Thermal conductivity enhancement of the base material when a small amount of graphene (and/or multi-layer-graphene) nanoplatelets are added into distilled water, ethylene glycol (EG), a mixture of water and EG (6:4), car coolant, and epoxy. Increased particle concentration (100, 200, and 500 ppm) results in higher enhancement. The light red bar shows the epoxy incorporated with a mixture of mono- and multi-layer graphene. Data are taken from Refs. 418–422.

polymers. The enhancement in  $\kappa$  with the addition of GQDs is summarized in Fig. 17(d).

Nanofluids, formed by suspended nanoparticles in a base fluid, have shown their advantages in photovoltaics.<sup>417</sup> The small particle sizes, thus the high surface area, lead to significantly increased specific heat, favorable for solar collectors. The presence of nanoparticles also enhances the  $\kappa$  of base fluids, which helps achieve improved thermal management in these systems. Dispersing GQDs in nanofluids has been shown to considerably increase the  $\kappa$  of base fluids.<sup>418–420</sup> Enhancements of as much as 53%, 21%, and 18% in the  $\kappa$  have been achieved with 0.5%wt GQDs suspended in water, ethylene glycol, and a 6:4 water/ethylene glycol mixture at 323 K, respectively.<sup>420</sup> A concentration dependence revealed an increase in  $\kappa$  enhancement from 5% to 7% when the concentration of GQDs in car radiator coolant varies from 100 to 500 ppm.<sup>419</sup> Apart from increased  $\kappa$ , a massive enhancement in the electrical conductivity (up to 140 times) was also reported for GQDs dispersed in distilled water.<sup>418</sup> In addition to GQDs nanofluids, composites formed with GQDs dispersed in polymers also exhibit superior thermal transport performance. Enhancements of up to 144% in  $\kappa$ , as well as 260% in toughness, have been found for 5%wt loading of GQDs in epoxy.<sup>170,421</sup> Furthermore, by carefully mixing graphite with different thickness and lateral sizes in a specific ratio, the  $\kappa$  of epoxy can be enhanced by a record-high value of 2300%.<sup>422</sup>

## B. Copper zinc tin sulfide/selenide (CZTS/Se)

Another class of third-generation PV materials attracting much attention are  $\text{Cu}_2\text{ZnSnS}_4$  (CZTS) and  $\text{Cu}_2\text{ZnSnSe}_4$  (CZTSe). CZTS and CZTSe are considered promising alternatives to CIGS due to a

replacement of the rare indium and gallium with nontoxic and earth-abundant zinc and tin. Compared with other all-inorganic PV materials, CZTS/Se feature a remarkably low  $\kappa$ , making them also potential candidates for thermoelectric applications.<sup>423–425</sup> Note that although single-crystalline CZTS/Se were measured and calculated to have much higher  $\kappa$  than thin films,<sup>426,427</sup> polycrystalline thin films are the predominant forms for their PV applications.

CZTS, also referred to as the kesterite, usually forms a stable crystallographic structure of ordered tetragonal (space group  $I-4$ ), which evolves into a disordered tetragonal structure ( $I-42m$ ) above 532 K through a reversible phase transition.<sup>428</sup>  $\kappa$  lower than  $1 \text{ W m}^{-1} \cdot \text{K}^{-1}$  was found for tetragonal CZTS over a wide temperature range from 80 to 700 K by various methods, specifically  $3\omega$ ,<sup>423,429</sup> TDTR,<sup>430</sup> and LFA.<sup>428,431</sup> The low  $\kappa$  was generally attributed to the crystal complexity of the quaternary compounds and the abundant presence of defects, mainly cationic disorders<sup>430</sup> and vacancies.<sup>429</sup>

Additionally, a disordered cubic phase of CZTS that remains stable at temperatures up to 650 K can be synthesized by high-energy mechanical alloying.<sup>432</sup> Such an uncommon phase of CZTS was found to exhibit largely suppressed ( $\sim 3$  times reduction) and temperature-insensitive  $\kappa$  in the temperature window below 650 K as presented in Fig. 18(a).<sup>428</sup> Above 650 K, it goes through a phase transition back to the tetragonal phase. More intriguingly, an over two-fold enhancement in electrical conductivity was simultaneously achieved in CZTS when transformed into the cubic phase. The peculiar behavior was attributed to the strong localization of  $s^2$  lone pair electrons in some Sn atoms that (1) leads to Sn-ion rattling, evident in the low-frequency optical phonon modes via which lattice energy dissipates; and (2) causes *p*-type doping-like

effect with highly localized acceptor levels originating from the presence of charge-deficient Sn-S bonds.

For tetragonal CZTS, a flexible tuning (either increasing or decreasing) of its  $\kappa$  can be achieved via manipulating the defect concentration. By sulfurizing CZTS thin films to reduce the number of sulfur vacancies, a 4.5-fold increase in  $\kappa$  at room temperature was achieved, from 0.9 to 4.0  $\text{W}\cdot\text{m}^{-1}\cdot\text{K}^{-1}$ .<sup>429</sup> Such enhancement is even

more prominent under low temperatures, reaching a peak  $\kappa$  of 6.8  $\text{W}\cdot\text{m}^{-1}\cdot\text{K}^{-1}$  at 145 K [Fig. 18(b)]. Thermal treatment after the film growth can also modify the thermal transport properties by introducing a higher degree of cation disorder.<sup>430</sup> While the standard ordered CZTS films were measured to exhibit a  $\kappa$  of 0.69  $\text{W}\cdot\text{m}^{-1}\cdot\text{K}^{-1}$  with TDTR, the highly disordered crystals produced by thermal annealing under different temperatures show lower  $\kappa$ , spanning

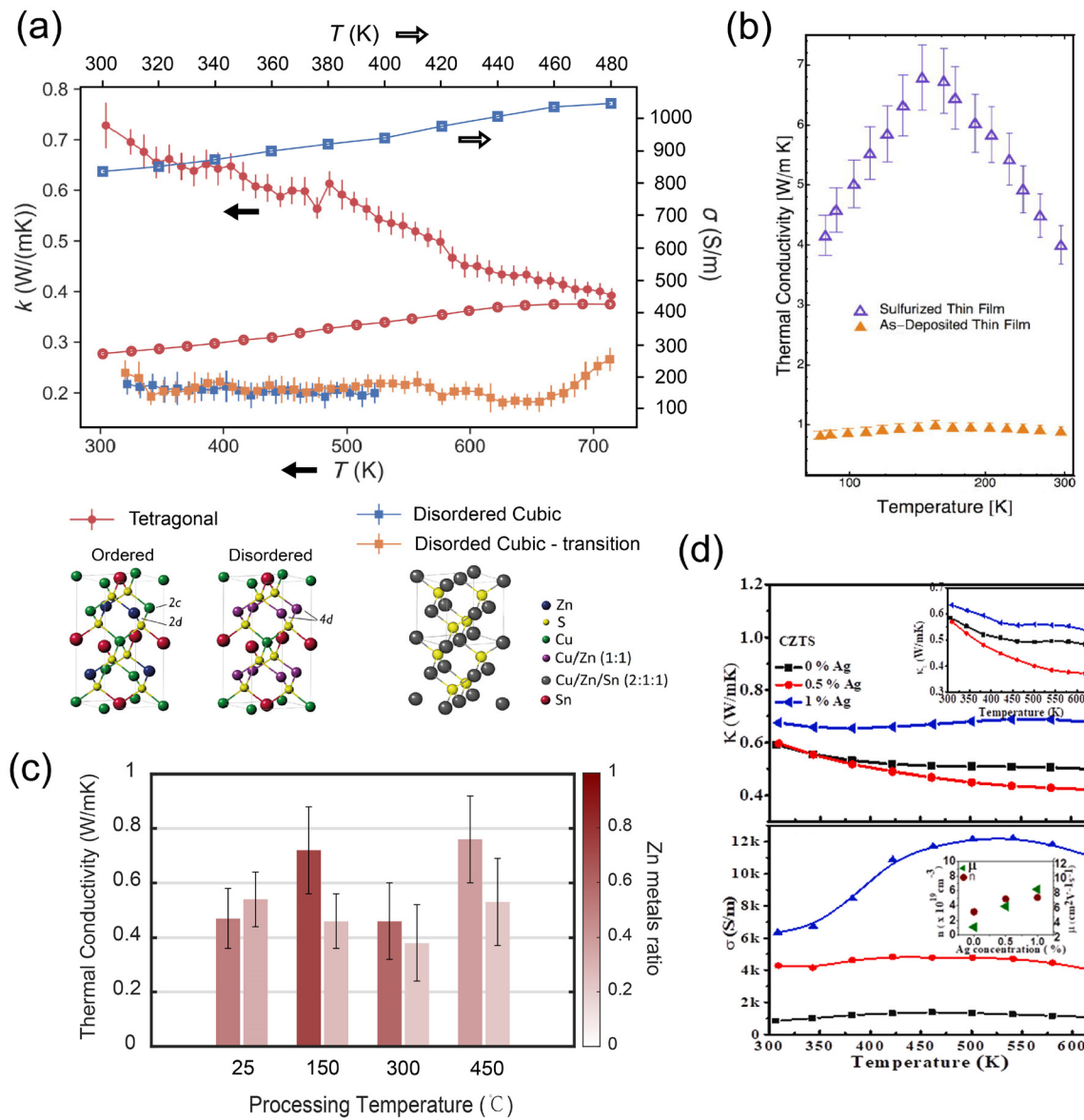


**FIG. 18.** (a) Thermal conductivities (filled markers) and electrical conductivities (empty markers) of CZTS in tetragonal and cubic phases as a function of temperature measured with LFA. Reproduced with permission from Isotta *et al.*, Phys. Rev. Appl. **14**, 064073 (2020). Copyright 2020 American Physical Society.<sup>428</sup> (b) Thermal conductivities of the pulsed-laser-deposited pristine (orange) and sulfurized (purple) CZTS thin films as a function of temperature measured with  $3\omega$  method. Reproduced with permission from Thompson *et al.*, J. Appl. Phys. **119**, 095108 (2016). Copyright 2016 AIP Publishing.<sup>429</sup> (c) Flexible tuning of thermal conductivities of CZTS thin film by adjusting the Zn metals ratio and annealing temperatures after film growth measured with TDTR. Reproduced with permission from Ye *et al.*, Chem. Mater. **31**, 8402–8412 (2019). Copyright 2019 American Chemical Society.<sup>430</sup> (d) Thermal conductivities (upper panel) and electrical conductivities (lower panel) of CZTS incorporated with varying amounts of Ag nanoparticles measured with LFA. Reproduced with permission from Sharma *et al.*, Ceram. Int. **45**(2), 2060–2068 (2019). Copyright 2019 Elsevier.

$0.38\text{--}0.54 \text{ W}\cdot\text{m}^{-1}\cdot\text{K}^{-1}$  as summarized in Fig. 18(c). The structural disorder from the stacking faults and the inhomogeneity from randomly ordered cations were found to contribute to the reduced  $\kappa$ . At the same time, introducing excess ZnS during synthesis to grow Zn-rich CZTS can further modify the density of crystallographic defects, achieving a remarkable tunability in  $\kappa$  of carefully engineered CZTS films from as low as  $0.4 \text{ W}\cdot\text{m}^{-1}\cdot\text{K}^{-1}$  to as high as  $0.8 \text{ W}\cdot\text{m}^{-1}\cdot\text{K}^{-1}$  [Fig. 18(c)]. Incorporating metal nanoparticles such as Ag and Cu has been a common strategy to modify the thermal and electrical conductivities of semiconductors.<sup>433–437</sup> A small addition of Ag nanoparticles into CZTS was shown to suppress thermal transport through enhanced phonon scattering originating from the increased amount of grain boundaries while simultaneously increase its electrical conductivity.<sup>431</sup> Further addition of Ag nanoparticles, on the other hand, facilitates thermal transport because of the intrinsically large  $\kappa$  of Ag as shown in Fig. 18(d). As for CZTSe, although it shares similar crystallographic structure and properties to CZTS, CZTSe generally features higher  $\kappa$  due to the softer phonon modes and thus longer phonon lifetimes.<sup>426</sup>

## VII. SUMMARY AND OUTLOOK

Third-generation PV materials, particularly MHPs, semiconducting QDs, and CZTS/Se, are emerging as promising candidates to supersede conventional solar cells in large-scale applications. Despite advantageous electrical and optical properties, the ubiquitously low thermal conductivities observed in these materials present formidable challenges in efficient heat dissipation during practical uses. Effective thermal management is pivotal to mitigating heat accumulation, which can precipitate thermal degradation, curtailed operational lifespan, diminished stability, and reduced efficiency. Consequently, there has been a paradigm shift from solely enhancing electrical transport to a more holistic approach that also emphasizes the significance of thermal transport in these materials. The development of more precise and versatile measurement techniques, along with a thorough understanding of thermal transport, are essential for formulating strategies to enhance thermal management, thereby achieving higher efficiency and more stable device performance.

Motivated by these considerations, we presented a comprehensive review of the techniques widely employed to measure the thermal transport properties of various third-generation PV materials. We elucidated and compared the working principles, application conditions, sample requirements, specialties, and data interpretation of various photothermal and electrothermal methods. While electrothermal methods boast a longer developmental history and ease of implementation, the non-contact and more versatile optical methods offer robust and flexible approaches to measure various types of materials, extending beyond photovoltaics, and encompassing a broad spectrum of properties beyond thermal transport. In addition to the methods we discussed here, the innovation of novel optical methods for thermal transport measurement that provides both temporal and spatial resolution, such as thermal imaging, represents a burgeoning field that will pave the way for advanced thermal management from macroscopic to microscopic scales.

From a materials perspective, we delved into the fundamental origins of the ultralow thermal conductivities of these third-generation PV materials. The inorganic octahedra in both 3D and 2D forms of MHPs play a predominant role in determining the phonon dispersions and vibrational modes, which in turn influence the thermal transport properties. This characteristic permits thermal-property engineering

by adjusting the constituent metal and halide ions. Lower-dimensional 2D MHPs exhibit stronger excitonic effects, higher moisture stability, and improved structural diversity over their 3D counterparts. However, the high concentration of organic-inorganic interfaces in the layered structures of 2D MHPs further impedes thermal transport in the cross-plane direction, rendering efficient heat dissipation more challenging. Strategies to address the low thermal conductivity of the broad MHPs family include phonon engineering through constructing phononic structures,<sup>438</sup> composition modification on the  $[\text{BX}_6]^{4-}$  octahedra,<sup>36,301</sup> and morphology tailoring of the film by controlling the grain sizes and orientations.<sup>9,150,439,440</sup> Unique to quasi-2D MHPs, thermal transport can be enhanced by augmenting the portion of heat carried by the coherent longitudinal acoustic phonons through phonon band structure engineering, similar to the approach used in superlattices.<sup>263,317</sup> Additionally, exploiting the anisotropic nature of the structure can facilitate faster heat transfer in the in-plane direction, analogous to the accelerated charge transport observed along this direction.<sup>441</sup> Furthermore, the structurally and compositionally more complex 2D MHPs offer greater flexibility to independently modulate their thermal transport, optical, electronic, and mechanical properties.<sup>257,259,289</sup> Apart from enhancing the intrinsic thermal conductivity of MHPs, strengthening their mechanical coupling with adjacent layers in devices (e.g., ETL and HTL) through interfacial toughening can also promote better heat dissipation. This approach not only improves thermal management but also enhances PV efficiencies by simultaneously boosting charge transport across the contact interfaces.<sup>142–144</sup>

Metal chalcogenide QDs, akin to 2D MHPs, exhibit tunable optoelectronic properties through quantum confinements. Despite the shared origins of ultralow thermal conductivities with 2D MHPs, i.e., organic-inorganic interfaces, the thermal transport properties of QDs are predominantly influenced by the organic ligands, including their lengths, functional groups, solubility in the solvents, and rigidity. Surface chemistry modification through different ligand choices provides a potential approach to tune the thermal properties of QDs. Conversely, graphene QDs possess relatively high thermal conductivities, promising superior thermal management when integrated into a matrix material. The low thermal conductivities of CZTS/Se, attributable to the high level of cation disorder in their complex crystal structures, can also be managed by defect engineering or phase control.

In summation, measuring and comprehending the thermal transport properties of third-generation PV materials are as pivotal as their optoelectronic properties for further advancing PV performance. While the intrinsically poor thermal conductance of these promising materials imposes challenges for more efficient heat dissipation in applications such as solar cells, LEDs, photodetectors, and other electronic and optoelectronic applications, various strategies have been proposed to surmount this limitation. Meanwhile, low thermal conductivities could be advantageous for enhanced phonon bottleneck effects that improve PV efficiencies, and for other energy applications such as thermoelectrics. These factors underscore the imperative for more sophisticated thermal management strategies in these materials.

## ACKNOWLEDGMENTS

This material is based upon the work supported by the National Science Foundation under Grant No. DMR-2313648. P.G. also acknowledges the support from ACS Petroleum Research Fund (65716-DNI6).

## AUTHOR DECLARATIONS

## Conflict of Interest

The authors have no conflicts to disclose.

## Author Contributions

**Du Chen:** Investigation (equal); Writing – original draft (equal).  
**Shunran Li:** Investigation (equal); Writing – original draft (equal).  
**Bowen Li:** Investigation (equal); Writing – original draft (equal).  
**Peijun Guo:** Conceptualization (equal); Funding acquisition (equal); Supervision (equal); Writing – original draft (equal); Writing – review & editing (equal).

## DATA AVAILABILITY

Data sharing is not applicable to this article as no new data were created or analyzed in the study.

## REFERENCES

- <sup>1</sup>G. F. Brown and J. Wu, *Laser Photonics Rev.* **3**(4), 394 (2009).
- <sup>2</sup>M. A. Green, “Introduction,” in: *Third Generation Photovoltaics*, Springer Series in Photonics Vol. 12 (Springer, Berlin, Heidelberg, 2006).
- <sup>3</sup>A. Kojima, K. Teshima, Y. Shirai, and T. Miyasaka, *J. Am. Chem. Soc.* **131**(17), 6050 (2009).
- <sup>4</sup>M. A. Green, A. Ho-Baillie, and H. J. Snaith, *Nat. Photonics* **8**(7), 506 (2014).
- <sup>5</sup>H. Zhou, Q. Chen, G. Li, S. Luo, T.-B. Song, H.-S. Duan, Z. Hong, J. You, Y. Liu, and Y. Yang, *Science* **345**(6196), 542 (2014).
- <sup>6</sup>H. S. Kim, C. R. Lee, J. H. Im, K. B. Lee, T. Moehl, A. Marchioro, S. J. Moon, R. Humphry-Baker, J. H. Yum, J. E. Moser, M. Grätzel, and N. G. Park, *Sci. Rep.* **2**, 591 (2012).
- <sup>7</sup>N. J. Jeon, J. H. Noh, Y. C. Kim, W. S. Yang, S. Ryu, and S. I. Seok, *Nat. Mater.* **13**(9), 897 (2014).
- <sup>8</sup>S. Liu, J. Li, W. Xiao, R. Chen, Z. Sun, Y. Zhang, X. Lei, S. Hu, M. Kober-Czerny, J. Wang, F. Ren, Q. Zhou, H. Raza, Y. Gao, Y. Ji, S. Li, H. Li, L. Qiu, W. Huang, Y. Zhao, B. Xu, Z. Liu, H. J. Snaith, N.-G. Park, and W. Chen, *Nature* **632**, 536–542 (2024).
- <sup>9</sup>J.-H. Im, I.-H. Jang, N. Pellet, M. Grätzel, and N.-G. Park, *Nat. Nanotechnol.* **9**(11), 927 (2014).
- <sup>10</sup>H. Min, D. Y. Lee, J. Kim, G. Kim, K. S. Lee, J. Kim, M. J. Paik, Y. K. Kim, K. S. Kim, M. G. Kim, T. J. Shin, and S. Il Seok, *Nature* **598**(7881), 444 (2021).
- <sup>11</sup>J. J. Yoo, G. Seo, M. R. Chua, T. G. Park, Y. Lu, F. Rotermund, Y.-K. Kim, C. S. Moon, N. J. Jeon, J.-P. Correa-Baena, V. Bulović, S. S. Shin, M. G. Bawendi, and J. Seo, *Nature* **590**(7847), 587 (2021).
- <sup>12</sup>X. Li, D. Bi, C. Yi, J.-D. Décopet, J. Luo, S. M. Zakeeruddin, A. Hagfeldt, and M. Grätzel, *Science* **353**(6294), 58 (2016).
- <sup>13</sup>Y. Chen, Y. Sun, J. Peng, J. Tang, K. Zheng, and Z. Liang, *Adv. Mater.* **30**(2), 1703487 (2018).
- <sup>14</sup>R. E. Beal, D. J. Slotcavage, T. Leijtens, A. R. Bowring, R. A. Belisle, W. H. Nguyen, G. F. Burkhard, E. T. Hoke, and M. D. McGehee, *J. Phys. Chem. Lett.* **7**(5), 746 (2016).
- <sup>15</sup>J. M. Ball and A. Petrozza, *Nat. Energy* **1**(11), 16149 (2016).
- <sup>16</sup>J. Kim, S.-H. Lee, J. H. Lee, and K.-H. Hong, *J. Phys. Chem. Lett.* **5**(8), 1312 (2014).
- <sup>17</sup>A. K. Jena, A. Kulkarni, and T. Miyasaka, *Chem. Rev.* **119**(5), 3036 (2019).
- <sup>18</sup>W.-J. Yin, T. Shi, and Y. Yan, *J. Phys. Chem. C* **119**(10), 5253 (2015).
- <sup>19</sup>M. E. Kamminga, H.-H. Fang, M. R. Filip, F. Giustino, J. Baas, G. R. Blake, M. A. Loi, and T. T. M. Palstra, *Chem. Mater.* **28**(13), 4554 (2016).
- <sup>20</sup>C. Murray, D. J. Norris, and M. G. Bawendi, *J. Am. Chem. Soc.* **115**(19), 8706 (1993).
- <sup>21</sup>L. E. Brus, *J. Chem. Phys.* **80**(9), 4403 (1984).
- <sup>22</sup>A. Shabaei, A. L. Efros, and A. J. Nozik, *Nano Lett.* **6**(12), 2856 (2006).
- <sup>23</sup>O. E. Semonin, J. M. Luther, and M. C. Beard, *Mater. Today* **15**(11), 508 (2012).
- <sup>24</sup>M. Ravindiran and C. Praveenkumar, *Renewable Sustainable Energy Rev.* **94**, 317 (2018).
- <sup>25</sup>H. Katagiri, K. Jimbo, W. S. Maw, K. Oishi, M. Yamazaki, H. Araki, and A. Takeuchi, *Thin Solid Films* **517**(7), 2455 (2009).
- <sup>26</sup>A. D. Sheikh, R. Munir, M. A. Haque, A. Bera, W. Hu, P. Shaikh, A. Amassian, and T. Wu, *ACS Appl. Mater. Interfaces* **9**(40), 35018 (2017).
- <sup>27</sup>R. L. Milot, G. E. Eperon, H. J. Snaith, M. B. Johnston, and L. M. Herz, *Adv. Funct. Mater.* **25**(39), 6218 (2015).
- <sup>28</sup>C. Quarti, E. Mosconi, J. M. Ball, V. D’Innocenzo, C. Tao, S. Pathak, H. J. Snaith, A. Petrozza, and F. De Angelis, *Energy Environ. Sci.* **9**(1), 155 (2016).
- <sup>29</sup>A. Dualeh, P. Gao, S. Il Seok, M. K. Nazeeruddin, and M. Grätzel, *Chem. Mater.* **26**(21), 6160 (2014).
- <sup>30</sup>J. He, T. Li, X. Liu, H. Su, Z. Ku, J. Zhong, F. Huang, Y. Peng, and Y.-B. Cheng, *Sol. Energy* **188**, 312 (2019).
- <sup>31</sup>E. J. Juarez-Perez, Z. Hawash, S. R. Raga, L. K. Ono, and Y. Qi, *Energy Environ. Sci.* **9**(11), 3406 (2016).
- <sup>32</sup>Z. Fan, H. Xiao, Y. Wang, Z. Zhao, Z. Lin, H.-C. Cheng, S.-J. Lee, G. Wang, Z. Feng, W. A. Goddard, Y. Huang, and X. Duan, *Joule* **1**(3), 548 (2017).
- <sup>33</sup>B. Conings, J. Drijkoningen, N. Gauquelin, A. Babayigit, J. D’Haen, L. D’Olieslaeger, A. Ethirajan, J. Verbeeck, J. Manca, E. Mosconi, F. De Angelis, and H.-G. Boyen, *Adv. Energy Mater.* **5**(15), 1500477 (2015).
- <sup>34</sup>G. A. Elbaz, W. L. Ong, E. A. Doud, P. Kim, D. W. Paley, X. Roy, and J. A. Malen, *Nano Lett.* **17**(9), 5734–5739 (2017).
- <sup>35</sup>S. Thakur and A. Giri, *ACS Appl. Mater. Interfaces* **15**(22), 26755 (2023).
- <sup>36</sup>T. Haeger, R. Heiderhoff, and T. Riedl, *J. Mater. Chem. C* **8**(41), 14289 (2020).
- <sup>37</sup>A. Pisoni, J. Jacimovic, O. S. Barisic, M. Spina, R. Gaal, L. Forro, and E. Horvath, *J. Phys. Chem. Lett.* **5**(14), 2488–2492 (2014).
- <sup>38</sup>A. Giri, A. Z. Chen, A. Mattoni, K. Aryana, D. Zhang, X. Hu, S.-H. Lee, J. J. Choi, and P. E. Hopkins, *Nano Lett.* **20**(5), 3331 (2020).
- <sup>39</sup>X. Wang, W. Wang, C. Yang, D. Han, H. Fan, and J. Zhang, *J. Appl. Phys.* **130**(17), 170902 (2021).
- <sup>40</sup>A. J. Angström, *London, Edinburgh Dublin Philos. Mag. J. Sci.* **25**(166), 130 (1863).
- <sup>41</sup>W. J. Parker, R. J. Jenkins, C. P. Butler, and G. L. Abbott, *J. Appl. Phys.* **32**(9), 1679 (1961).
- <sup>42</sup>S. Sen, W. H. Konkel, S. J. Tighe, L. G. Bland, S. R. Sharma, and R. E. Taylor, *J. Cryst. Growth* **86**(1), 111 (1988).
- <sup>43</sup>R.-I. Biega, M. Bokdam, K. Herrmann, J. Mohanraj, D. Skrybeck, M. Thelakkat, M. Retsch, and L. Leppert, *J. Phys. Chem. C* **127**(19), 9183–9195 (2023).
- <sup>44</sup>M. Wolf and D. Cahen, *Sol. Cells* **27**(1), 247 (1989).
- <sup>45</sup>I SO. and BIPM OIML, *Guide to the Expression of Uncertainty in Measurement* (Aenor, 1993).
- <sup>46</sup>B. Hay, J. R. Filtz, J. Hameury, and L. Rongione, *Int. J. Thermophys.* **26**(6), 1883 (2005).
- <sup>47</sup>A. Lunev and R. Heymer, *Rev. Sci. Instrum.* **91**(6), 064902 (2020).
- <sup>48</sup>T. Baba and A. Ono, *Meas. Sci. Technol.* **12**(12), 2046 (2001).
- <sup>49</sup>K. Shinzato and T. Baba, *J. Therm. Anal. Calorim.* **64**(1), 413 (2001).
- <sup>50</sup>J. Szalapak, K. Kielbasiński, J. Krzemieński, A. Młozniak, E. Zwierkowska, M. Jakubowska, and R. Pawłowski, *Metrol. Meas. Syst.* **22**, 521 (2015).
- <sup>51</sup>Y. Zhang, A. Fan, S. Luo, H. Wang, W. Ma, and X. Zhang, *Int. J. Heat Mass Transfer* **145**, 118795 (2019).
- <sup>52</sup>A. Kusiak, J. Martan, J.-L. Battaglia, and R. Daniel, *Thermochim. Acta* **556**, 1–5 (2013).
- <sup>53</sup>A. C. Tam and H. Sontag, *Nondestructive Characterization of Materials II*, edited by J. F. Bussière, J.-P. Monchal, C. O. Ruud, and R. E. Green (Springer US, Boston, MA, 1987), p. 355.
- <sup>54</sup>J. W. MacLachlan and J. C. Murphy *et al.*, *Nondestructive Characterization of Materials II*, edited by J. F. Bussière, J.-P. Monchal, and C. O. Ruud (Springer US, Boston, MA, 1987), p. 777.
- <sup>55</sup>A. G. Bell, *Am. J. Sci.* **s3-20**, 305 (1880).
- <sup>56</sup>R. T. Swinn, *Appl. Phys. Lett.* **42**(11), 955 (1983).
- <sup>57</sup>P. Charpentier, F. Lepoutre, and L. Bertrand, *J. Appl. Phys.* **53**(1), 608 (1982).
- <sup>58</sup>O. Pessoa, Jr., C. L. Cesar, N. A. Patel, H. Vargas, C. C. Ghizoni, and L. C. M. Miranda, *J. Appl. Phys.* **59**(4), 1316 (1986).
- <sup>59</sup>A. C. Tam, *Rev. Mod. Phys.* **58**(2), 381 (1986).

- <sup>60</sup>E. L. Kerr, *Appl. Opt.* **12**(10), 2520 (1973).
- <sup>61</sup>A. Rosencwaig, *Anal. Chem.* **47**(6), 592A (1975).
- <sup>62</sup>H. K. Wickramasinghe, R. C. Bray, V. Jipson, C. F. Quate, and J. R. Salcedo, *Appl. Phys. Lett.* **33**(11), 923 (1978).
- <sup>63</sup>S. Govorkov, W. Ruderman, M. W. Horn, R. B. Goodman, and M. Rothschild, *Rev. Sci. Instrum.* **68**(10), 3828 (1997).
- <sup>64</sup>M. J. Adams and G. F. Kirkbright, *Analyst* **102**(1213), 281 (1977).
- <sup>65</sup>Y.-H. Pao, *Optoacoustic Spectroscopy and Detection* (Elsevier, 2012).
- <sup>66</sup>M. M. Farrow, R. K. Burnham, M. Auzanneau, S. L. Olsen, N. Purdie, and E. M. Eyring, *Appl. Opt.* **17**(7), 1093 (1978).
- <sup>67</sup>J. Wang, T. Liu, S. Jiao, R. Chen, Q. Zhou, K. K. Shung, L. V. Wang, and H. F. Zhang, *J. Biomed. Opt.* **15**(2), 021317 (2010).
- <sup>68</sup>G. Busse and A. Ograbeck, *J. Appl. Phys.* **51**(7), 3576 (1980).
- <sup>69</sup>C. L. Cesar, H. Vargas, and L. C. M. Miranda, *Appl. Phys. Lett.* **43**(6), 555 (1983).
- <sup>70</sup>H. Hu, X. Wang, and X. Xu, *J. Appl. Phys.* **86**(7), 3953 (1999).
- <sup>71</sup>G. Liu, *Appl. Opt.* **21**(5), 955 (1982).
- <sup>72</sup>J.-M. Heritier, *Opt. Commun.* **44**(4), 267 (1983).
- <sup>73</sup>H. M. Lai and K. Young, *J. Acoust. Soc. Am.* **72**(6), 2000 (1982).
- <sup>74</sup>V. S. Teslenko, *Sov. J. Quantum Electron.* **7**(8), 981 (1977).
- <sup>75</sup>T. J. Burkey, M. Majewski, and D. Griller, *J. Am. Chem. Soc.* **108**(9), 2218 (1986).
- <sup>76</sup>V. A. Sablikov and V. B. Sandomirskii, *Phys. Status Solidi B* **120**(2), 471 (1983).
- <sup>77</sup>R. Rosei and D. W. Lynch, *Phys. Rev. B* **5**(10), 3883 (1972).
- <sup>78</sup>E. Matatagui, A. G. Thompson, and M. Cardona, *Phys. Rev.* **176**(3), 950 (1968).
- <sup>79</sup>R. B. Wilson, B. A. Apgar, L. W. Martin, and D. G. Cahill, *Opt. Express* **20**(27), 28829 (2012).
- <sup>80</sup>K. Ujihara, *J. Appl. Phys.* **43**(5), 2376 (1972).
- <sup>81</sup>D. A. Young, C. Thomsen, H. T. Grahn, H. J. Maris, and J. Tauc, *Phonon Scattering in Condensed Matter V* (Springer, Berlin, Heidelberg, 1986).
- <sup>82</sup>C. A. Paddock and G. L. Eesley, *Opt. Lett.* **11**(5), 273 (1986).
- <sup>83</sup>D. G. Cahill, W. K. Ford, K. E. Goodson, G. D. Mahan, A. Majumdar, H. J. Maris, R. Merlin, and S. R. Phillpot, *J. Appl. Phys.* **93**(2), 793 (2003).
- <sup>84</sup>J. Liu, J. Zhu, M. Tian, X. Gu, A. Schmidt, and R. Yang, *Rev. Sci. Instrum.* **84**(3), 034902 (2013).
- <sup>85</sup>Z. Cheng, A. Weidenbach, T. Feng, M. B. Tellekamp, S. Howard, M. J. Wahila, B. Zivasatienraj, B. Foley, S. T. Pantelides, L. F. J. Piper, W. Doolittle, and S. Graham, *Phys. Rev. Mater.* **3**(2), 025002 (2019).
- <sup>86</sup>C. Chiritescu, D. G. Cahill, N. Nguyen, D. Johnson, A. Bodapati, P. Kebbinski, and P. Zschack, *Science* **315**(5810), 351 (2007).
- <sup>87</sup>P. Jiang, X. Qian, and R. Yang, *Rev. Sci. Instrum.* **88**(7), 074901 (2017).
- <sup>88</sup>P. Jiang, X. Qian, and R. Yang, *J. Appl. Phys.* **124**(16), 161103 (2018).
- <sup>89</sup>A. J. Schmidt, X. Chen, and G. Chen, *Rev. Sci. Instrum.* **79**(11), 114902 (2008).
- <sup>90</sup>T. Favaloro, J.-H. Bahk, and A. Shakouri, *Rev. Sci. Instrum.* **86**(2), 024903 (2015).
- <sup>91</sup>B. Sun and Y. K. Koh, *Rev. Sci. Instrum.* **87**(6), 064901 (2016).
- <sup>92</sup>J. Zhu, D. Tang, W. Wang, J. Liu, K. W. Holub, and R. Yang, *J. Appl. Phys.* **108**(9), 094315 (2010).
- <sup>93</sup>W. S. Capinski, H. J. Maris, T. Ruf, M. Cardona, K. Ploog, and D. S. Katzer, *Phys. Rev. B* **59**(12), 8105 (1999).
- <sup>94</sup>Y. K. Koh, D. G. Cahill, and B. Sun, *Phys. Rev. B* **90**(20), 205412 (2014).
- <sup>95</sup>R. M. Costescu, M. A. Wall, and D. G. Cahill, *Phys. Rev. B* **67**(5), 054302 (2003).
- <sup>96</sup>A. J. Schmidt, R. Cheaito, and M. Chiesa, *Rev. Sci. Instrum.* **80**(9), 094901 (2009).
- <sup>97</sup>D. G. Cahill, *Rev. Sci. Instrum.* **75**(12), 5119 (2004).
- <sup>98</sup>J. Yang, E. Ziade, and A. J. Schmidt, *Rev. Sci. Instrum.* **87**(1), 014901 (2016).
- <sup>99</sup>J. L. Braun and P. E. Hopkins, *J. Appl. Phys.* **121**(17), 175107 (2017).
- <sup>100</sup>D. G. Cahill, P. V. Braun, G. Chen, D. R. Clarke, S. Fan, K. E. Goodson, P. Kebbinski, W. P. King, G. D. Mahan, A. Majumdar, H. J. Maris, S. R. Phillpot, E. Pop, and L. Shi, *Appl. Phys. Rev.* **1**(1), 011305 (2014).
- <sup>101</sup>P. Jiang, X. Qian, and R. Yang, *Rev. Sci. Instrum.* **89**(9), 094902 (2018).
- <sup>102</sup>Z. Cheng, F. Mu, X. Ji, T. You, W. Xu, T. Suga, X. Ou, D. G. Cahill, and S. Graham, *ACS Appl. Mater. Interfaces* **13**(27), 31843 (2021).
- <sup>103</sup>D. H. Olson, J. L. Braun, and P. E. Hopkins, *J. Appl. Phys.* **126**(15), 150901 (2019).
- <sup>104</sup>J. L. Braun, D. H. Olson, J. T. Gaskins, and P. E. Hopkins, *Rev. Sci. Instrum.* **90**(2), 024905 (2019).
- <sup>105</sup>D. Rodin and S. K. Yee, *Rev. Sci. Instrum.* **88**(1), 014902 (2017).
- <sup>106</sup>K. T. Regner, D. P. Sellan, Z. Su, C. H. Amon, A. J. H. McGaughey, and J. A. Malen, *Nat. Commun.* **4**(1), 1640 (2013).
- <sup>107</sup>A. J. Minnich, J. A. Johnson, A. J. Schmidt, K. Esfarjani, M. S. Dresselhaus, K. A. Nelson, and G. Chen, *Phys. Rev. Lett.* **107**(9), 095901 (2011).
- <sup>108</sup>H. Zhang, X. Chen, Y.-D. Jho, and A. J. Minnich, *Nano Lett.* **16**(3), 1643 (2016).
- <sup>109</sup>L. Wang, R. Cheaito, J. L. Braun, A. Giri, and P. E. Hopkins, *Rev. Sci. Instrum.* **87**(9), 094902 (2016).
- <sup>110</sup>X. Qian, Z. Ding, J. Shin, A. J. Schmidt, and G. Chen, *Rev. Sci. Instrum.* **91**(6), 064903 (2020).
- <sup>111</sup>C. M. Rost, J. Braun, K. Ferri, L. Backman, A. Giri, E. J. Opila, J.-P. Maria, and P. E. Hopkins, *Appl. Phys. Lett.* **111**(15), 151902 (2017).
- <sup>112</sup>S. Li, Z. Dai, L. Li, N. P. Padture, and P. Guo, *Rev. Sci. Instrum.* **93**(5), 053003 (2022).
- <sup>113</sup>B. Li, J. Xu, C. A. Kocoj, S. Li, Y. Li, D. Chen, S. Zhang, L. Dou, and P. Guo, *J. Am. Chem. Soc.* **146**(3), 2187 (2024).
- <sup>114</sup>D. Chen, M. Fortin-Deschênes, Y. Lou, H. Lee, J. Xu, A. A. Sheikh, K. Watanabe, T. Taniguchi, Y. Xia, F. Xia, and P. Guo, *J. Phys. Chem. C* **127**(19), 9121 (2023).
- <sup>115</sup>U. Choudhry, T. Kim, M. Adams, J. Ranasinghe, R. Yang, and B. Liao, *J. Appl. Phys.* **130**(23), 231101 (2021).
- <sup>116</sup>H. J. Eichler, P. Günter, and D. W. Pohl, *Laser-Induced Dynamic Gratings* (Springer Berlin Heidelberg, Berlin, Heidelberg, 1986), p. 13.
- <sup>117</sup>H. Eichler, G. Salje, and H. Stahl, *J. Appl. Phys.* **44**(12), 5383 (1973).
- <sup>118</sup>T. S. Rose, R. Righini, and M. D. Fayer, *Chem. Phys. Lett.* **106**(1), 13 (1984).
- <sup>119</sup>Y. Bi, E. M. Hutter, Y. Fang, Q. Dong, J. Huang, and T. J. Savenije, *J. Phys. Chem. Lett.* **7**(5), 923 (2016).
- <sup>120</sup>F. Hoffmann, M. P. Short, and C. A. Dennett, *MRS Bull.* **44**(5), 392 (2019).
- <sup>121</sup>M. Fayer, *IEEE J. Quantum Electron.* **22**(8), 1437 (1986).
- <sup>122</sup>A. Harata, H. Nishimura, and T. Sawada, *Appl. Phys. Lett.* **57**(2), 132 (1990).
- <sup>123</sup>C. Li, H. Ma, T. Li, J. Dai, M. A. J. Rasel, A. Mattioni, A. Alatas, M. G. Thomas, Z. W. Rouse, A. Shragai, S. P. Baker, B. J. Ramshaw, J. P. Feser, D. B. Mitzi, and Z. Tian, *Nano Lett.* **21**(9), 3708 (2021).
- <sup>124</sup>L. Rieland, J. Wagner, R. Bernhardt, T. Wang, O. Abdul-Aziz, P. Stein, E. A. A. Pogna, S. D. Conte, G. Cerullo, H. Hedayat, and P. H. M. van Loosdrecht, *Nano Lett.* **24**, 9824 (2024).
- <sup>125</sup>P. Šćajev, R. Aleksiūnas, S. Terakawa, C. Qin, T. Fujihara, T. Matsushima, C. Adachi, and S. Juršėnas, *J. Phys. Chem. C* **123**(24), 14914 (2019).
- <sup>126</sup>O. W. Käding, H. Skurk, A. A. Maznev, and E. Matthias, *Appl. Phys. A* **61**(3), 253 (1995).
- <sup>127</sup>W. B. Jackson, N. M. Amer, A. C. Boccara, and D. Fournier, *Appl. Opt.* **20**(8), 1333 (1981).
- <sup>128</sup>A. C. Boccara, D. Fournier, and J. Badoz, *Appl. Phys. Lett.* **36**(2), 130 (1980).
- <sup>129</sup>S. Akhmanov, D. Krindach, A. Migulin, A. Sukhorukov, and R. Khokhlov, *IEEE J. Quantum Electron.* **4**(10), 568 (1968).
- <sup>130</sup>M. E. Long, R. L. Swofford, and A. C. Albrecht, *Science* **191**(4223), 183 (1976).
- <sup>131</sup>S. Sandell, E. Chávez-Ángel, A. El Sachat, J. He, C. M. S. Torres, and J. Maire, *J. Appl. Phys.* **128**(13), 131101 (2020).
- <sup>132</sup>J. D. Gupta, P. Jangra, and A. K. Mishra, in *Raman Spectroscopy: Advances and Applications*, edited by D. K. Singh, A. K. Mishra, and A. Materny (Springer Nature Singapore, Singapore, 2024), p. 75.
- <sup>133</sup>A. Özden, F. Drechsler, J. Kurtos, M. Alexe, and C. Himcinschi, *Phys. Rev. Mater.* **8**(1), 014407 (2024).
- <sup>134</sup>S. Sett, V. K. Aggarwal, A. Singha, and A. K. Raychaudhuri, *Phys. Rev. Appl.* **13**(5), 054008 (2020).
- <sup>135</sup>A. Balandin, S. Ghosh, W. Bao, I. Calizo, D. Teweldebrhan, F. Miao, and C. N. Lau, *Nano Lett.* **8**(3), 902 (2008).
- <sup>136</sup>E. Yalon, B. Aslan, K. K. H. Smithe, C. J. McClellan, S. V. Suryavanshi, F. Xiong, A. Sood, C. M. Neumann, X. Xu, K. E. Goodson, T. F. Heinz, and E. Pop, *ACS Appl. Mater. Interfaces* **9**(49), 43013 (2017).
- <sup>137</sup>Q.-Y. Li, K. Xia, J. Zhang, Y. Zhang, Q. Li, K. Takahashi, and X. Zhang, *Nanoscale* **9**(30), 10784 (2017).

- <sup>138</sup>S. Yin, W. Zhang, C. Tan, L. Chen, J. Chen, G. Li, H. Zhang, Y. Zhang, W. Wang, and L. Li, *J. Phys. Chem. C* **125**(29), 16129 (2021).
- <sup>139</sup>Q.-Y. Li, X. Zhang, and Y.-D. Hu, *Thermochim. Acta* **592**, 67 (2014).
- <sup>140</sup>M. Franko and C. D. Tran, *Encyclopedia of Analytical Chemistry* (Wiley, 2010), p. 1249.
- <sup>141</sup>A. Skumanich, D. Fournier, A. C. Boccarda, and N. M. Amer, *Appl. Phys. Lett.* **47**(4), 402 (1985).
- <sup>142</sup>D. Fournier, C. Boccarda, A. Skumanich, and N. M. Amer, *J. Appl. Phys.* **59**(3), 787 (1986).
- <sup>143</sup>D. G. Cahill, *Rev. Sci. Instrum.* **61**(2), 802 (1990).
- <sup>144</sup>D.-W. Oh, A. Jain, J. K. Eaton, K. E. Goodson, and J. S. Lee, *Int. J. Heat Fluid Flow* **29**(5), 1456 (2008).
- <sup>145</sup>D. G. Cahill, M. Katiyar, and J. R. Abelson, *Phys. Rev. B* **50**(9), 6077 (1994).
- <sup>146</sup>C. E. Raudzis, F. Schatz, and D. Wharam, *J. Appl. Phys.* **93**(10), 6050 (2003).
- <sup>147</sup>L. Peri, D. Prete, V. Demontis, E. Degoli, A. Ruini, R. Magri, and F. Rossella, *Nanotechnology* **34**(43), 435403 (2023).
- <sup>148</sup>J. Pelzl, M. Chirtoc, and R. Meckenstock, *Int. J. Thermophys.* **34**(8), 1353 (2013).
- <sup>149</sup>B. Beltrán-Pitarch, B. Guralnik, N. Lamba, A. R. Stilling-Andersen, L. Nørregaard, T. M. Hansen, O. Hansen, N. Pryds, P. F. Nielsen, and D. H. Petersen, *Mater. Today Phys.* **31**, 100963 (2023).
- <sup>150</sup>T. Liu, S. Y. Yue, S. Ratnasingham, T. Degousee, P. Varsini, J. Briscoe, M. A. McLachlan, M. Hu, and O. Fenwick, *ACS Appl. Mater. Interfaces* **11**(50), 47507 (2019).
- <sup>151</sup>C. C. Williams and H. K. Wickramasinghe, *Microelectron. Eng.* **5**(1–4), 509 (1986).
- <sup>152</sup>Y. Zhang, W. Zhu, F. Hui, M. Lanza, T. Borca-Tasciuc, and M. M. Rojo, *Adv. Funct. Mater.* **30**(18), 1900892 (2020).
- <sup>153</sup>G. Mills, H. Zhou, A. Midha, L. Donaldson, and J. M. R. Weaver, *Appl. Phys. Lett.* **72**(22), 2900 (1998).
- <sup>154</sup>I. W. Rangelow, T. Gotszalk, P. Grabiec, K. Edinger, and N. Abedinov, *Microelectron. Eng.* **57**–**58**, 737 (2001).
- <sup>155</sup>R. J. Pylkki, P. J. Moyer, P. J. Moyer, P. E. West, and P. E. West, *Jpn. J. Appl. Phys., Part 1* **33**(6S), 3785 (1994).
- <sup>156</sup>S. Lefèvre, J.-B. Saulnier, C. Fuentes, and S. Volz, *Superlattices Microstruct.* **35**(3–6), 283 (2004).
- <sup>157</sup>E. Oesterschulze, M. Stopka, L. Ackermann, W. Scholz, and S. Werner, *J. Vac. Sci. Technol. B* **14**(2), 832 (1996).
- <sup>158</sup>S. Gomès, A. Assy, and P. Chapuis, *Phys. Status Solidi A* **212**(3), 477 (2015).
- <sup>159</sup>S. Lefèvre, S. Volz, J.-B. Saulnier, C. Fuentes, and N. Trannoy, *Rev. Sci. Instrum.* **74**(4), 2418 (2003).
- <sup>160</sup>K. Luo, Z. Shi, J. Varesi, and A. Majumdar, *J. Vac. Sci. Technol. B* **15**(2), 349 (1997).
- <sup>161</sup>H. Song, J. Liu, B. Liu, J. Wu, H.-M. Cheng, and F. Kang, *Joule* **2**(3), 442 (2018).
- <sup>162</sup>W. Cai, A. L. Moore, Y. Zhu, X. Li, S. Chen, L. Shi, and R. S. Ruoff, *Nano Lett.* **10**(5), 1645 (2010).
- <sup>163</sup>I. Jo, M. T. Pettes, J. Kim, K. Watanabe, T. Taniguchi, Z. Yao, and L. Shi, *Nano Lett.* **13**(2), 550 (2013).
- <sup>164</sup>M. Fujii, X. Zhang, H. Xie, H. Ago, K. Takahashi, T. Ikuta, H. Abe, and T. Shimizu, *Phys. Rev. Lett.* **95**(6), 065502 (2005).
- <sup>165</sup>P. Kim, L. Shi, A. Majumdar, and P. L. McEuen, *Phys. Rev. Lett.* **87**(21), 215502 (2001).
- <sup>166</sup>L. Shi, D. Li, C. Yu, W. Jang, D. Kim, Z. Yao, P. Kim, and A. Majumdar, *J. Heat Transfer* **125**(5), 881 (2003).
- <sup>167</sup>D. Li, Y. Wu, P. Kim, L. Shi, P. Yang, and A. Majumdar, *Appl. Phys. Lett.* **83**(14), 2934 (2003).
- <sup>168</sup>E. Freire, in *Protein Stability and Folding: Theory and Practice*, edited by B. A. Shirley (Humana Press, Totowa, NJ, 1995), p. 191.
- <sup>169</sup>G. W. H. Höhne, W. F. Hemminger, and H.-J. Flammersheim, in *Differential Scanning Calorimetry* (Springer Berlin Heidelberg, Berlin, Heidelberg, 2003), p. 147.
- <sup>170</sup>J. R. Seibert, Ö. Keleş, J. Wang, and F. Erogboogo, *Polymer* **185**, 121988 (2019).
- <sup>171</sup>H. Chen, C. Liu, J. Xu, A. Maxwell, W. Zhou, Y. Yang, Q. Zhou, A. S. R. Bati, H. Wan, Z. Wang, L. Zeng, J. Wang, P. Serles, Y. Liu, S. Teale, Y. Liu, M. I. Saidaminov, M. Li, N. Rolston, S. Hoogland, T. Filleter, M. G. Kanatzidis, B. Chen, Z. Ning, and E. H. Sargent, *Science* **384**(6692), 189 (2024).
- <sup>172</sup>Q. Jiang and K. Zhu, *Nat. Rev. Mater.* **9**, 399–419 (2024).
- <sup>173</sup>S. D. Stranks, V. M. Burlakov, T. Leijtens, J. M. Ball, A. Goriely, and H. J. Snaith, *Phys. Rev. Appl.* **2**(3), 034007 (2014).
- <sup>174</sup>T. Leijtens, S. D. Stranks, G. E. Eperon, R. Lindblad, E. M. Johansson, I. J. McPherson, H. Rensmo, J. M. Ball, M. M. Lee, and H. J. Snaith, *ACS Nano* **8**(7), 7147 (2014).
- <sup>175</sup>S. D. Stranks, G. E. Eperon, G. Grancini, C. Menelaou, M. J. Alcocer, T. Leijtens, L. M. Herz, A. Petrozza, and H. J. Snaith, *Science* **342**(6156), 341 (2013).
- <sup>176</sup>G. Xing, N. Mathews, S. Sun, S. S. Lim, Y. M. Lam, M. Gratzel, S. Mhaisalkar, and T. C. Sum, *Science* **342**(6156), 344 (2013).
- <sup>177</sup>Q. Dong, Y. Fang, Y. Shao, P. Mulligan, J. Qiu, L. Cao, and J. Huang, *Science* **347**(6225), 967 (2015).
- <sup>178</sup>D. Shi, V. Adinolfi, R. Comin, M. Yuan, E. Alarousu, A. Buin, Y. Chen, S. Hoogland, A. Rothenberger, K. Katsiev, Y. Losovyj, X. Zhang, P. A. Dowben, O. F. Mohammed, E. H. Sargent, and O. M. Bakr, *Science* **347**(6221), 519 (2015).
- <sup>179</sup>M. Li, Y. Yang, Z. Kuang, C. Hao, S. Wang, F. Lu, Z. Liu, J. Liu, L. Zeng, Y. Cai, Y. Mao, J. Guo, H. Tian, G. Xing, Y. Cao, C. Ma, N. Wang, Q. Peng, L. Zhu, W. Huang, and J. Wang, *Nature* **630**, 631–635 (2024).
- <sup>180</sup>C. Qin, A. S. D. Sandanayaka, C. Zhao, T. Matsushima, D. Zhang, T. Fujihara, and C. Adachi, *Nature* **585**(7823), 53 (2020).
- <sup>181</sup>L. Yi, B. Hou, H. Zhao, and X. Liu, *Nature* **618**(7964), 281 (2023).
- <sup>182</sup>J. Burschka, N. Pellet, S. J. Moon, R. Humphry-Baker, P. Gao, M. K. Nazeeruddin, and M. Grätzel, *Nature* **499**(7458), 316 (2013).
- <sup>183</sup>Q. Chen, H. Zhou, Z. Hong, S. Luo, H. S. Duan, H. H. Wang, Y. Liu, G. Li, and Y. Yang, *J. Am. Chem. Soc.* **136**(2), 622 (2014).
- <sup>184</sup>L. K. Ono, S. Wang, Y. Kato, S. R. Raga, and Y. Qi, *Energy Environ. Sci.* **7**(12), 3989 (2014).
- <sup>185</sup>B. R. Sutherland, S. Hoogland, M. M. Adachi, P. Kanjanaboos, C. T. Wong, J. J. McDowell, J. Xu, O. Voznyy, Z. Ning, A. J. Houtepen, and E. H. Sargent, *Adv. Mater.* **27**(1), 53 (2015).
- <sup>186</sup>H. S. Jung, G. S. Han, N.-G. Park, and M. J. Ko, *Joule* **3**(8), 1850 (2019).
- <sup>187</sup>J. You, Z. Hong, Y. M. Yang, Q. Chen, M. Cai, T. B. Song, C. C. Chen, S. Lu, Y. Liu, H. Zhou, and Y. Yang, *ACS Nano* **8**(2), 1674 (2014).
- <sup>188</sup>M. Saliba, T. Matsui, K. Domanski, J. Y. Seo, A. Ummadisingu, S. M. Zakeeruddin, J. P. Correa-Baena, W. R. Tress, A. Abate, A. Hagfeldt, and M. Grätzel, *Science* **354**(6309), 206 (2016).
- <sup>189</sup>J. You, L. Meng, T. B. Song, T. F. Guo, Y. M. Yang, W. H. Chang, Z. Hong, H. Chen, H. Zhou, Q. Chen, Y. Liu, N. De Marco, and Y. Yang, *Nat. Nanotechnol.* **11**(1), 75 (2016).
- <sup>190</sup>Y. Lin, Y. Bai, Y. Fang, Z. Chen, S. Yang, X. Zheng, S. Tang, Y. Liu, J. Zhao, and J. Huang, *J. Phys. Chem. Lett.* **9**(3), 654 (2018).
- <sup>191</sup>G. E. Eperon, S. D. Stranks, C. Menelaou, M. B. Johnston, L. M. Herz, and H. J. Snaith, *Energy Environ. Sci.* **7**(3), 982 (2014).
- <sup>192</sup>S. H. Turren-Cruz, A. Hagfeldt, and M. Saliba, *Science* **362**(6413), 449 (2018).
- <sup>193</sup>F. Zhang and K. Zhu, *Adv. Energy Mater.* **10**(13), 1902579 (2019).
- <sup>194</sup>N. Rolston, A. D. Printz, J. M. Tracy, H. C. Weerasingham, D. Vak, L. J. Haur, A. Priyadarshi, N. Mathews, D. J. Slotcavage, M. D. McGehee, R. E. Kalan, K. Zieliński, R. L. Grimm, H. Tsai, W. Nie, A. D. Mohite, S. Gholipour, M. Saliba, M. Grätzel, and R. H. Dauskardt, *Adv. Energy Mater.* **8**(9), 1702116 (2017).
- <sup>195</sup>S. Ma, G. Yuan, Y. Zhang, N. Yang, Y. Li, and Q. Chen, *Energy Environ. Sci.* **15**(1), 13 (2022).
- <sup>196</sup>H. C. Weerasingham, Y. Dkhissi, A. D. Scully, R. A. Caruso, and Y.-B. Cheng, *Nano Energy* **18**, 118 (2015).
- <sup>197</sup>G. Grancini, C. Roldan-Carmona, I. Zimmermann, E. Mosconi, X. Lee, D. Martineau, S. Narbey, F. Oswald, F. De Angelis, M. Graetzel, and M. K. Nazeeruddin, *Nat. Commun.* **8**, 15684 (2017).
- <sup>198</sup>J. Chen and N.-G. Park, *ACS Energy Lett.* **5**(8), 2742 (2020).
- <sup>199</sup>Y. Wang, Y. Yue, X. Yang, and L. Han, *Adv. Energy Mater.* **8**(22), 1800249 (2018).
- <sup>200</sup>S. S. Shin, S. J. Lee, and S. Il Seok, *Adv. Funct. Mater.* **29**(47), 1900455 (2019).
- <sup>201</sup>Q. Jiang, R. Tirawat, R. A. Kerner, E. A. Gaulding, Y. Xian, X. Wang, J. M. Newkirk, Y. Yan, J. J. Berry, and K. Zhu, *Nature* **623**(7986), 313 (2023).
- <sup>202</sup>M. Wang and S. Lin, *Adv. Funct. Mater.* **26**(29), 5297 (2016).
- <sup>203</sup>L. Zhao, K. Roh, S. Kacmolli, K. Al Kurdi, S. Jhulki, S. Barlow, S. R. Marder, C. Gmachl, and B. P. Rand, *Adv. Mater.* **32**(25), e2000752 (2020).

- <sup>204</sup>F. Pei, N. Li, Y. Chen, X. Niu, Y. Zhang, Z. Guo, Z. Huang, H. Zai, G. Liu, Y. Zhang, Y. Bai, X. Zhang, C. Zhu, Q. Chen, Y. Li, and H. Zhou, *ACS Energy Lett.* **6**(9), 3029 (2021).
- <sup>205</sup>Y. Zhang, Z. He, J. Xiong, S. Zhan, F. Liu, M. Su, D. Wang, Y. Huang, Q. Liao, J.-r Lu, Z. Zhang, C. Yuan, J. Wang, Q. Dai, and J. Zhang, *J. Mater. Chem. A* **12**, 10369–10384 (2024).
- <sup>206</sup>R. G. Morris and J. G. Hust, *Phys. Rev.* **124**(5), 1426 (1961).
- <sup>207</sup>R. O. Carlson, G. A. Slack, and S. J. Silverman, *J. Appl. Phys.* **36**(2), 505 (1965).
- <sup>208</sup>W. Liu and M. Asheghi, *J. Heat Transfer* **128**(1), 75 (2006).
- <sup>209</sup>A. Kovalsky, L. Wang, G. T. Marek, C. Burda, and J. S. Dyck, *J. Phys. Chem. C* **121**(6), 3228–3233 (2017).
- <sup>210</sup>R. Heiderhoff, T. Haeger, N. Pourdavoud, T. Hu, M. Al-Khafaji, A. Mayer, Y. Chen, H.-C. Scheer, and T. Riedl, *J. Phys. Chem. C* **121**(51), 28306–28311 (2017).
- <sup>211</sup>R. Anufriev, J. Ordóñez-Miranda, and M. Nomura, *Phys. Rev. B* **101**(11), 115301 (2020).
- <sup>212</sup>J. Zhao, Y. Ying, H. Zeng, K. Zhao, G. Li, and W. Li, *ACS Appl. Mater. Interfaces* **15**(9), 12502 (2023).
- <sup>213</sup>Q. Chen, C. Zhang, M. Zhu, S. Liu, M. E. Siemens, S. Gu, J. Zhu, J. Shen, X. Wu, C. Liao, J. Zhang, X. Wang, and M. Xiao, *Appl. Phys. Lett.* **108**(8), 081902 (2016).
- <sup>214</sup>Z. Guo, S. J. Yoon, J. S. Manser, P. V. Kamat, and T. Luo, *J. Phys. Chem. C* **120**(12), 6394–6401 (2016).
- <sup>215</sup>G. Wang, H. Fan, Z. Chen, Y. Gao, Z. Wang, Z. Li, H. Lu, and Y. Zhou, *Adv. Sci.* **11**, e2401194 (2024).
- <sup>216</sup>T. Ye, X. Wang, X. Li, A. Q. Yan, S. Ramakrishna, and J. Xu, *J. Mater. Chem. C* **5**(5), 1255 (2017).
- <sup>217</sup>C. Ge, M. Hu, P. Wu, Q. Tan, Z. Chen, Y. Wang, J. Shi, and J. Feng, *J. Phys. Chem. C* **122**(28), 15973 (2018).
- <sup>218</sup>X. Long, Z. Pan, Z. Zhang, J. J. Urban, and H. Wang, *Appl. Phys. Lett.* **115**(7), 072104 (2019).
- <sup>219</sup>M. A. Haque, M. I. Nugraha, S. H. K. Paleti, and D. Baran, *J. Phys. Chem. C* **123**(24), 14928 (2019).
- <sup>220</sup>Y. Wang, R. Lin, P. Zhu, Q. Zheng, Q. Wang, D. Li, and J. Zhu, *Nano Lett.* **18**(5), 2772–2779 (2018).
- <sup>221</sup>C. Shen, W. Du, Z. Wu, J. Xing, S. T. Ha, Q. Shang, W. Xu, Q. Xiong, X. Liu, and Q. Zhang, *Nanoscale* **9**(24), 8281 (2017).
- <sup>222</sup>N. Peimyoo, J. Shang, W. Yang, Y. Wang, C. Cong, and T. Yu, *Nano Res.* **8**(4), 1210 (2014).
- <sup>223</sup>S. Sahoo, A. P. S. Gaur, M. Ahmadi, M. J. F. Guinel, and R. S. Katiyar, *J. Phys. Chem. C* **117**(17), 9042 (2013).
- <sup>224</sup>S. Zhou, X. Tao, and Y. Gu, *J. Phys. Chem. C* **120**(9), 4753 (2016).
- <sup>225</sup>H. Malekpour and A. A. Balandin, *J. Raman Spectrosc.* **49**, 106–120 (2018).
- <sup>226</sup>X. Li, K. Maute, M. L. Dunn, and R. Yang, *Phys. Rev. B* **81**(24), 245318 (2010).
- <sup>227</sup>X. Qian, X. Gu, and R. Yang, *J. Phys. Chem. C* **119**(51), 28300 (2015).
- <sup>228</sup>A. Giri, S. Thakur, and A. Mattoni, *Chem. Mater.* **34**(21), 9569 (2022).
- <sup>229</sup>S. G. Volz and G. Chen, *Phys. Rev. B* **61**(4), 2651 (2000).
- <sup>230</sup>A. J. C. Ladd, B. Moran, and W. G. Hoover, *Phys. Rev. B* **34**(8), 5058 (1986).
- <sup>231</sup>X. Qian, X. Gu, and R. Yang, *Appl. Phys. Lett.* **108**(6), 063902 (2016).
- <sup>232</sup>J. Kang and L.-W. Wang, *Phys. Rev. B* **96**(2), 020302(R) (2017).
- <sup>233</sup>S.-Y. Yue, X. Zhang, G. Qin, J. Yang, and M. Hu, *Phys. Rev. B* **94**(11), 115427 (2016).
- <sup>234</sup>L. D. Whalley, J. M. Skelton, J. M. Frost, and A. Walsh, *Phys. Rev. B* **94**(22), 220301(R) (2016).
- <sup>235</sup>W. Lee, H. Li, A. B. Wong, D. Zhang, M. Lai, Y. Yu, Q. Kong, E. Lin, J. J. Urban, J. C. Grossman, and P. Yang, *Proc. Natl. Acad. Sci. U. S. A.* **114**(33), 8693 (2017).
- <sup>236</sup>T. Haeger, M. Wilmes, R. Heiderhoff, and T. Riedl, *J. Phys. Chem. Lett.* **10**(11), 3019 (2019).
- <sup>237</sup>T. Haeger, M. Ketteler, J. Bahr, N. Pourdavoud, M. Runkel, R. Heiderhoff, and T. Riedl, *J. Phys. Mater.* **3**(2), 024004 (2020).
- <sup>238</sup>Z. Hu, L. Aigouy, Z. Chen, and D. Fournier, *J. Appl. Phys.* **127**(12), 125113 (2020).
- <sup>239</sup>F. Qian, M. Hu, J. Gong, C. Ge, Y. Zhou, J. Guo, M. Chen, Z. Ge, N. P. Padture, Y. Zhou, and J. Feng, *J. Phys. Chem. C* **124**(22), 11749 (2020).
- <sup>240</sup>Y. Zhang, Q. Yao, J. Qian, X. Zhao, D. Li, and Q. Mi, *Chem. Phys. Lett.* **754**, 137637 (2020).
- <sup>241</sup>H. Xie, S. Hao, J. Bao, T. J. Slade, G. J. Snyder, C. Wolverton, and M. G. Kanatzidis, *J. Am. Chem. Soc.* **142**(20), 9553 (2020).
- <sup>242</sup>A. Mandal, S. Goswami, S. Das, D. Swain, and K. Biswas, *Angew. Chem., Int. Ed.* **63**, e202406616 (2024).
- <sup>243</sup>T. Zhu, Y. Liu, C. Fu, J. P. Heremans, J. G. Snyder, and X. Zhao, *Adv. Mater.* **29**(14), 1605884 (2017).
- <sup>244</sup>X. Huang, M. Roushan, T. J. Emge, W. Bi, S. Thiagarajan, J.-H. Cheng, R. Yang, and J. Li, *Angew. Chem., Int. Ed.* **48**(42), 7871 (2009).
- <sup>245</sup>K. J. Erickson, F. Léonard, V. Stavila, M. E. Foster, C. D. Spataru, R. E. Jones, B. M. Foley, P. E. Hopkins, M. D. Allendorf, and A. A. Talin, *Adv. Mater.* **27**(22), 3453 (2015).
- <sup>246</sup>Y.-R. Luo, *Comprehensive Handbook of Chemical Bond Energies* (2007).
- <sup>247</sup>E. Isotta, W. Peng, A. Balodhi, and A. Zevalkink, *Angew. Chem., Int. Ed.* **62**(12), e202213649 (2023).
- <sup>248</sup>Z. Fan, H. Wang, Y. Wu, X. J. Liu, and Z. P. Lu, *RSC Adv.* **6**(57), 52164 (2016).
- <sup>249</sup>X. Yan, L. Constantin, Y. Lu, J. Silvain, M. Nastasi, and B. Cui, *J. Am. Ceram. Soc.* **101**(10), 4486 (2018).
- <sup>250</sup>J. Cai, J. Yang, G. Liu, H. Wang, F. Shi, X. Tan, Z. Ge, and J. Jiang, *Mater. Today Phys.* **18**, 100394 (2021).
- <sup>251</sup>J. Callaway, *Phys. Rev.* **113**(4), 1046 (1959).
- <sup>252</sup>W. R. Thurber and A. J. H. Mante, *Phys. Rev.* **139**(5A), A1655 (1965).
- <sup>253</sup>J. S. Tse and M. A. White, *J. Phys. Chem.* **92**(17), 5006 (2002).
- <sup>254</sup>Y. Bouyrie, C. Candolfi, S. Pailhes, M. M. Koza, B. Malaman, A. Dauscher, J. Tobola, O. Boisron, L. Saviot, and B. Lenoir, *Phys. Chem. Chem. Phys.* **17**(30), 19751 (2015).
- <sup>255</sup>P. Acharyya, T. Ghosh, K. Pal, K. Kundu, K. S. Rana, J. Pandey, A. Soni, U. V. Waghmare, and K. Biswas, *J. Am. Chem. Soc.* **142**(36), 15595 (2020).
- <sup>256</sup>M. A. J. Rasel, A. Giri, D. H. Olson, C. Ni, P. E. Hopkins, and J. P. Feser, *ACS Appl. Mater. Interfaces* **12**(48), 53705–53711 (2020).
- <sup>257</sup>S. Thakur, Z. Dai, P. Karna, N. P. Padture, and A. Giri, *Mater. Horiz.* **9**(12), 3087–3094 (2022).
- <sup>258</sup>N. S. Dahod, W. Paritmongkol, and W. A. Tisdale, “Efficient thermal transport across molecular chains in hybrid 2D lead bromide perovskites,” *arXiv:2303.17397* (2023).
- <sup>259</sup>A. Negi, L. Yan, C. Yang, Y. Yu, D. Kim, S. Mukherjee, A. H. Comstock, S. Raza, Z. Wang, D. Sun, H. Ade, Q. Tu, W. You, and J. Liu, *ACS Nano* **18**(22), 14218–14230 (2024).
- <sup>260</sup>A. D. Christodoulides, P. Guo, L. Dai, J. M. Hoffman, X. Li, X. Zuo, D. Rosenmann, A. Brumberg, M. G. Kanatzidis, R. D. Schaller, and J. A. Malen, *ACS Nano* **15**(3), 4165 (2021).
- <sup>261</sup>P. Guo, C. C. Stoumpos, L. Mao, S. Sadasivam, J. B. Ketterson, P. Darancet, M. G. Kanatzidis, and R. D. Schaller, *Nat. Commun.* **9**(1), 2019 (2018).
- <sup>262</sup>Y.-H. Wang, C.-H. Yeh, I.-T. Hsieh, P.-Y. Yang, Y.-W. Hsiao, H.-T. Wu, C.-W. Pao, and C.-F. Shih, *Nanomaterials* **14**(5), 446 (2024).
- <sup>263</sup>M. N. Luckyanova, J. Garg, K. Esfarjani, A. Jandl, M. T. Bulsara, A. J. Schmidt, A. J. Minnich, S. Chen, M. S. Dresselhaus, Z. Ren, E. A. Fitzgerald, and G. Chen, *Science* **338**(6109), 936 (2012).
- <sup>264</sup>G. Chen and M. Neagu, *Appl. Phys. Lett.* **71**(19), 2761 (1997).
- <sup>265</sup>B. Yang and G. Chen, *Phys. Rev. B* **67**(19), 195311 (2003).
- <sup>266</sup>W.-L. Ong, S. Majumdar, J. A. Malen, and A. J. H. McGaughey, *J. Phys. Chem. C* **118**(14), 7288 (2014).
- <sup>267</sup>M. D. Losego, M. E. Grady, N. R. Sottos, D. G. Cahill, and P. V. Braun, *Nat. Mater.* **11**(6), 502 (2012).
- <sup>268</sup>Z. Wang, J. A. Carter, A. Lagutchev, Y. Kan Koh, N.-H. Seong, D. G. Cahill, and D. D. Drillon, *Science* **317**(5839), 787 (2007).
- <sup>269</sup>M. Cao, Y. Damji, C. Zhang, L. Wu, Q. Zhong, P. Li, D. Yang, Y. Xu, and Q. Zhang, *Small Methods* **4**(12), 2000303 (2020).
- <sup>270</sup>D. H. Cao, C. C. Stoumpos, O. K. Farha, J. T. Hupp, and M. G. Kanatzidis, *J. Am. Chem. Soc.* **137**(24), 7843 (2015).
- <sup>271</sup>H. Tsai, W. Nie, J.-C. Blancon, C. C. Stoumpos, R. Asadpour, B. Harutyunyan, A. J. Neukirch, R. Verduzco, J. J. Crochet, S. Tretiak, L. Pedesseau, J. Even, M. A. Alam, G. Gupta, J. Lou, P. M. Ajayan, M. J. Bedzyk, M. G. Kanatzidis, and A. D. Mohite, *Nature* **536**(7616), 312 (2016).

- <sup>272</sup>M. Shao, T. Bie, L. Yang, Y. Gao, X. Jin, F. He, N. Zheng, Y. Yu, and X. Zhang, *Adv. Mater.* **34**(1), 2107211 (2022).
- <sup>273</sup>M. A. Green, E. D. Dunlop, M. Yoshita, N. Kopidakis, K. Bothe, G. Siefer, and X. Hao, *Prog. Photovoltaics* **31**(7), 651 (2023).
- <sup>274</sup>I. C. Smith, E. T. Hoke, D. Solis-Ibarra, M. D. McGehee, and H. I. Karunadasa, *Angew. Chem., Int. Ed.* **53**(42), 11232 (2014).
- <sup>275</sup>L. Etgar, *Energy Environ. Sci.* **11**(2), 234 (2018).
- <sup>276</sup>M. M. Elsenety, M. Antoniadou, N. Balis, A. Kaltzoglou, L. Sygellou, A. Stergiou, N. Tagmatarchis, and P. Falaras, *ACS Appl. Energy Mater.* **3**(3), 2465 (2020).
- <sup>277</sup>A. Krishna, S. Gottis, M. Khaja Nazeeruddin, and F. Sauvage, *Adv. Funct. Mater.* **29**(8), 1806482 (2019).
- <sup>278</sup>A. H. Proppe, A. Johnston, S. Teale, A. Mahata, R. Quintero-Bermudez, E. H. Jung, L. Grater, T. Cui, T. Filletter, C.-Y. Kim, S. O. Kelley, F. De Angelis, and E. H. Sargent, *Nat. Commun.* **12**(1), 3472 (2021).
- <sup>279</sup>T. Duan, S. You, M. Chen, W. Yu, Y. Li, P. Guo, J. J. Berry, J. M. Luther, K. Zhu, and Y. Zhou, *Science* **384**(6698), 878 (2024).
- <sup>280</sup>P. Liu, S. Yu, and S. Xiao, *Sustainable Energy Fuels* **5**(16), 3950–3978 (2021).
- <sup>281</sup>B. Saparov and D. B. Mitzi, *Chem. Rev.* **116**(7), 4558 (2016).
- <sup>282</sup>D. B. Straus and C. R. Kagan, *J. Phys. Chem. Lett.* **9**(6), 1434 (2018).
- <sup>283</sup>C. Katan, N. Mercier, and J. Even, *Chem. Rev.* **119**(5), 3140 (2019).
- <sup>284</sup>H. Wang and D. H. Kim, *Chem. Soc. Rev.* **46**(17), 5204 (2017).
- <sup>285</sup>J. Byun, H. Cho, C. Wolf, M. Jang, A. Sadhanala, R. H. Friend, H. Yang, and T.-W. Lee, *Adv. Mater.* **28**(34), 7515 (2016).
- <sup>286</sup>C. Qin, T. Matsushima, W. J. Potsavage, Jr., A. S. D. Sandanayaka, M. R. Leyden, F. Bencheikh, K. Goushi, F. Mathevet, B. Heinrich, G. Yumoto, Y. Kanemitsu, and C. Adachi, *Nat. Photonics* **14**(2), 70 (2020).
- <sup>287</sup>J. Xing, Y. Zhao, M. Askerka, L. N. Quan, X. Gong, W. Zhao, J. Zhao, H. Tan, G. Long, L. Gao, Z. Yang, O. Voznyy, J. Tang, Z.-H. Lu, Q. Xiong, and E. H. Sargent, *Nat. Commun.* **9**(1), 3541 (2018).
- <sup>288</sup>S.-N. Hsu, W. Zhao, Y. Gao, Akriti, M. Segovia, X. Xu, B. W. Boudouris, and L. Dou, *Nano Lett.* **21**(18), 7839 (2021).
- <sup>289</sup>X. Li, J. M. Hoffman, and M. G. Kanatzidis, *Chem. Rev.* **121**(4), 2230 (2021).
- <sup>290</sup>L. Mao, C. C. Stoumpos, and M. G. Kanatzidis, *J. Am. Chem. Soc.* **141**(3), 1171–1190 (2019).
- <sup>291</sup>C. C. Stoumpos, D. H. Cao, D. J. Clark, J. Young, J. M. Rondinelli, J. I. Jang, J. T. Hupp, and M. G. Kanatzidis, *Chem. Mater.* **28**(8), 2852 (2016).
- <sup>292</sup>H. Wang, Q. Wang, M. Ning, S. Li, R. Xue, P. Chen, and Z. Li, *RSC Adv.* **13**(33), 22886 (2023).
- <sup>293</sup>S. Wang, J. Ma, W. Li, J. Wang, H. Wang, H. Shen, J. Li, J. Wang, H. Luo, and D. Li, *J. Phys. Chem. Lett.* **10**(10), 2546 (2019).
- <sup>294</sup>J. Yang, X. Wen, H. Xia, R. Sheng, Q. Ma, J. Kim, P. Tapping, T. Harada, T. W. Kee, F. Huang, Y.-B. Cheng, M. Green, A. Ho-Baillie, S. Huang, S. Shrestha, R. Patterson, and G. Conibeer, *Nat. Commun.* **8**(1), 14120 (2017).
- <sup>295</sup>C. Pipitone, S. Boldrini, A. Ferrario, G. Garcia-Espejo, A. Guagliardi, N. Masciocchi, A. Martorana, and F. Giannici, *Appl. Phys. Lett.* **119**(10), 101104 (2021).
- <sup>296</sup>C. J. Glassbrenner and G. A. Slack, *Phys. Rev.* **134**(4A), A1058 (1964).
- <sup>297</sup>A. V. Inyushkin, *J. Appl. Phys.* **134**(22), 221102 (2023).
- <sup>298</sup>N. A. Akil and S.-D. Guo, *J. Electron. Mater.* **52**(5), 3401 (2023).
- <sup>299</sup>C. M. Mauck, A. France-Lanord, A. C. H. Oendra, N. S. Dahod, J. C. Grossman, and W. A. Tisdale, *J. Phys. Chem. C* **123**(45), 27904–27916 (2019).
- <sup>300</sup>H. Ma, C. Li, Y. Ma, H. Wang, Z. W. Rouse, Z. Zhang, C. Slebodnick, A. Alatas, S. P. Baker, J. J. Urban, and Z. Tian, *Phys. Rev. Lett.* **123**(15), 155901 (2019).
- <sup>301</sup>M. A. Haque, S. Kee, D. R. Villalva, W.-L. Ong, and D. Baran, *Adv. Sci.* **7**(10), 1903389 (2020).
- <sup>302</sup>P. E. Hopkins and E. S. Piekos, *Appl. Phys. Lett.* **94**(18), 181901 (2009).
- <sup>303</sup>N. S. Dahod, A. France-Lanord, W. Paritmongkol, J. C. Grossman, and W. A. Tisdale, *J. Chem. Phys.* **153**(4), 044710 (2020).
- <sup>304</sup>S. Majumdar, J. A. Sierra-Suarez, S. N. Schiffrés, W.-L. Ong, C. F. Higgs III, A. J. H. McGaughey, and J. A. Malen, *Nano Lett.* **15**(5), 2985 (2015).
- <sup>305</sup>A. Giri, J.-P. Niemelä, T. Tynell, J. T. Gaskins, B. F. Donovan, M. Karppinen, and P. E. Hopkins, *Phys. Rev. B* **93**(11), 115310 (2016).
- <sup>306</sup>A. Giri, J.-P. Niemelä, C. J. Szwejkowski, M. Karppinen, and P. E. Hopkins, *Phys. Rev. B* **93**(2), 024201 (2016).
- <sup>307</sup>A. Giri, S. W. King, W. A. Lanford, A. B. Mei, D. Merrill, L. Li, R. Oviedo, J. Richards, D. H. Olson, J. L. Braun, J. T. Gaskins, F. Deangelis, A. Henry, and P. E. Hopkins, *Adv. Mater.* **30**(44), 1804097 (2018).
- <sup>308</sup>G. Chen, *Phys. Rev. B* **57**(23), 14958 (1998).
- <sup>309</sup>S. Yu, P. Liu, and S. Xiao, *J. Mater. Sci.* **56**(20), 11656 (2021).
- <sup>310</sup>A. Gold-Parker, P. M. Gehring, J. M. Skelton, I. C. Smith, D. Parshall, J. M. Frost, H. I. Karunadasa, A. Walsh, and M. F. Toney, *Proc. Natl. Acad. Sci. U. S. A.* **115**(47), 11905 (2018).
- <sup>311</sup>P.-A. Mante, C. C. Stoumpos, M. G. Kanatzidis, and A. Yartsev, *Nat. Commun.* **8**(1), 14398 (2017).
- <sup>312</sup>D. König, K. Casalenuovo, Y. Takeda, G. Conibeer, J. F. Guillemoles, R. Patterson, L. M. Huang, and M. A. Green, *Physica E* **42**(10), 2862 (2010).
- <sup>313</sup>P. Maity, J. Yin, B. Cheng, J. H. He, O. M. Bakr, and O. F. Mohammed, *J. Phys. Chem. Lett.* **10**(17), 5259 (2019).
- <sup>314</sup>M. V. Simkin and G. D. Mahan, *Phys. Rev. Lett.* **84**(5), 927 (2000).
- <sup>315</sup>S.-I. Tamura, Y. Tanaka, and H. J. Maris, *Phys. Rev. B* **60**(4), 2627 (1999).
- <sup>316</sup>M.-L. Lin, B. Dhanabalan, G. Biffi, Y.-C. Leng, S. Kutkan, M. P. Arciniegas, P.-H. Tan, and R. Krahne, *Small* **18**(15), 2106759 (2022).
- <sup>317</sup>A. Bartels, T. Dekorsy, H. Kurz, and K. Köhler, *Phys. Rev. Lett.* **82**(5), 1044 (1999).
- <sup>318</sup>C. Colvard, R. Merlin, M. V. Klein, and A. C. Gossard, *Phys. Rev. Lett.* **45**(4), 298 (1980).
- <sup>319</sup>A. S. Barker, Jr., J. L. Merz, and A. C. Gossard, *Phys. Rev. B* **17**(8), 3181 (1978).
- <sup>320</sup>H. Jang, J. D. Wood, C. R. Ryder, M. C. Hersam, and D. G. Cahill, *Adv. Mater.* **27**(48), 8017 (2015).
- <sup>321</sup>P. Jiang, X. Qian, R. Yang, and L. Lindsay, *Phys. Rev. Mater.* **2**(6), 064005 (2018).
- <sup>322</sup>J. Liu, G.-M. Choi, and D. G. Cahill, *J. Appl. Phys.* **116**(23), 233107 (2014).
- <sup>323</sup>P. Jiang, X. Qian, X. Gu, and R. Yang, *Adv. Mater.* **29**(36), 1701068 (2017).
- <sup>324</sup>X. Zhao, T. Liu, and Y.-L. Loo, *Adv. Mater.* **34**(3), 2105849 (2022).
- <sup>325</sup>A. Maiti, K. Agarwal, S. Gonzalez-Munoz, and O. V. Kolosov, *Phys. Rev. Mater.* **7**(2), 023801 (2023).
- <sup>326</sup>R. McKinney, P. Gorai, E. S. Toberer, and V. Stevanović, *Chem. Mater.* **31**(6), 2048 (2019).
- <sup>327</sup>P. Acharyya, T. Ghosh, K. Pal, K. S. Rana, M. Dutta, D. Swain, M. Etter, A. Soni, U. V. Waghmare, and K. Biswas, *Nat. Commun.* **13**(1), 5053 (2022).
- <sup>328</sup>D. G. Billing and A. Lemmerer, *Acta Crystallogr., Sect. B* **63**(5), 735 (2007).
- <sup>329</sup>G. S. Nolas and H. J. Goldsmid, in *Thermal Conductivity: Theory, Properties, and Applications* (Springer, 2004), p. 105.
- <sup>330</sup>S. Tiwari, *Compound Semiconductor Device Physics* (Academic Press, 2013).
- <sup>331</sup>H. R. Shanks, P. D. Maycock, P. H. Sidles, and G. C. Danielson, *Phys. Rev. 130*(5), 1743 (1963).
- <sup>332</sup>S. Yuan, J. Deng, H. Xiong, W. Wu, Z. Ma, M. Wang, W. Li, and J. Fan, *J. Mater. Chem. A* **11**(36), 19685 (2023).
- <sup>333</sup>J. Li, Q. Yu, Y. He, C. C. Stoumpos, G. Niu, G. G. Trimarchi, H. Guo, G. Dong, D. Wang, L. Wang, and M. G. Kanatzidis, *J. Am. Chem. Soc.* **140**(35), 11085–11090 (2018).
- <sup>334</sup>J. J. Alvarado, O. Zelaya-Angel, F. Sánchez-Sinencio, G. Torres-Delgado, H. Vargas, and J. González-Hernández, *J. Appl. Phys.* **76**(11), 7217 (1994).
- <sup>335</sup>A. D. McConnell, S. Uma, and K. E. Goodson, *J. Microelectromech. Syst.* **10**, 360–369 (2001).
- <sup>336</sup>O. Madelung, in *Semiconductors: Data Handbook*, edited by O. Madelung (Springer Berlin Heidelberg, Berlin, Heidelberg, 2004), p. 173.
- <sup>337</sup>O. Madelung, in *Semiconductors: Data Handbook*, edited by O. Madelung (Springer Berlin Heidelberg, Berlin, Heidelberg, 2004), p. 71.
- <sup>338</sup>S. Mei and I. Knezevic, *J. Appl. Phys.* **118**(17), 175101 (2015).
- <sup>339</sup>W.-Y. Lee, J.-H. Lee, J.-Y. Ahn, T.-H. Park, N.-W. Park, G.-S. Kim, J.-S. Park, and S.-K. Lee, *Nanotechnology* **28**(10), 105401 (2017).
- <sup>340</sup>J. Li, L. Wei, Z. Ti, L. Ma, Y. Yan, G. Zhang, and P.-F. Liu, *Phys. Rev. B* **108**(22), 224302 (2023).
- <sup>341</sup>M. Parashar, R. Singh, K. Yoo, and J.-J. Lee, *ACS Appl. Energy Mater.* **4**(3), 2751 (2021).
- <sup>342</sup>Y. Hu, T. Qiu, F. Bai, W. Ruan, and S. Zhang, *Adv. Energy Mater.* **8**(19), 1703620 (2018).
- <sup>343</sup>Z. Zhang, X. Li, X. Xia, Z. Wang, Z. Huang, B. Lei, and Y. Gao, *J. Phys. Chem. Lett.* **8**(17), 4300 (2017).

- <sup>344</sup>M. Kong, H. Hu, L. Wan, M. Chen, Y. Gan, J. Wang, F. Chen, B. Dong, D. Eder, and S. Wang, *RSC Adv.* **7**(56), 35549 (2017).
- <sup>345</sup>G. Xiang, Y. Wu, M. Zhang, C. Cheng, J. Leng, and H. Ma, *Nanomaterials* **11**(10), 2712 (2021).
- <sup>346</sup>K. M. McCall, C. C. Stoumpos, O. Y. Kontsevoi, G. C. B. Alexander, B. W. Wessels, and M. G. Kanatzidis, *Chem. Mater.* **31**(7), 2644 (2019).
- <sup>347</sup>A. J. Lehner, D. H. Fabini, H. A. Evans, C.-A. Hébert, S. R. Smock, J. Hu, H. Wang, J. W. Zwanziger, M. L. Chabiny, and R. Seshadri, *Chem. Mater.* **27**(20), 7137 (2015).
- <sup>348</sup>P. Acharyya, K. Pal, A. Ahad, D. Sarkar, K. S. Rana, M. Dutta, A. Soni, U. V. Waghmare, and K. Biswas, *Adv. Funct. Mater.* **33**(41), 2304607 (2023).
- <sup>349</sup>B.-W. Park, B. Philippe, X. Zhang, H. Rensmo, G. Boschloo, and E. M. J. Johansson, *Adv. Mater.* **27**(43), 6806 (2015).
- <sup>350</sup>M. A. Haque, A. N. Gandi, R. Mohanraman, Y. Weng, B. Davaasuren, A.-H. Emwas, C. Combe, D. Baran, A. Rothenberger, U. Schwingenschlögl, H. N. Alshareef, S. Dong, and T. Wu, *Adv. Funct. Mater.* **29**(13), 1809166 (2019).
- <sup>351</sup>A. C. Ferreira, A. Letoublon, S. Paofai, S. Raymond, C. Ecolivet, B. Ruffle, S. Cordier, C. Katan, M. I. Saidaminov, A. A. Zhumekenov, O. M. Bakr, J. Even, and P. Bourges, *Phys. Rev. Lett.* **121**(8), 085502 (2018).
- <sup>352</sup>I. P. Swainson, M. G. Tucker, D. J. Wilson, B. Winkler, and V. Milman, *Chem. Mater.* **19**(10), 2401 (2007).
- <sup>353</sup>B. Li, Y. Kawakita, Y. Liu, M. Wang, M. Matsuuura, K. Shibata, S. Ohira-Kawamura, T. Yamada, S. Lin, K. Nakajima, and S. F. Liu, *Nat. Commun.* **8**, 16086 (2017).
- <sup>354</sup>L. N. Quan, Y. Park, P. Guo, M. Gao, J. Jin, J. Huang, J. K. Copper, A. Schwartzberg, R. Schaller, D. T. Limmer, and P. Yang, *Proc. Natl. Acad. Sci. U.S.A.* **118**(25), e2104425118 (2021).
- <sup>355</sup>C. Yang, S. Raza, X. Li, and J. Liu, *J. Phys. Chem. B* **127**(30), 6804 (2023).
- <sup>356</sup>Q. Tu, D. Kim, M. Shyik, and M. G. Kanatzidis, *Matter* **4**(9), 2765 (2021).
- <sup>357</sup>D. G. Cahill, S. K. Watson, and R. O. Pohl, *Phys. Rev. B* **46**(10), 6131 (1992).
- <sup>358</sup>A. Giri and P. E. Hopkins, *Adv. Funct. Mater.* **30**(8), 1903857 (2020).
- <sup>359</sup>Z. Xu, *Theor. Appl. Mech. Lett.* **6**(3), 113 (2016).
- <sup>360</sup>R. Hanus, M. T. Agne, A. J. E. Rettie, Z. Chen, G. Tan, D. Y. Chung, M. G. Kanatzidis, Y. Pei, P. W. Voorhees, and G. J. Snyder, *Adv. Mater.* **31**, 1900108 (2019).
- <sup>361</sup>Q. Tu, I. Spanopoulos, E. S. Vasileiadou, X. Li, M. G. Kanatzidis, G. S. Shekhawat, and V. P. Dravid, *ACS Appl. Mater. Interfaces* **12**(18), 20440 (2020).
- <sup>362</sup>H. Gao, W. Wei, L. Li, Y. Tan, and Y. Tang, *J. Phys. Chem. C* **124**(35), 19204 (2020).
- <sup>363</sup>G. A. Slack and S. Galginaitis, *Phys. Rev.* **133**(1A), A253 (1964).
- <sup>364</sup>C.-H. Su, *AIP Adv.* **5**, 057118 (2015).
- <sup>365</sup>J. J. Alvarado-Gil, O. Zelaya-Angel, H. Vargas, and J. L. Lucio M., *Phys. Rev. B* **50**(19), 14627 (1994).
- <sup>366</sup>R. Castro-Rodríguez, M. Zapata-Torres, V. Rejón Moo, P. Bartolo-Pérez, and J. L. Peña, *J. Phys. D* **32**(11), 1194 (1999).
- <sup>367</sup>G. Conibeer, *Mater. Today* **10**(11), 42 (2007).
- <sup>368</sup>S. H. Im, H.-J. Kim, S. W. Kim, S.-W. Kim, and S. Il Seok, *Energy Environ. Sci.* **4**(10), 4181 (2011).
- <sup>369</sup>G. I. Koleilat, L. Levina, H. Shukla, S. H. Myrskog, S. Hinds, A. G. Pattantyus-Abraham, and E. H. Sargent, *ACS Nano* **2**(5), 833 (2008).
- <sup>370</sup>J. H. Bang and P. V. Kamat, *ACS Nano* **3**(6), 1467 (2009).
- <sup>371</sup>J. Yang and X. Zhong, *J. Mater. Chem. A* **4**(42), 16553 (2016).
- <sup>372</sup>K. S. Leschkies, R. Divakar, J. Basu, E. Enache-Pommier, J. E. Boercker, C. B. Carter, U. R. Kortshagen, D. J. Norris, and E. S. Aydil, *Nano Lett.* **7**(6), 1793 (2007).
- <sup>373</sup>F. Huang, L. Zhang, Q. Zhang, J. Hou, H. Wang, H. Wang, S. Peng, J. Liu, and G. Cao, *ACS Appl. Mater. Interfaces* **8**(50), 34482 (2016).
- <sup>374</sup>R. K. Sonker, R. Shastri, and R. Johari, *Energy Fuels* **35**(9), 8430 (2021).
- <sup>375</sup>M. Panachikool and T. Pandiyarajan, *Carbon Lett.* **34**(1), 445 (2024).
- <sup>376</sup>M. Li, W. Ni, B. Kan, X. Wan, L. Zhang, Q. Zhang, G. Long, Y. Zuo, and Y. Chen, *Phys. Chem. Chem. Phys.* **15**(43), 18973 (2013).
- <sup>377</sup>M. Bacon, S. J. Bradley, and T. Nann, *Part. Part. Syst. Charact.* **31**(4), 415 (2014).
- <sup>378</sup>A. Kim, J. K. Dash, P. Kumar, and R. Patel, *ACS Appl. Electron. Mater.* **4**(1), 27 (2022).
- <sup>379</sup>P. Guyot-Sionnest, M. Shim, C. Matranga, and M. Hines, *Phys. Rev. B* **60**(4), R2181 (1999).
- <sup>380</sup>V. I. Klimov, A. A. Mikhailovsky, D. W. McBranch, C. A. Leatherdale, and M. G. Bawendi, *Phys. Rev. B* **61**(20), R13349 (2000).
- <sup>381</sup>D. V. Talapin and J. Steckel, *MRS Bull.* **38**(9), 685 (2013).
- <sup>382</sup>A. L. Moore and L. Shi, *Mater. Today* **17**(4), 163 (2014).
- <sup>383</sup>Y. Gao, B. Li, X. Liu, H. Shen, Y. Song, J. Song, Z. Yan, X. Yan, Y. Chong, R. Yao, S. Wang, L. S. Li, F. Fan, and Z. Du, *Nat. Nanotechnol.* **18**(10), 1168 (2023).
- <sup>384</sup>M. I. Nugraha, I. Indriyati, I. Primadona, M. Gedda, G. E. Timuda, F. Iskandar, and T. D. Anthopoulos, *Adv. Mater.* **35**(38), 2210683 (2023).
- <sup>385</sup>A. Khalid, K. Easawi, S. Abdallah, M. G. El-Shaarawy, S. Negm, and H. Talaat, *IOP Conf. Ser.* **762**(1), 012007 (2020).
- <sup>386</sup>Z. El-Qahtani, A. Badawi, K. Easawi, N. Al-Hosiny, and S. Abdallah, *Mater. Sci. Semicond. Process.* **20**, 68–73 (2014).
- <sup>387</sup>N. Al-Hosiny, A. Badawi, M. A. A. Moussa, R. El Agmy, and S. Abdallah, *Int. J. Nanopart.* **5**(3), 258 (2012).
- <sup>388</sup>N. K. Mahanta and A. R. Abramson, paper presented at the 13th InterSociety Conference on Thermal and Thermomechanical Phenomena in Electronic Systems, 2002.
- <sup>389</sup>M. Liu, Y. Ma, and R. Y. Wang, *ACS Nano* **9**(12), 12079–12087 (2015).
- <sup>390</sup>W.-L. Ong, S. M. Rupich, D. V. Talapin, A. J. H. McGaughey, and J. A. Malen, *Nat. Mater.* **12**(5), 410–415 (2013).
- <sup>391</sup>J. P. Feser, E. M. Chan, A. Majumdar, R. A. Segelman, and J. J. Urban, *Nano Lett.* **13**(5), 2122 (2013).
- <sup>392</sup>B. T. Diroll, P. Guo, and R. D. Schaller, *Nano Lett.* **18**(12), 7863 (2018).
- <sup>393</sup>B. T. Diroll and R. D. Schaller, *Nanoscale* **11**(17), 8204 (2019).
- <sup>394</sup>M. Piotrowski, M. Franco, V. Sousa, J. Rodrigues, F. L. Deepak, Y. Kakefuda, N. Kawamoto, T. Baba, B. Owens-Baird, P. Alpuim, K. Kovnir, T. Mori, and Y. V. Kolen'ko, *J. Phys. Chem. C* **122**(48), 27127 (2018).
- <sup>395</sup>K. Gu, H. Wu, J. Su, P. Sun, P.-H. Tan, and H. Zhong, *Nano Lett.* **24**(13), 4038 (2024).
- <sup>396</sup>Z. Wang, A. D. Christodoulides, L. Dai, Y. Zhou, R. Dai, Y. Xu, Q. Nian, J. Wang, J. A. Malen, and R. Y. Wang, *Nano Lett.* **22**(12), 4669 (2022).
- <sup>397</sup>Y. Liang, B. T. Diroll, K.-L. Wong, S. M. Harvey, M. Wasielewski, W.-L. Ong, R. D. Schaller, and J. A. Malen, *Nano Lett.* **23**(9), 3687–3693 (2023).
- <sup>398</sup>J. Rupp and R. Birringer, *Phys. Rev. B* **36**(15), 7888 (1987).
- <sup>399</sup>N. X. Sun and K. Lu, *Phys. Rev. B* **54**(9), 6058 (1996).
- <sup>400</sup>Y. Yin and A. Paul Alivisatos, *Nature* **437**(7059), 664 (2005).
- <sup>401</sup>M. B. Zanjani and J. R. Lukes, *J. Appl. Phys.* **115**(14), 143515 (2014).
- <sup>402</sup>A. Dong, X. Ye, J. Chen, Y. Kang, T. Gordon, J. M. Kikkawa, and C. B. Murray, *J. Am. Chem. Soc.* **133**(4), 998 (2011).
- <sup>403</sup>M. T. Frederick, V. A. Amin, L. C. Cass, and E. A. Weiss, *Nano Lett.* **11**(12), 5455 (2011).
- <sup>404</sup>D. V. Talapin, J.-S. Lee, M. V. Kovalenko, and E. V. Shevchenko, *Chem. Rev.* **110**(1), 389 (2010).
- <sup>405</sup>N. Yazdani, M. Jansen, D. Bozyigit, W. M. M. Lin, S. Volk, O. Yarema, M. Yarema, F. Juranyi, S. D. Huber, and V. Wood, *Nat. Commun.* **10**(1), 4236 (2019).
- <sup>406</sup>R. H. Terrill, T. A. Postlethwaite, C.-H. Chen, C.-D. Poon, A. Terzis, A. Chen, J. E. Hutchison, M. R. Clark, and G. Wignall, *J. Am. Chem. Soc.* **117**(50), 12537 (1995).
- <sup>407</sup>M. A. Boles and D. V. Talapin, *J. Am. Chem. Soc.* **136**(16), 5868 (2014).
- <sup>408</sup>M. C. Weidman, K. G. Yager, and W. A. Tisdale, *Chem. Mater.* **27**(2), 474 (2015).
- <sup>409</sup>K. J. Schnitzelbaumer and G. Dukovic, *Nano Lett.* **18**(6), 3667 (2018).
- <sup>410</sup>X. Yan, X. Cui, B. Li, and L.-S. Li, *Nano Lett.* **10**(5), 1869 (2010).
- <sup>411</sup>I. Mihalache, A. Radoi, M. Mihaila, C. Munteanu, A. Marin, M. Danila, M. Kusko, and C. Kusko, *Electrochim. Acta* **153**, 306 (2015).
- <sup>412</sup>G. Zamiri and S. Bagheri, *J. Colloid Interface Sci.* **511**, 318 (2018).
- <sup>413</sup>V. Gupta, N. Chaudhary, R. Srivastava, G. D. Sharma, R. Bhardwaj, and S. Chand, *J. Am. Chem. Soc.* **133**(26), 9960 (2011).
- <sup>414</sup>H. Han, Y. Zhang, N. Wang, M. K. Samani, Y. Ni, Z. Y. Mijbil, M. Edwards, S. Xiong, K. Sääskilahti, M. Murugesan, Y. Fu, L. Ye, H. Sadeghi, S. Bailey, Y. A. Kosevich, C. J. Lambert, J. Liu, and S. Volz, *Nat. Commun.* **7**(1), 11281 (2016).
- <sup>415</sup>A. J. Nozik, *Physica E* **14**(1), 115 (2002).
- <sup>416</sup>M. Potenza, A. Cataldo, G. Bovesecchi, S. Corasaniti, P. Coppa, and S. Bellucci, *AIP Adv.* **7**(7), 075214 (2017).

- <sup>417</sup>A. H. Elsheikh, S. W. Sharshir, M. E. Mostafa, F. A. Essa, and M. K. Ahmed Ali, *Renewable Sustainable Energy Rev.* **82**, 3483 (2018).
- <sup>418</sup>E. K. Goharshadi, Z. Niyazi, M. Shafaei, M. B. Moghaddam, R. Ludwig, and M. Namayandeh-Jorabchi, *J. Mol. Liq.* **241**, 831 (2017).
- <sup>419</sup>E. Ettefaghi, B. Ghobadian, A. Rashidi, G. Najafi, M. Hadi Khoshtaghaza, and S. Pourhashem, *Energy Convers. Manage.* **153**, 215 (2017).
- <sup>420</sup>F. Sedaghat and F. Yousefi, *J. Mol. Liq.* **278**, 299 (2019).
- <sup>421</sup>J. R. Seibert, O. Keles, J. Wang, and F. Erogogbo, *Data Brief* **28**, 105008 (2020).
- <sup>422</sup>K. M. F. Shahil and A. A. Balandin, *Nano Lett.* **12**(2), 861 (2012).
- <sup>423</sup>E. Isotta, U. Syafiq, N. Ataollahi, A. Chiappini, C. Malerba, S. Luong, V. Trifiletti, O. Fenwick, N. M. Pugno, and P. Scardi, *Phys. Chem. Chem. Phys.* **23**(23), 13148 (2021).
- <sup>424</sup>H. Yang, L. A. Jauregui, G. Zhang, Y. P. Chen, and Y. Wu, *Nano Lett.* **12**(2), 540 (2012).
- <sup>425</sup>M.-L. Liu, F.-Q. Huang, L.-D. Chen, and I.-W. Chen, *Appl. Phys. Lett.* **94**(20), 202103 (2009).
- <sup>426</sup>J. M. Skelton, A. J. Jackson, M. Dimitrijevska, S. K. Wallace, and A. Walsh, *APL Mater.* **3**(4), 041102 (2015).
- <sup>427</sup>M. Handwerg, R. Mitdank, S. Levencio, S. Schorr, and S. F. Fischer, *Mater. Res. Express* **7**(10), 105908 (2020).
- <sup>428</sup>E. Isotta, B. Mukherjee, C. Fanciulli, N. Ataollahi, I. Sergueev, S. Stankov, R. Edla, N. M. Pugno, and P. Scardi, *Phys. Rev. Appl.* **14**(6), 064073 (2020).
- <sup>429</sup>W. D. Thompson, A. Nandur, and B. E. White, Jr., *J. Appl. Phys.* **119**(9), 095108 (2016).
- <sup>430</sup>K. Ye, S. C. Siah, P. T. Erslev, A. Akey, C. Settens, M. S. B. Hoque, J. Braun, P. Hopkins, G. Teeter, T. Buonassisi, and R. Jaramillo, *Chem. Mater.* **31**(20), 8402–8412 (2019).
- <sup>431</sup>S. D. Sharma, B. Khasimsaheb, Y. Y. Chen, and S. Neeleshwar, *Ceram. Int.* **45**(2), 2060–2068 (2019).
- <sup>432</sup>K. Kapusta, M. Drygas, J. F. Janik, P. Jelen, M. M. Bucko, and Z. Olejniczak, *J. Alloys Compd.* **770**, 981 (2019).
- <sup>433</sup>Q. Zhang, X. Ai, L. Wang, Y. Chang, W. Luo, W. Jiang, and L. Chen, *Adv. Funct. Mater.* **25**(6), 966 (2015).
- <sup>434</sup>K.-H. Lee, H.-S. Kim, S.-I. Kim, E.-S. Lee, S.-M. Lee, J.-S. Rhyee, J.-Y. Jung, I.-H. Kim, Y. Wang, and K. Koumoto, *J. Elecron. Mater.* **41**(6), 1165 (2012).
- <sup>435</sup>B. Paul, V. Ajay Kumar, and P. Banerji, *J. Appl. Phys.* **108**(6), 064322 (2010).
- <sup>436</sup>M. Koirala, H. Zhao, M. Pokharel, S. Chen, T. Dahal, C. Opeil, G. Chen, and Z. Ren, *Appl. Phys. Lett.* **102**(21), 213111 (2013).
- <sup>437</sup>S. Wang, H. Li, R. Lu, G. Zheng, and X. Tang, *Nanotechnology* **24**(28), 285702 (2013).
- <sup>438</sup>L. Dong, L. Ye, D. Zhao, L. Tong, F. Gao, W. Li, P. Lu, and X. H. Bu, *J. Phys. Chem. Lett.* **11**(14), 5728 (2020).
- <sup>439</sup>Z. Liang, S. Zhang, X. Xu, N. Wang, J. Wang, X. Wang, Z. Bi, G. Xu, N. Yuan, and J. Ding, *RSC Adv.* **5**(74), 60562 (2015).
- <sup>440</sup>N. Cho, F. Li, B. Turedi, L. Sinatra, S. P. Sarmah, M. R. Parida, M. I. Saidaminov, B. Murali, V. M. Burlakov, A. Goriley, O. F. Mohammed, T. Wu, and O. M. Bakr, *Nat. Commun.* **7**(1), 13407 (2016).
- <sup>441</sup>L. Yan, J. Ma, P. Li, S. Zang, L. Han, Y. Zhang, and Y. Song, *Adv. Mater.* **34**(7), 2106822 (2022).
- <sup>442</sup>Z. Dai, S. K. Yadavalli, M. Chen, A. Abbaspouramijani, Y. Qi, and N. P. Padture, *Science* **372**(6542), 618 (2021).
- <sup>443</sup>Z. Dai and N. P. Padture, *Nat. Energy* **8**(12), 1319 (2023).
- <sup>444</sup>I. S. Yang, Z. Dai, A. Ranka, D. Chen, K. Zhu, J. J. Berry, P. Guo, and N. P. Padture, *Adv. Mater.* **36**(3), 2308819 (2024).
- <sup>445</sup>F. Hofmann, D. R. Mason, J. K. Eliason, A. A. Maznev, K. A. Nelson, and S. L. Dudarev, *Sci. Rep.* **5**(1), 16042 (2015).
- <sup>446</sup>M. Kim, K. Park, G. Kim, J. Yoo, D.-K. Kim, and H. Kim, *Appl. Sci.* **9**(8), 1522 (2019).
- <sup>447</sup>D. Sarker, R. W. Hooper, A. Karmakar, A. Bhattacharya, A. Pominov, V. V. Terskikh, and V. K. Michaelis, *ACS Mater. Lett.* **4**, 1255–1263 (2022).
- <sup>448</sup>X. Mettan, R. Pisoni, P. Matus, A. Pisoni, J. Jaćimović, B. Náfrádi, M. Spina, D. Pavuna, L. Forró, and E. Horváth, *J. Phys. Chem. C* **119**(21), 11506 (2015).